Metal-Based Soft Materials in Biological Applications

M.Sc. Research Thesis

By

Ashish Bora

DEPARTMENT OF CHEMISTRY

INDIAN INSTITUTE OF TECHNOLOGY INDORE

MAY, 2024

Metal-Based Soft Materials in Biological Applications

A THESIS

Submitted in partial fulfillment of the

requirements for the award of the degree

of

Master of Science

by

ASHISH BORA

DEPARTMENT OF CHEMISTRY

INDIAN INSTITUTE OF TECHNOLOGY INDORE

MAY, 2024

INDIAN INSTITUTE OF TECHNOLOGY INDORE

CANDIDATE'S DECLARATION

I hereby certify that the work being presented in the thesis entitled **"Metal-Based Soft Materials in Biological Applications"** in the partial fulfillment of the requirements for the award of the degree of **MASTER OF SCIENCE** and submitted to the **Department of Chemistry, Indian Institute of Technology Indore**, is an authentic record of my work carried out during the period from July 2023 to May 2024 under the supervision of Dr. Suman Mukhopadhyay, Professor, IIT Indore.

The matter presented in this thesis has not been submitted by me for the award of any other degree of this or any other institute.

Ashish Bora

This is to certify that the above statement made by the candidate is correct to the best of my/our knowledge.

Prof. Suman Mukhopadhyay

Ashish Bora has successfully given his M.Sc. Oral Examination held on **09/05/2024**.

Signature of Supervisor of M.Sc. thesis
Prof. Suman Mukhopadhyay
Date: 20/05/2024

Convener DPGC
Dr. Umesh A Kshirsagar
Date:

Signature of PSPC Member 1
Prof. Sampak Samanta
Date:

Signature of PSPC Member 2
Dr. Amrendra Kumar Singh
Date:

ACKNOWLEDGEMENTS

From the bottom of my heart, I am grateful to God for giving me blessings, perseverance, and courage. I want to express my appreciation to everyone who contributed to this project and helped me finish my project successfully.

First and foremost, I want to express my sincere thanks and profound gratitude to my supervisor, Prof. Suman Mukhopadhyay, for his constant support, continuous guidance, belief, and encouragement throughout my work. I am fortunate enough to have the opportunity to work under his kind supervision and learn from him.

I would also like to thank my PSPC members, Prof. Sampak Samanta and Dr. Amrendra Kumar Singh, for their valuable suggestions and guidance. I thank Dr. Tushar Kanti Mukherjee, Head of Department, Chemistry, and DPGC Convenor, Dr. Umesh A. Kshirsagar, for their sincere recommendations and assistance.

I express my esteemed gratitude to Prof. Suhas S. Joshi, Director, IIT Indore, for providing the resources and a favorable research environment.

I am grateful to the Sophisticated Instrument Centre (SIC), IIT Indore for instrumentation facilities, and the Chemistry Office for their assistance and technical support, without which I would not have been able to work on this project.

I thank my mentors, Ms. Ritika Munjal and Mr. Argha Chakraborty, for guiding and assisting me in every step which helped me make progress in this project. I am also thankful to my other lab members for their constant encouragement.

I am thrilled to express my special thanks to Dr. Reena Kyarikwal for her unwavering support and suggestions throughout this research project.

I also acknowledge with deep reverence my parents, family members, and friends, who have always supported me morally and encouraged me.

Through the kindness of these acknowledged persons, I have made successful progress in this project. Without their guidance, I would not have made any headway in this research project.

ASHISH BORA

Department of Chemistry, IIT Indore

DEDICATED TO…

My beloved parents and sisters for their constant support in every way possible

ABSTRACT

The project includes synthesizing and optimizing metal-based soft materials (metallogels) with various applicable properties. The gelator component TABTA has been synthesized because it possesses hydrogen bond donor-acceptor sites that actively participate in forming non-covalent interactions. Specifically, two hybrid organogel matrices **G8-TABTA** (N^2, N^4, N^6-tri(1H-tetrazol-5-yl)-1,3,5-triazine-2,4,6-triamine and benzene-1,3,5-tricarboxylic acid tris-[(4-aminophenyl)-amide]) and **TABTA-Ibp** (Benzene-1,3,5-tricarboxylic acid tris-[(4-aminophenyl)-amide] and sodium salt of Ibuprofen) have been designed and optimized effectively. These matrices form silver metallogels, and the formation of silver nanoparticles serves as a scaffold for gel fabrication. Various spectroscopic techniques have been employed to characterize these metallogels successfully. All gel matrices display typical gel characteristics such as flexibility, stability, and self-healing properties. To understand the interactions between gelator components, FT-IR and PXRD analyses of their xerogels have been conducted. Additionally, rheologic properties are explored to assess the strength and thixotropic properties of the gels. Previously, based on an earlier report, a gelator molecule **GE** (Benzene- tricarbonyl tris(azanediyl)) tris(4-aminobenzoic acid)) has been synthesized to form a hybrid gel with **G8**. This **G8GE** gel exhibited the aggregation-induced enhanced emission (AIEE) phenomenon in its aggregated state. Therefore, in this study, leveraging the fluorescence characteristics of the gelator component **TABTA**, a gel matrix, **G8-TABTA** has been designed, which demonstrates the aggregation-caused quenching (ACQ) phenomenon in its aggregated state. Additionally, another gel matrix, **TABTA-Ibp**, loaded with silver nanoparticles, featuring injectability, has been designed for dual delivery of Ibuprofen drug and AgNPs, serving simultaneously as anti-inflammatory and antimicrobial agents.

TABLE OF CONTENTS

LIST OF FIGURES

LIST OF TABLES

LIST OF SCHEMES

NOMENCLATURE

θ	Angle
Å	Angstrom
cm	Centimetre
δ	Chemical Shift (NMR)
°C	Degree Centigrade
g	Gram
mg	Milli gram
µL	Micro Litre
mL	Milli Litre
mmol	Milli Mole
mol	Mole
%	Percentage
h	Hours

ACRONYMS

ACN	Acetonitrile
ACQ	Aggregation-caused quenching
AIEE	Aggregation-induced emission enhancement
AgNPs	Silver nanoparticles
BET	Brunauer-Emmett-Teller
BJH	Barrett-Joyner-Halenda
CCl_4	Carbon tetrachloride
CGC	Critical Gel Concentration
DCM	Dichloromethane
DMF	N, N-Dimethylformamide
DMSO	Dimethylsulphoxide
EDS	Energy-dispersive X-ray spectroscopy
ESI-MS	Electron Spray Ionization-Mass Spectrometry
EtOH	Ethanol
FESEM	Field-Emission Scanning Electron Microscopy
FT-IR	Fourier Transform- Infrared
HCl	Hydrochloric acid
H_2O	Water
LMWGs	Low molecular weight gelators
NMR	Nuclear Magnetic Resonance
NSAID	Non-steroidal anti-inflammatory drug
N_2	Nitrogen
PBS	Phosphate buffered saline
Ppm	Parts per million
PXRD	Powder X-ray Diffraction
TICT	Twisted intramolecular charge transfer
TGA	Thermogravimetric Analysis
UV-Vis	Ultraviolet-Visible

CHAPTER 1

INTRODUCTION

1.1 General Introduction

Gels are a fascinating class of materials characterized by their intermediate state between solids and liquids.[1] In general, a gel is a soft material self-assembled through non-covalent interactions and can occupy a considerable amount of solvent within its matrix while maintaining its stability. This unique property allows them to exhibit various characteristics, ranging from soft and flexible to rigid and resilient. Non-covalent interactions facilitate the self-assembly of molecules capable of gel formation, with solvent molecules forming supramolecular gels. Various solvent mixtures can be trapped within the bonding sites of a gelator molecule depending on their properties resulting in the formation of a gel.[2] Gels possess a porous structure, which allows them to absorb and retain large amounts of solvent or other substances. Gel formation is a unique property, even though it is very challenging to predict the structure accurately. Molecules containing specific functional groups and appropriate sites for extensive non-covalent interactions are more likely to exhibit gelation. Generated by extensive non-covalent interactions, gels can undergo sol-gel transition. Gels typically do not possess self-regulating behavior. However, their properties can be modulated due to external stimuli like heat, light, sound, sonication, changes in pH, mechanical force, and the presence of other chemical entities including cations, anions, neutral chemicals, and chiral guest molecules.[3] These stimuli induce microscopic changes in the gel's structure, can affect its aggregation and morphology, and trigger transitions between different gel states (**Figure 1.1**). Many gels exhibit shear-thinning behavior, meaning they flow more easily under shear stress but recover their gel structure when the stress is removed. Some gels are sensitive to changes in pH, swelling, or contracting in response to variations in acidity or alkalinity while, some gels are biocompatible,[4] meaning they are non-toxic and do

not elicit an immune response when introduced into living organisms. Additionally, certain gels, termed conductive gels,[5] can conduct electricity. Thus, depending upon the properties of the formed gel, it can be applied to a wide range of applications in various fields, including tissue engineering,[6] sensing,[7] energy conversion and storage systems,[8] 3D bioprinting,[9] drug delivery and controlled release systems,[10] environmental science,[11], etc.

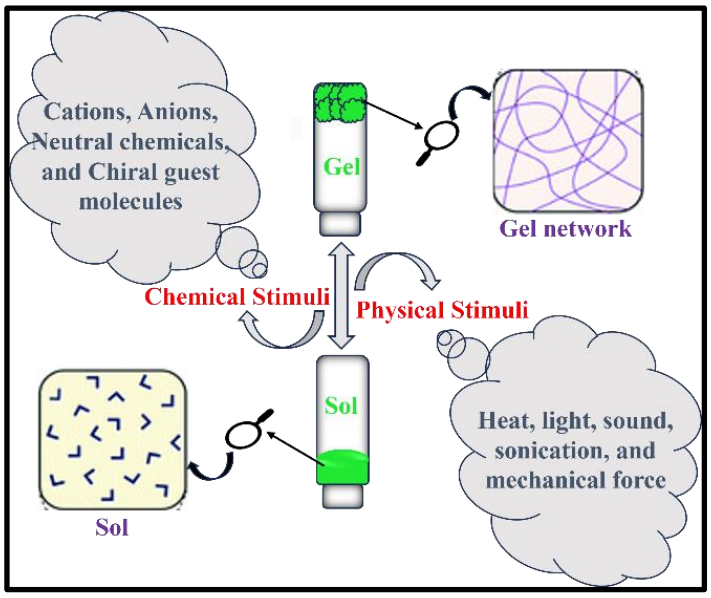

Figure 1.1: Physical and chemical stimuli responsible for sol-gel transitions

1.2 Classification of gels

Gels can be classified in various ways based on their composition, structure, and properties, with their solvent playing a crucial role. Gels can be categorized as hydrogels when water comprises the liquid phase or as organogels when organic solvents are utilized. If the gel is incorporated with metal ions or complex, it is termed a metallogel. Further, a metallogel is divided into two sub-categories: (i) metal complex induced gel in which the gel formation typically occurs when metal complexes interact with other components in a solution, leading to the formation of a three-dimensional network structure that immobilizes the solvent molecules,[12] (ii) coordination polymer gel in which metal ions are coordinated with organic ligands to form extended networks in a self-

assembled fashion (**Figure 1.2**).[13] These networks can entangle solvent molecules, resulting in the formation of a gel-like material. The gelation process is often driven by the coordination bonds between the metal ions and the ligands, as well as other non-covalent interactions such as hydrogen bonding or π-π stacking.

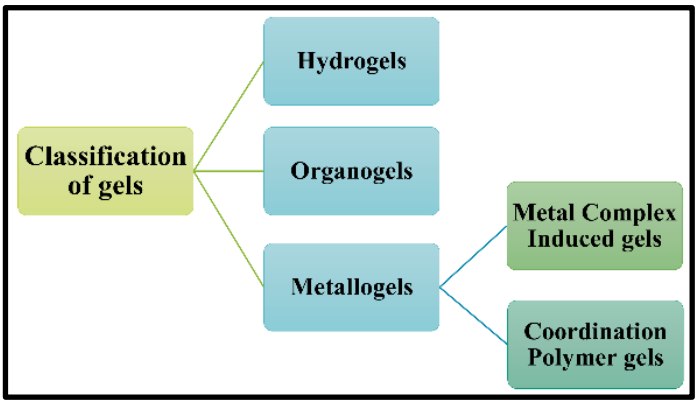

Figure 1.2: Classification of gels

1.3 Gels: Synthesis and fabrication

The synthesis and fabrication of gels enclose various methodologies tailored to produce materials with specific structures and properties suitable for various applications. Chemical crosslinking methods involve the formation of covalent bonds between polymer chains, creating a three-dimensional network that imparts mechanical strength and stability to the gel. Physical gelation techniques exploit non-covalent interactions, such as hydrogen bonding or hydrophobic interactions, to induce gel formation without altering the chemical structure of the gel components. Sol-gel transitions, driven by changes in temperature, pH, or solvent composition, facilitate the conversion of colloidal dispersions into solid gel networks through aggregation and self-assembly processes.[14] Template-assisted methods utilize templates or scaffolds to guide the assembly of gel components into desired structures. At the same time, self-assembly techniques rely on the spontaneous organization of molecular or colloidal building blocks to form ordered gel networks. Each method offers distinct advantages, allowing precise control over gel properties and structures to meet specific application requirements.

1.4 Metallogels: Properties and Characterization

Metallogels are a class of gels where metal ions or metal-containing complexes play a crucial role in the gelation process. These gels typically consist of metal-containing building blocks, such as metal ions, coordination complexes, or metal nanoparticles, which interact with each other or other components to form a three-dimensional network structure. Metallogels can exhibit unique properties and functionalities attributed to the presence of metal species within the gel matrix. The choice of metal ions and ligands, as well as their concentration and stoichiometry, can significantly influence the properties of the resulting metallogel, including its mechanical strength, responsiveness to external stimuli, and potential applications.[15]

The gel fabrication can be examined by varying concentrations of the low molecular weight gelator (LMWG) and the minimum concentration of gelator molecules required to form a stable gel under specific conditions, termed the critical gel concentration (CGC).[16] Below the CGC, the gelator molecules are dispersed homogeneously in the solvent without forming interconnected networks. As the concentration of gelator molecules increases beyond the CGC, they begin to interact and self-assemble, eventually leading to the formation of a gel network. The CGC is an important parameter in the study of gelation processes as it provides insight into the concentration-dependent behavior of gel systems and helps in the design and optimization of gel-forming materials.

The characterization of gels involves various techniques to understand their structure, properties, and behavior. A gel's mechanical strength and sol-gel transition behavior are significant characteristics that can be analyzed using rheology. The rheology of gels involves the study of their flow and deformation behavior under applied forces. Gels exhibit viscoelastic behavior, meaning their response to applied stress involves both viscous (flow-like) and elastic (solid-like) deformation.[17] This behavior arises from the structural network within the gel, which allows it to deform and flow under stress while also maintaining its overall structure. Rheological measurements involve frequency sweep and strain

sweep experiments, where the gel is subjected to oscillatory strain over a range of frequencies or amplitudes. The material's response is assessed in terms of the storage modulus (G'), representing the elastic response of the gel, and the loss modulus (G''), representing the viscous response. These experiments provide information about the gel's viscoelastic properties and its response to different deformation conditions. The crossover point (G'=G'') can also be determined utilizing rheology that quantifies the balance between storage and loss modulus. This point is also called the gel point, which represents the transition from liquid-like to solid-like behavior during the gelation process.[18] Certain gels also exhibit thixotropic behavior, meaning their viscosity decreases over time under constant strain, followed by a recovery of viscosity when the strain is removed. This characteristic is evaluated through a rheological analysis involving time-oscillation strain-sweep experiments.[19]

The FT-IR (Fourier transform Infrared) spectroscopic technique is utilized to identify the functional groups in the gelator and the interactions occurring within these functional groups. These interactions are pivotal for creating a 3D gel network, resulting in gel formation and they are evident from the changes in the intensity and shifts in the IR bands. In the context of hybrid gel matrices, the changes in the shift of the IR bands can be utilized to determine the interactions responsible for the gel formation between two gelator components as well.[20] The PXRD (Powder X-ray Diffraction) technique is also well utilized to determine the orientation and crystallinity of the gelator components.[21] The interplanar distance helps to govern the non-covalent interactions responsible for the self-assembly between the gelator components, resulting in gel formation.

The NMR (Nuclear Magnetic Resonance) technique is indeed a valuable technique for characterizing gels. The study of molecular interactions within gels, including gelator-solvent interactions, gelator-gelator interactions, and host-guest interactions, can be analyzed by chemical shift changes, peak broadening, and cross-peak patterns in NMR spectra, and the nature and strength of interactions between the gelator components can be elucidated.[22]

The Field-Emission Scanning Electron Microscopy (FESEM) analysis investigates gels' morphology, enabling the examination of morphological transitions from the gelator to the gel network.[23] The energy-dispersive X-ray spectroscopy (EDS) enables elemental analysis of gel samples, providing information about the chemical composition and elemental distribution within the gel matrix. This allows us to identify the presence of specific elements or chemical species and to correlate elemental distribution with structural features observed in FESEM images.

The TGA (Thermogravimetric Analysis) determines gels' thermal decomposition behavior and stability under controlled heating conditions. The BET (Brunauer-Emmett-Teller) technique is utilized to provide valuable information about the porosity, surface area, and pore size distribution of the gel matrix.[24]

1.5 AIEE and ACQ phenomenon

The molecules self-assembled within the gel, depending on the specific molecular structure, the arrangement of the gel matrix, and the intermolecular interactions with the gel network certain gel compositions favor AIEE (aggregation-induced emission enhancement),[25] leading to enhanced emission or ACQ (aggregation-caused quenching),[26] leading to decreased emission efficiency.

AIEE molecules typically have rigid or sterically hindered structures that restrict intramolecular motion. In solution, these molecules exhibit weak fluorescence due to the availability of non-radiative relaxation pathways facilitated by free rotation or intramolecular motion However, intramolecular motion is restricted when molecules aggregate or become confined in a rigid environment such as a gel matrix, leading to reduced non-radiative decay and enhanced radiative emission. Some AIEE molecules exhibit a twisted intramolecular charge transfer (TICT) mechanism. In solution, the TICT state typically leads to non-radiative decay pathways, resulting in weak fluorescence. However, in aggregated or rigid environments like gels, the TICT state may be stabilized, leading to enhanced fluorescence.[27] AIEE molecules may have specific chemical

functionalities or substituents that suppress intermolecular interactions in the aggregated state.

In contrast, ACQ molecules experience enhanced intermolecular interactions such as π-π stacking, van der Waals forces, and dipole-dipole interactions in the aggregated states. These interactions promote non-radiative pathways for energy transfer or quenching, competing with radiative decay pathways and leading to reduced fluorescence intensity.[28]

1.6 Drug Delivery

Gels offer significant advantages as formulations for drug delivery as well, including their simple preparation and administration. Sustained drug release can be optimized by adjusting the structure of low molecular weight gelators (LMWGs) and potentially modifying the organic phase. Precise control over drug dosage, location, and timing is crucial in drug delivery to maximize therapeutic benefits while minimizing side effects. Organogels are moisture-resistant and enhance skin penetration.[29,30] Their organic nature also helps prevent microbial contamination, making their gelation and entrapment procedures easy to manage.

Gels offer numerous advantages as drug delivery systems, making them an attractive choice for various therapeutic applications: (i) Gels can provide sustained release of drugs over an extended period, maintaining therapeutic concentrations in the target tissue or site of action. This sustained release profile can improve drug efficacy and reduce the frequency of dosing, enhancing patient compliance. (ii) Gels can encapsulate a wide range of drugs, including hydrophilic, hydrophobic, and amphiphilic compounds. This versatility allows for the delivery of diverse classes of therapeutics, including small molecules, proteins, peptides, and nucleic acids. (iii) Gels can be engineered to provide targeted delivery of drugs to specific tissues or organs within the body. This can minimize systemic side effects and improve therapeutic outcomes by concentrating the drug at the site of action. (iv) Gels are often easy to administer and can be formulated into various dosage forms, including creams, gels, ointments, films, and implants. This flexibility in

formulation allows for convenient and patient-friendly drug delivery options. (v) Gels can respond to external stimuli or physiological cues, enabling the controlled release of drugs in a spatiotemporal manner. Stimuli-responsive gels can be designed to release drugs in response to factors such as pH, temperature, light, or enzyme activity, offering precise control over drug delivery.

Further, gels can enable the simultaneous delivery of multiple drugs, allowing for combination therapy to address complex medical conditions or multiple symptoms. Dual drug delivery via gels can leverage synergistic effects between the drugs, where the combination produces a greater therapeutic effect than either drug alone. This approach can enhance treatment efficacy by targeting multiple pathways or disease mechanisms simultaneously.[31] In addition to drugs, gels can also incorporate other therapeutic agents such as nanoparticles, growth factors, or biomolecules.[32] This allows for the delivery of multiple types of therapeutic agents, further enhancing treatment options and efficacy.

1.7 Organization of the Thesis

Chapter 1: This chapter briefly describes the general introduction and classification of gels, synthesis, and fabrication of gels, characterization techniques and fluorescence behavior of gels, and utilization of gels in drug delivery systems.

Chapter 2: This chapter discusses the past work on this topic and the motivation behind this work.

Chapter 3: This chapter includes the experimental procedure for the synthesis of gelator components, fabrication of gels, instrumentation techniques for analysis of gels, and the release study of the drug from the gel matrix.

Chapter 4: This chapter discusses all the project's results and outcomes.

Chapter 5: This chapter concludes and summarizes the work done and discusses the future scope of the project.

CHAPTER 2

LITERATURE SURVEY

2.1 Review of Pastwork and Project Motivation

Various works on the fabrication of supramolecular gels formed by the self-assembly of low molecular weight gelator molecules have been reported possessing various non-covalent interactions that precisely adjust the supramolecular structures, unlocking the full potential of these soft materials for a wide range of applications. These non-covalent interactions include hydrogen bonding, π-π stacking, Van der Waals interactions, hydrophobic interactions, metal coordination, dipole-dipole interactions, etc.,[33] and form a 3-D network of entrapped solvent molecules, including gel formation.

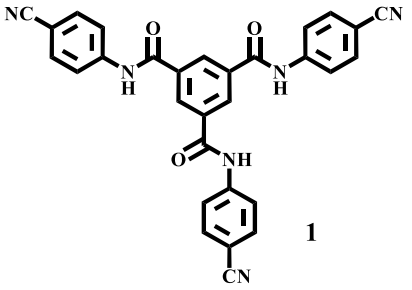

1

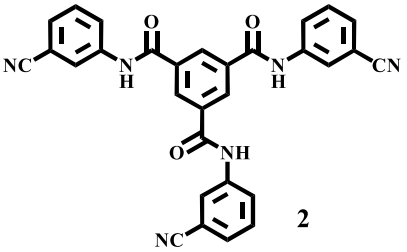

2

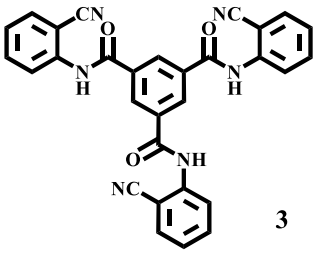

3

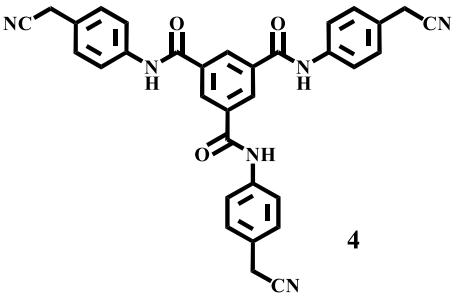

4

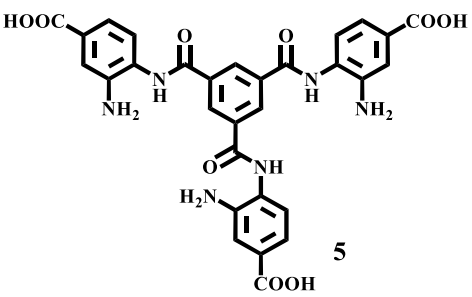

5

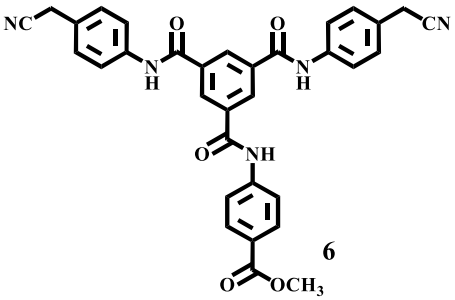

6

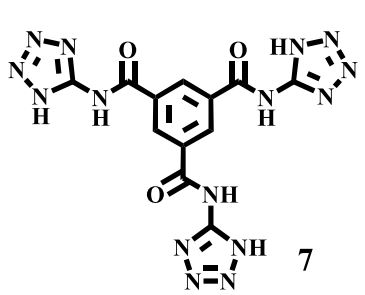

7

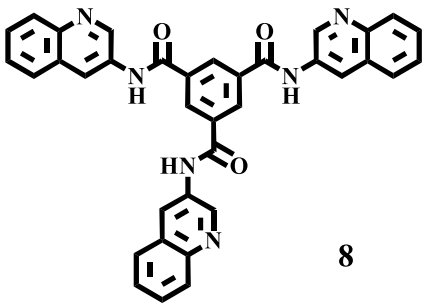

8

Figure 2.1: Structures of gelator molecules leading to gelation[34–38]

The molecules shown in **Figure 2.1** are examples of some previously reported gelator molecules leading to gelation due to non-covalent interactions. Therefore, from the above-mentioned gelator molecules, it is evident that C_3 symmetric molecules containing carboxamide groups exhibit gelation properties. The main advantage of such a moiety is that it easily allows the incorporation of metals in the assembly forming a stable metallogel. Further, incorporating a metal ion into an organogel unlocks the possibility of utilizing them as catalysts, sensors, optical, redox, and magnetic materials, etc.[39] Furthermore, the presence of metal components allows fine-tuning of gelation capabilities and modification of gel morphologies. Several reports revealed that metals like ruthenium and iron are easily incorporated within this tri-carboxamide moiety, forming a stable metallogel that can be further applied to various applications, including drug delivery,[10] anticancer agents,[34] stabilization of nanoparticles,[35] and catalysis.[36]

Due to the various interactions in the gel matrix, these materials could be an alternative to the conventionally used materials. In the latest report by Kyarikwal et al., a 1,3,5-tri-carboxamide molecule was utilized to enhance the strength and stability of an already gel-forming tetrazole moiety. The hybrid matrix **G8GE** exhibited the aggregation-induced enhanced emission (AIEE) phenomenon due to restriction in intramolecular motion between the two components. This led to reduced non-radiative decay and enhanced radiative emission in its aggregated state. The matrix showed the capacity to remove heavy metal ions from their aqueous solution.[37]

Hence, this can be an excellent opportunity to modify the structure of 1,3,5-tri carboxamide into its derivatives that can either be susceptible to gelation

or able to form a hybrid gel matrix with **G8** showing different behavior as of **G8GE** matrix and can be suitable for biological applications.

At the same time, it would be interesting if the synthesized 1,3,5-tri carboxamide gelator component could serve as a drug carrier in response to external stimuli like pH, sonication, or UV-vis irradiation as gels are suitable candidates for sustained and targeted drug delivery Generally, gels with moderate strength and thixotropic behavior are preferred. Uzan et al. developed novel dermal and topical drug delivery vehicles using amino alcohol-based bis-(amino alcohol)oxalamides (BAOAs) as the key compounds. These BAOAs were utilized to form organogels for delivering Ibuprofen, a non-steroidal anti-inflammatory drug (NSAID), by loading it into the organogel matrix, and the release kinetics of Ibuprofen were investigated using UV-Vis spectroscopy.[40]

Praveen et al. introduced a novel gel-forming supramolecular synthon, termed primary ammonium monocarboxylate (PAM), which has been utilized to create a range of PAM salts by reacting Ibuprofen with different primary amines. These PAM salts were effective in gelling methyl salicylate (MS) and proved suitable for delivering the gelator drug in a self-delivery manner for treating skin inflammation.[41]

Further, Yadav et al. designed a new gel formulation containing low molecular mass DAP (2,6-diamino pyridine) derived fatty acid amides with varying alkyl chain lengths and was utilized as a carrier for ibuprofen drug delivery.[42]

Constantin et al. recently developed an environmentally friendly composite film using poly(vinyl alcohol) (PVA) cross-linked with oxidized chitosan (OxCS), with the addition of silver nanoparticles (AgNPs) during the film synthesis process. This involved incorporating freshly prepared chitosan-capped AgNP colloidal solution into the polymer mixture. Subsequently, Ibuprofen (Ibp) was loaded in the most effective film formulation. The resulting Ibp-loaded PVA/OxCS-Ag films demonstrated promising capabilities for ibuprofen delivery while

exhibiting effective antimicrobial properties against common pathogens found in oral cavities.[43]

Popescu et al. introduced a composite hydrogel composed of chitosan (CS) and poly(vinyl alcohol) (PVA), with the incorporation of silver nanoparticles (AgNPs) possessing antibacterial properties and Ibuprofen (Ib) as an anti-inflammatory agent. This hydrogel exhibited favorable mechanical characteristics, with a compressive modulus of 132 kPa, along with high swelling capacity and sustained drug release under simulated skin conditions. Additionally, the hydrogel demonstrated potent antibacterial activity against *S. aureus* and *K. pneumoniae*, due to embedded AgNPs.[44]

From the above literature survey and previous reports, it is evident that functional groups having active hydrogen donor-acceptor sites and amide groups are potent for gel formation. Thus, a C_3 symmetric gelator component having an amide and free amine group has been used to form two hybrid organogel matrices and their metallogels. The design of this gelator component is tailored to exhibit distinct behavior compared to the **G8GE** matrix, and it also serves as a carrier for the dual delivery of Ibuprofen drug and silver nanoparticles, enabling it to function simultaneously as a pain reliever and an antibacterial agent.

CHAPTER 3

EXPERIMENTAL SECTION

3.1 Reagents and Chemicals

The chemicals and solvents used in this work were purchased from Alfa Aesar, Avra Chemicals, HiMedia Chemicals, Sigma-Aldrich, and Finar, India, and used directly without additional purification. The metal perchlorate salts were synthesized in the laboratory using the reported procedure.[45]

3.2 Methods and Instrumentation

A Bruker Tensor 27 FTIR spectrophotometer measured the FTIR (Fourier-transform infrared) spectra within the 4000-500 cm-1 range. Electrospray ionization mass spectrometry (ESI-MS) data was obtained using a Bruker-Daltonics micro TOF-Q II instrument. NMR spectra were obtained with an AVANCE NEO500 Ascend Bruker BioSpin International AG instrument with TMS as the standard reference at room temperature using DMSO-d_6. The mechanical properties and thixotropic behavior of gels were investigated using a rheometer. An Anton Paar Physica MCR 301 rheometer was utilized for rheological analysis at 25ºC using a 25 mm parallel plate with a true gap of 0.5 mm. Morphological investigations of the gelator components, organogels, metallogels, and silver nanoparticles were performed using A Supra55 Zeiss field emission scanning electron microscope (FE-SEM). The powder X-ray diffraction (PXRD) pattern for gelator components and all the xerogels were recorded on an Empyrean, Malvern Panalytical, with Cu-Kα radiation. TGA experiments were done using a Mettler Toledo Thermal Analyser under a nitrogen atmosphere in the 30-800 ºC temperature range at a rate of 10 ºC min^{-1}. Porosity parameters were determined using a Quantachrome Autosorb iQ2 Brunauer–Emmett–Teller (BET) surface area analyzer. A Fluoromax-4 spectrofluorometer (HORIBA Jobin Yvon, model FM-100) was used to study the emission spectra of the gelatin components. The absorption spectra, formation of silver nanoparticles,

and drug release studies were monitored by UV-visible spectroscopy using a Varian carry 100 Bio UV−vis spectrophotometer in a quartz cuvette (1cm × 1cm).

3.3 Synthesis of gelator components G8 and TABTA

3.3.1 Synthesis of Benzene-1,3,5-tricarboxylic acid tris-[(4-nitrophenyl)-amide] (TNBTA)

The synthesis of **TNBTA** was done using the reported procedure.[46] In a round bottom flask, 0.80 g (5.79 mmol) of 4-nitroaniline was suspended in 50 mL acetonitrile, and 0.465 g (1.75 mmol) of trimesoyl chloride was added. The reaction mixture was then stirred under reflux (85℃) for 24 hours. The resulting material was filtered and washed multiple times with cold acetonitrile. The product was isolated as a grey solid (0.908 g, 90% yield).

3.3.2 Synthesis of Benzene-1,3,5-tricarboxylic acid tris-[(4-aminophenyl)-amide] (TABTA)

The synthesis of **TABTA** was done using the reported procedure.[47] In a round bottom flask, 1.14 g (2.0 mmol) of **TNBTA** was suspended in 23 mL each of DMF and ethanol, and 10% Pd/C (0.050 g) was added. Subsequently, hydrazine monohydrate 2.6 mL (52.9 mmol) was added dropwise and the resulting mixture was stirred under reflux (100 °C) for 24 hours under an N_2-atmosphere (inert). After the completion of the reaction, the hot mixture was filtered through celite, and washed with hot ethanol. The solvent was then removed under reduced pressure to yield a brown oil. EtOH and a large amount of Milli Q-water were added, and a precipitate was observed within a time. The precipitate was isolated by centrifugation and the product was isolated as a yellow solid (0.650 g, 67.7% yield).

3.3.3 Synthesis of N^2, N^4, N^6-tri(1H-tetrazol-5-yl)-1,3,5-triazine-2,4,6-triamine (G8)

The synthesis of gelator **G8** was done using the reported procedure.[48] In a round bottom flask, 2.47 g (24 mmol) of 5-amino tetrazole monohydrate, and 3.34 mL (24 mmol) of triethylamine were suspended in 80 mL of

ethanol under ice-cooled conditions. Consequently, 1.472 g (8 mmol) of cyanuric chloride was added to it in small portions and the resulting mixture was stirred under reflux (80 °C) for 3 hours. After the completion of the reaction, the precipitate was filtered and washed with 3N HCl, water, and methanol before being dried at room temperature under a vacuum. The desired gelator molecule **G8** was obtained as a white solid (78% yield).

3.4 Gels preparation

3.4.1 Preparation of G8-TABTA organogel and its metallogels

For the formation of **G8-TABTA organogel**, 0.05 mmol (16 mg) of **G8** and 0.05 mmol (24 mg) of **TABTA** were solubilized in 750 µL of DMF by heating for 4-5 minutes that upon homogeneous addition of 250 µL Milli-Q water, forms a yellowish-brown colored organogel instantly (**Figure 3.1**). Subsequently, for the formation of **G8-TABTA metallogels**, 0.05 mmol (16 mg) of **G8** and 0.05 mmol (24 mg) of **TABTA** were solubilized in 750 µL DMF by heating for 4-5 minutes, to which 0.05 mmol of **perchlorate salts** of Ag^{+}, Fe^{3+}, Fe^{2+}, Co^{2+}, Ni^{2+}, Cu^{2+}, and Zn^{2+} dissolved in 250 µL Milli-Q water was homogeneously added forming stable metallogels except for Ni^{2+} perchlorate salt. The gel formation was confirmed by the conventional test tube inversion method.

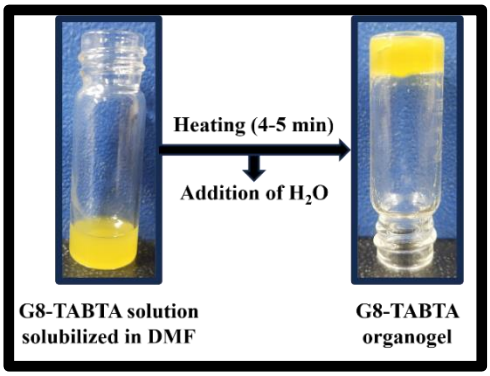

Figure 3.1: **G8-TABTA** organogel formation

3.4.2 Preparation of TABTA- Ibp organogel and its metallogel

For the formation of **TABTA- Ibp organogel**, 0.05 mmol (24 mg) of **TABTA** and 0.15 mmol (34 mg) of the **sodium salt of ibuprofen** were solubilized in 950 µL DMSO by heating followed by the addition of 50 µL

Milli-Q water that on sonication for 4-5 minutes forms a bright yellow colored organogel (**Figure 3.2**). Subsequently, for the formation of **TABTA- Ibp metallogel**, 0.05 mmol (24 mg) of **TABTA,** 0.15 mmol (34 mg) of the **sodium salt of ibuprofen,** and 0.15 mmol of **perchlorate salts** of Ag^{+}, Fe^{3+}, Fe^{2+}, Co^{2+}, Ni^{2+}, Cu^{2+}, and Zn^{2+} were dissolved in 1500 µL DMSO by heating and 250 µL Milli-Q water was uniformly added to the solution that on sonication for 4-5 minutes forms a stable metallogel specifically with Ag^{+} perchlorate salt. The gel formation was confirmed by the conventional test tube inversion method.

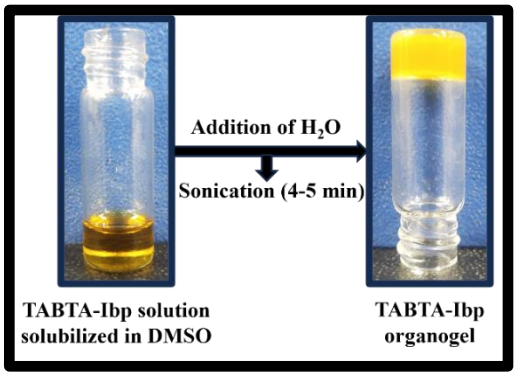

Figure 3.2: **TABTA-Ibp** organogel formation

3.5 Melting temperature of gels (T_{gel})

A silicon oil bath setup determined the gel melting temperature (Tgel) and the sol-gel transition behavior. A 5 mL glass vial was utilized for the experiment, with temperature monitoring facilitated by a thermometer. The gels were placed in the glass vial, along with a steel ball positioned on the gel's surface. Subsequently, the system was immersed in the oil bath. As the temperature increased, the gel began melting (indicated by the steel ball moving downward). The temperature was recorded as the T_{gel}, and heating ceased. After 5-10 minutes, it was observed that the sol reverted to the gel state. The gel melting temperature serves as an indicator of the sol-gel transition temperature for the gels.

3.6 Rheological analysis of gels

The rheological analysis assessed the gels' strength and sol-gel transition characteristics. The storage (G') and loss (G") moduli were measured at a 0.5% strain to assess viscoelasticity and a strain-sweep experiment was

conducted over time to investigate thixotropic behavior, employing 0.5% minimum and 100% maximum strain. With the help of a spatula, the gel was directly taken on the stage of the rheometer for measurements.

3.7 Morphological analysis of gels

Field-emission scanning electron microscopy was utilized to examine the morphology of the gelator components, organogels, and metallogels. Additionally, it was employed to investigate the changes in the self-assembly process and size after the formation of the silver nanoparticles within the gel matrix. To prepare the samples, a small quantity of the gel was spread onto a glass slide, dried, and then coated with gold.

3.8 Drug Release Study

The release of the drug was monitored using UV-visible spectroscopy at two different pH values. An acidic pH of 5.29 simulated the tumor cell environment, while a neutral pH of 7.4 mimicked the normal cell environment. At room temperature, the release of Ibuprofen drug from **TABTA-Ibp** organogel and **TABTA-Ibp-Ag** metallogel matrices was studied by layering them with PBS buffer solution. At different pH values, the gel matrices were layered with 3 mL of PBS buffer and were allowed to stand for 72 hours. Within different time intervals, the UV-Vis spectrum was recorded for the supernatant solution taken out and the amount of drug released was determined using the following equation:

$$D_t = \frac{C_0 - C_t}{C_0} \times 100\% = \frac{A_0 - A_t}{A_0} \times 100\%$$

where D_t is the exchange capacity, C_0 and A_0 are the initial concentration and absorbance of the ibuprofen drug, respectively, and C_t and A_t is the concentration and absorbance of the ibuprofen drug at specific time intervals.

CHAPTER 4

RESULTS AND DISCUSSION

4.1 Synthesis and Characterization

TNBTA and the gelator components **TABTA** and **G8** were successfully synthesized and characterized. **TNBTA** was synthesized by amide bond formation between trimesoyl chloride and 4-nitroaniline in the presence of acetonitrile (**Scheme 4.1**) followed by its reduction to form **TABTA** (**Scheme 4.2)** as a yellow-colored solid product and **G8** was synthesized by secondary amine bond formation between cyanuric chloride and 5-amino tetrazole monohydrate in the presence of triethylamine (**Scheme 4.3**) as a white-colored solid product. The synthesis of **G8**, **TNBTA**, and **TABTA** was confirmed by ^{1}H, ^{13}C, and FT-IR spectroscopy.

4.2 Reaction schemes

4.2.1 Synthesis of TNBTA

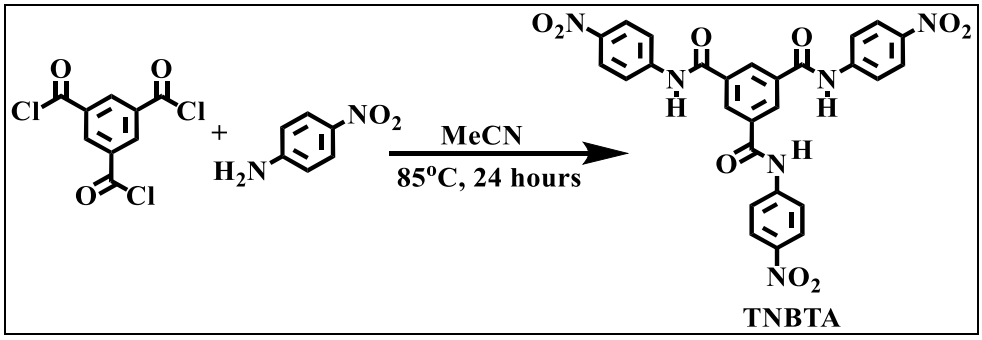

Scheme 4.1: Synthetic scheme for **TNBTA** synthesis

4.2.2 Synthesis of gelator component TABTA

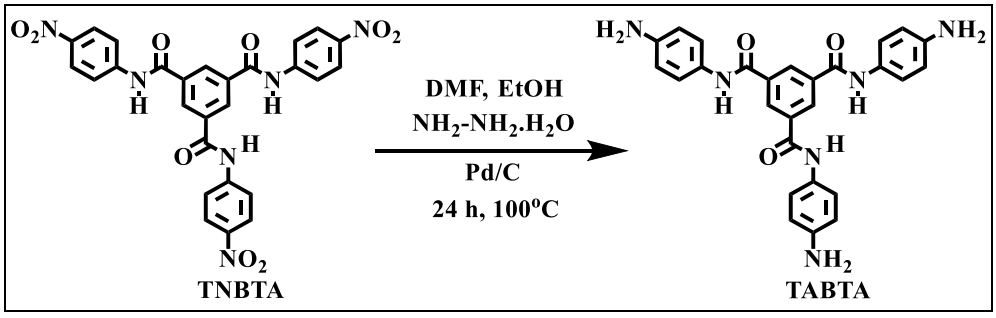

Scheme 4.2: Synthetic scheme for **TABTA** synthesis

4.2.3 Synthesis of gelator component G8

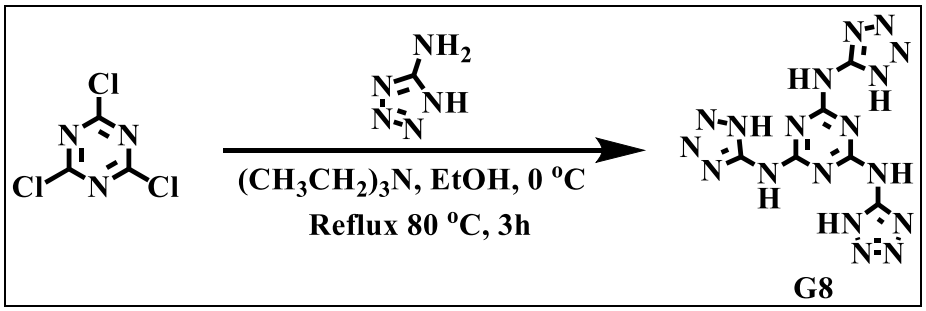

Scheme 4.3: Synthetic scheme for **G8** synthesis

4.3 Solubility of G8-TABTA and its Gelation Behaviour

The **G8-TABTA** mixture has been checked for solubility in various solvents and it was found to be soluble in DMSO and DMF, as shown in the table below (**Table 4.1**). The organogel was fabricated by dissolving 0.05 mmol (16 mg) of **G8** and 0.05 mmol (24 mg) of **TABTA** in 750 µL DMF by heating for 4-5 minutes, that upon subsequent homogeneous addition of 250 µL Milli-Q water, formed a yellowish-brown colored organogel instantly. To determine the critical gel concentration (CGC) value of organogel **G8-TABTA**, different proportions of **G8** and **TABTA** were taken from 0.01:0.01 mmol to 0.06:0.06 mmol with a constant ratio of DMF and Milli-Q water. It was observed that 0.03 mmol (10 mg) of **G8** and 0.03 mmol (14 mg) of **TABTA** on 500:100 µL of DMF: H_2O forms a weak organogel. Therefore, the critical gel concentration of **G8-TABTA organogel** was 40 $mgmL^{-1}$. The gel formation was confirmed by the conventional test tube inversion method.

Table 4.1: Solubility of organogel **G8-TABTA** in various solvents

Solvent	**Solubility (G8-TABTA)**	**Gelation**	**Solvent**	**Solubility (G8-TABTA)**	**Gelation**
CCl_4	Insoluble	-	**Hexane**	Insoluble	-
Methanol	Insoluble	-	**DMF**	**Soluble**	**Gel**
DMSO	Soluble	-	**Acetone**	Insoluble	-
Acetonitrile	Insoluble	-	**Toluene**	Insoluble	-
Ethanol	Insoluble	-	**DCM**	Insoluble	-
Ethyl acetate	Insoluble	-	**Benzene**	Insoluble	-

Table 4.2: Optimization Table for **G8-TABTA** gelation

mmol of G8 (250µL DMF)	**mmol of TABTA (250µL DMF)**	**Ratio of G8 and TABTA**	**DMF: H_2O (µL)**	**Gelation**
0.01	0.01	1:1	500: 100	No gel
0.02	0.02	1:1	500: 100	No gel
0.03	0.03	1:1	500: 100	Weak gel
0.04	0.04	1:1	500: 100	**Gel**
0.05	0.05	1:1	500: 100	**Gel**
0.06	0.06	1:1	500: 100	**Gel**

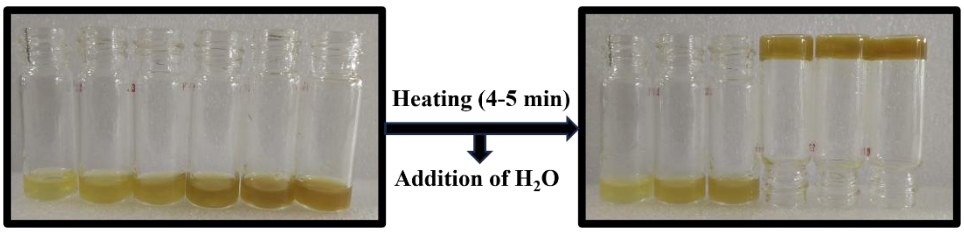

Figure 4.1: Optimization for **G8-TABTA** gelation

Table 4.3: Optimization Table for **G8-TABTA** gelation with varying **G8** proportions

mmol of G8 (250µL DMF)	**mmol of TABTA (250µL DMF)**	**Ratio of G8 and TABTA**	**DMF: H_2O (µL)**	**Gelation**
0.025	0.05	1:2	500: 100	No gel
0.05	0.05	1:1	500: 100	**Gel**
0.075	0.05	3:2	500: 100	**Gel**
0.10	0.05	2:1	500: 100	**Gel**
0.125	0.05	5:2	500: 100	**Gel**

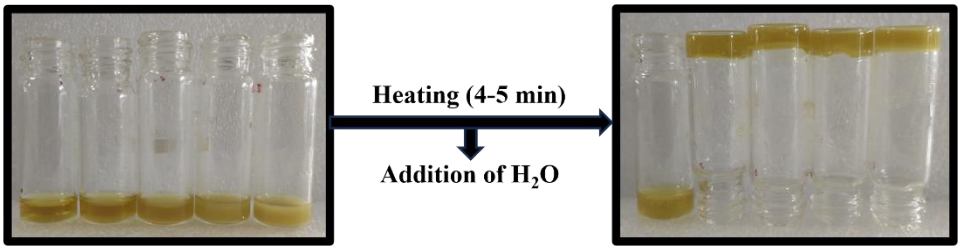

Figure 4.2: Optimization for **G8-TABTA** gelation with varying **G8** proportions

Table 4.4: Optimization Table for **G8-TABTA** gelation with varying **TABTA** proportions

mmol of G8 (250µL DMF)	mmol of TABTA (250µL DMF)	Ratio of G8 and TABTA	DMF: H_2O (µL)	Gelation
0.05	0.025	2:1	500: 100	**Gel**
0.05	0.05	1:1	500: 100	**Gel**
0.05	0.075	2:3	500: 100	**Gel**
0.05	0.10	1:2	500: 100	**Gel**
0.05	0.125	2:5	500: 100	**Gel**

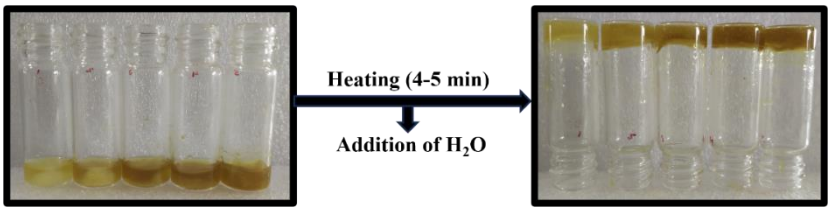

Figure 4.3: Optimization for **G8-TABTA** gelation with varying **TABTA** proportions

Table 4.5: Optimization Table for **G8-TABTA** gelation with varying solvent proportions

mmol of G8 (250µL DMF)	mmol of TABTA (250µL DMF)	Ratio of G8 and TABTA	DMF: H_2O (µL)	Gelation
0.05	0.05	1:1	500: 100	**Gel**
0.05	0.05	1:1	500: 250	**Gel**
0.05	0.05	1:1	750: 250	**Gel**
0.05	0.05	1:1	500: 500	No gel
0.05	0.05	1:1	500: 1000	No gel
0.05	0.05	1:1	1000: 250	No gel
0.05	0.05	1:1	1500:250	No gel

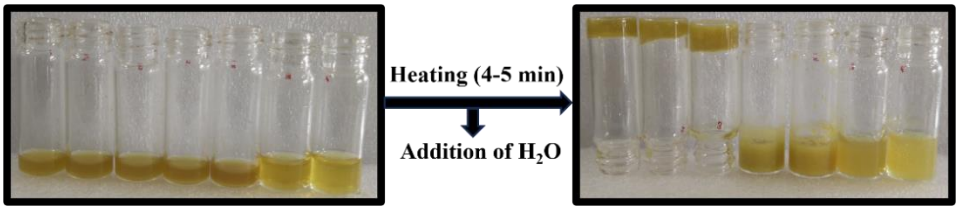

Figure 4.4: Optimization for **G8-TABTA** gelation with varying solvent proportions

4.4 Gelation behavior of G8-TABTA with metal salts

The **G8-TABTA metallogels** were fabricated by homogeneously adding 0.05 mmol of **perchlorate salts** of Ag^{+}, Fe^{3+}, Fe^{2+}, Co^{2+}, Ni^{2+}, Cu^{2+}, and Zn^{2+} dissolved in 250 µL Milli-Q water into a solution comprising 0.05 mmol each of **G8** (16 mg) and **TABTA** (24 mg) solubilized in 750 µL DMF. The gel formation was observed with all metal salts mentioned except for Ni^{2+} perchlorate salt which was confirmed by the conventional test tube inversion method (**Table 4.6**) and (**Figure 4.5**).

Table 4.6: Gelation behavior of **G8-TABTA** with metal salts

mmol of G8 (500µL DMF)	**mmol of TABTA (250µL DMF)**	**Metal ion (0.05 mmol in 250µL H_2O)**	**The ratio of G8, TABTA, and metal ions**	**DMF: H_2O (µL)**	**Gelation**
0.05	0.05	Ag^{+}	1:1:1	750: 250	**Gel**
0.05	0.05	Fe^{3+}	1:1:1	750: 250	**Gel**
0.05	0.05	Fe^{2+}	1:1:1	750: 250	**Gel**
0.05	0.05	Co^{2+}	1:1:1	750: 250	**Gel**
0.05	0.05	Ni^{2+}	1:1:1	750: 250	No gel
0.05	0.05	Cu^{2+}	1:1:1	750: 250	**Gel**
0.05	0.05	Zn^{2+}	1:1:1	750: 250	**Gel**

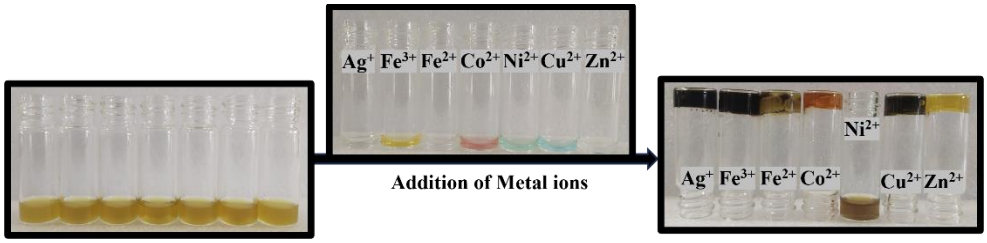

Figure 4.5: Gelation behavior of **G8-TABTA** with metal salts

Further, the gelation condition of **Ag and Zn perchlorate metallogel** of **G8-TABTA** was optimized (**Table 4.7**) and (**Table 4.8**), respectively.

Table 4.7: Optimization Table for silver perchlorate metallogel of **G8-TABTA**

mmol of G8 (500µL DMF)	mmol of TABTA (250µL DMF)	mmol of Ag^+ (250µL H_2O)	Ratio of G8, TABTA and Ag^+	DMF: H_2O (µL)	Gelation
0.05	0.05	0.10	1:1:2	750: 250	**Gel**
0.05	0.05	0.20	1:1:4	750: 250	**Gel**
0.05	0.05	0.30	1:1:6	750: 250	**Gel**
0.05	0.05	0.40	1:1:8	750: 250	**Gel**

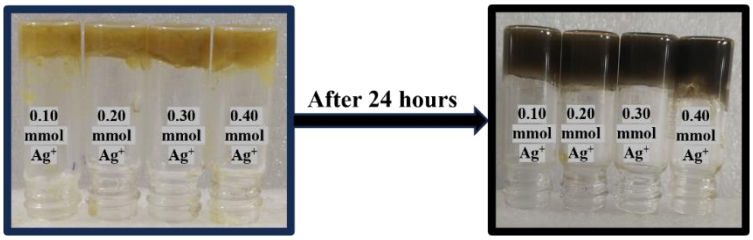

Figure 4.6: Optimization for silver perchlorate metallogel of **G8-TABTA**

Table 4.8: Optimization Table for zinc perchlorate metallogel of **G8-TABTA**

mmol of G8 (500µL DMF)	mmol of TABTA (250µL DMF)	mmol of Zn^{2+} (250µL H_2O)	Ratio of G8, TABTA and Zn^{2+}	DMF: H_2O (µL)	Gelation
0.05	0.05	0.025	1:1:0.5	750: 250	**Gel**
0.05	0.05	0.05	1:1:1	750: 250	**Gel**
0.05	0.05	0.075	1:1:1.5	750: 250	No gel
0.05	0.05	0.10	1:1:2	750: 250	No gel

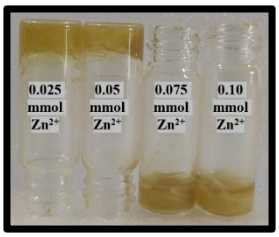

Figure 4.7: Optimization for zinc perchlorate metallogel of **G8-TABTA**

4.5 Solubility of TABTA-Ibuprofen and its Gelation Behaviour

The **TABTA-Ibuprofen** mixture has been checked for solubility in various solvents and it was found to be soluble in DMSO and DMF, as shown in the table below (**Table 4.9**). The organogel was fabricated by dissolving 0.05 mmol (24 mg) of **TABTA** and 0.15 mmol (34 mg) of the **sodium salt of ibuprofen** in 950 µL DMSO by heating followed by the addition of 50 µL Milli-Q water on sonication for 2-3 minutes forms a bright yellow colored organogel. To determine the critical gel concentration (CGC) value of organogel **TABTA-Ibp**, constant proportions of **TABTA** and **sodium salt of ibuprofen** 0.05:0.15 mmol were taken for a varying ratio of DMSO and Milli-Q water from 950:50 µL to 2450:50 µL. It was observed that 0.05 mmol (24 mg) of **TABTA** and 0.15 mmol (34 mg) of the **sodium salt of ibuprofen** on 1950:50 µL of DMSO: H_2O forms a weak organogel. Therefore, the critical gel concentration of **TABTA-Ibp organogel** was 29 $mgmL^{-1}$. The gel formation was confirmed by the conventional test tube inversion method.

Table 4.9: Solubility of organogel **TABTA-Ibuprofen** in various solvents

Solvent	**Solubility (TABTA-Ibuprofen)**	**Gelation**	**Solvent**	**Solubility (TABTA-Ibuprofen)**	**Gelation**
CCl_4	Insoluble	-	**Hexane**	Insoluble	-
Methanol	Insoluble	-	**DMF**	**Soluble**	**Gel**
DMSO	**Soluble**	**Gel**	**Acetone**	Insoluble	-
Acetonitrile	Insoluble	-	**Toluene**	Insoluble	-
Ethanol	Insoluble	-	**DCM**	Insoluble	-
Ethyl acetate	Insoluble	-	**Benzene**	Insoluble	-

Table 4.10: Optimization Table for **TABTA-Ibuprofen** gelation

mmol of TABTA (500µL DMSO)	**mmol of Ibuprofen (450µL DMSO)**	**Ratio of TABTA and Ibuprofen**	**DMSO: H_2O (µL)**	**Gelation on sonication**
0.05	0.05	1:1	950: 50	No gel
0.05	0.10	1:2	950: 50	Partial gel
0.05	0.15	1:3	950: 50	**Gel**

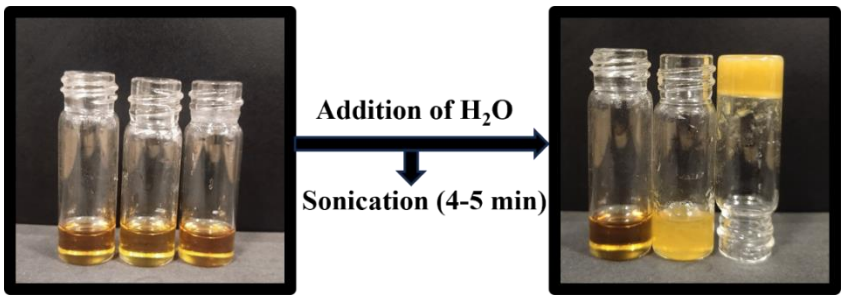

Figure 4.8: Optimization for **TABTA-Ibuprofen** gelation

Table 4.11: Optimization Table for gelation with fixed solvent proportions for **TABTA-Ibuprofen** gelation

mmol of TABTA (500µL DMSO)	**mmol of Ibuprofen (450µL DMSO)**	**Ratio of TABTA and Ibuprofen**	**DMSO: H_2O (µL)**	**Gelation on sonication**
0.01	0.03	1:3	950: 50	No gel
0.02	0.06	1:3	950: 50	No gel
0.03	0.09	1:3	950: 50	**Gel**
0.04	0.12	1:3	950: 50	**Gel**
0.05	0.15	1:3	950: 50	**Gel**

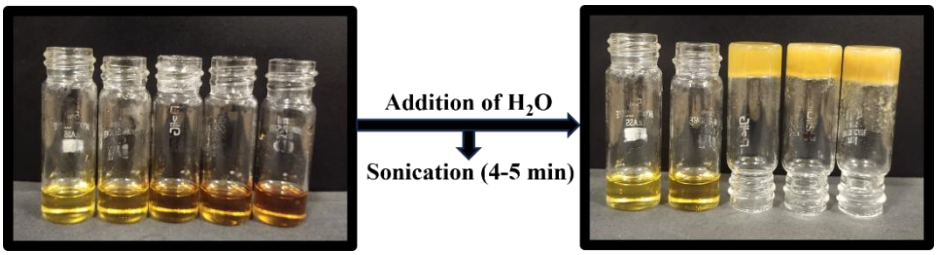

Figure 4.9: Optimization for gelation with fixed solvent proportions for **TABTA-Ibuprofen** gelation

Table 4.12: Optimization Table for **TABTA-Ibuprofen** gelation with varying solvent proportions

mmol of TABTA	mmol of Ibuprofen	Ratio of TABTA and Ibuprofen	DMSO: H_2O (µL)	Gelation on sonication
0.05	0.15	1:3	950:50	**Gel**
0.05	0.15	1:3	1450:50	**Gel**
0.05	0.15	1:3	1950:50	**Gel**
0.05	0.15	1:3	2450:50	No Gel

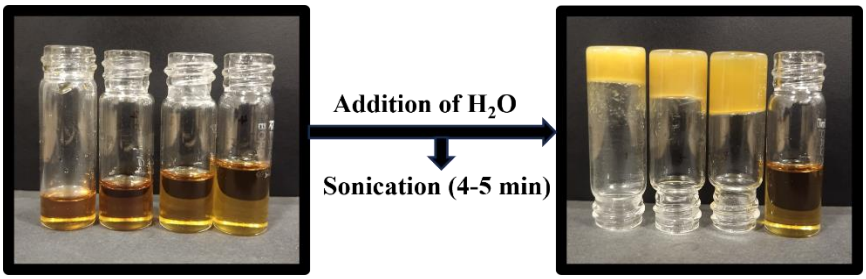

Figure 4.10: Optimization for **TABTA-Ibuprofen** gelation with varying solvent proportions

4.6 Gelation behavior of TABTA-Ibuprofen with metal salts

The **G8-Ibuprofen metallogel** was fabricated by uniformly adding 250 µL Milli-Q water into a solution comprising 0.05 mmol of **G8** (16 mg), 0.15 mmol of the **sodium salt of ibuprofen** (34 mg) and 0.15 mmol of **perchlorate salts** of Ag^{+}, Fe^{3+}, Fe^{2+}, Co^{2+}, Ni^{2+}, Cu^{2+}, and Zn^{2+} solubilized in 1500 µL DMSO. The gel formation was observed specifically with Ag-perchlorate salt amongst all metal salts mentioned, which was confirmed by the conventional test tube inversion method (**Table 4.13**) and (**Figure 4.11**).

Table 4.13: Gelation behavior of **TABTA-Ibuprofen** with metal salts

mmol of TABTA (500µL DMSO)	**mmol of Ibuprofen (500µL DMSO)**	**Metal ion (0.15 mmol in 500µL DMSO)**	**The ratio of TABTA, Ibuprofen, and metal ions**	**DMSO: H_2O (µL)**	**Gelation on sonication**
0.05	0.15	Ag^{+}	1:3:3	1500: 250	**Gel**
0.05	0.15	Fe^{3+}	1:3:3	1500: 250	No Gel
0.05	0.15	Fe^{2+}	1:3:3	1500: 250	No Gel
0.05	0.15	Co^{2+}	1:3:3	1500: 250	No Gel
0.05	0.15	Ni^{2+}	1:3:3	1500: 250	No Gel
0.05	0.15	Cu^{2+}	1:3:3	1500: 250	No Gel
0.05	0.15	Zn^{2+}	1:3:3	1500: 250	No Gel

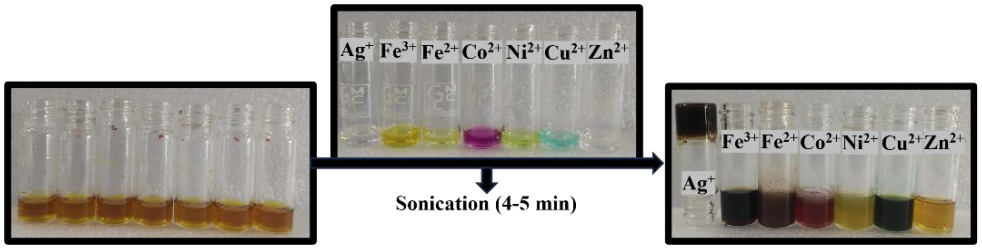

Figure 4.11: Gelation behavior of **G8-Ibuprofen** with metal salts

Further, the **Ag perchlorate metallogel** gelation condition of **TABTA-Ibuprofen** was optimized (**Table 4.14**).

Table 4.14: Optimization Table for silver perchlorate metallogel of **TABTA-Ibuprofen**

mmol of TABTA (500µL DMSO)	mmol of Ibuprofen (500µL DMSO)	mmol of Ag^+ (500µL DMSO)	Ratio of TABTA, Ibuprofen and Ag^+	DMSO: H_2O (µL)	Gelation on sonication
0.05	0.15	0.15	1:3:3	1500: 250	**Gel**
0.05	0.15	0.20	1:3:4	1500: 250	**Gel**
0.05	0.15	0.25	1:3:5	1500: 250	**Gel**
0.05	0.15	0.30	1:3:6	1500: 250	**Gel**

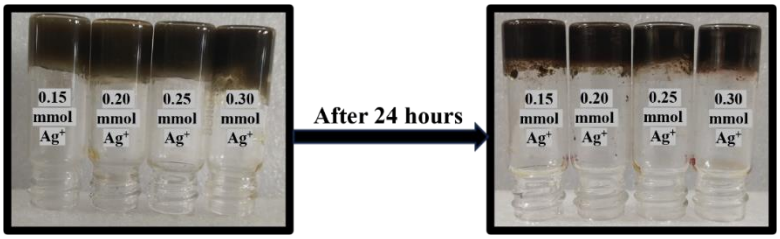

Figure 4.12: Optimization for silver perchlorate metallogel of **TABTA-Ibuprofen**

4.7 Characterization

4.7.1 Mass Spectra

ESI-MS spectra characterized the synthesized compounds G8 and TABTA. The gelator component **G8** shows a base peak at m/z= 329.0753 (in negative mode) (**Figure 4.13**) and **TABTA** shows a base peak at m/z=481.2042 (in positive mode) (**Figure 4.14**).

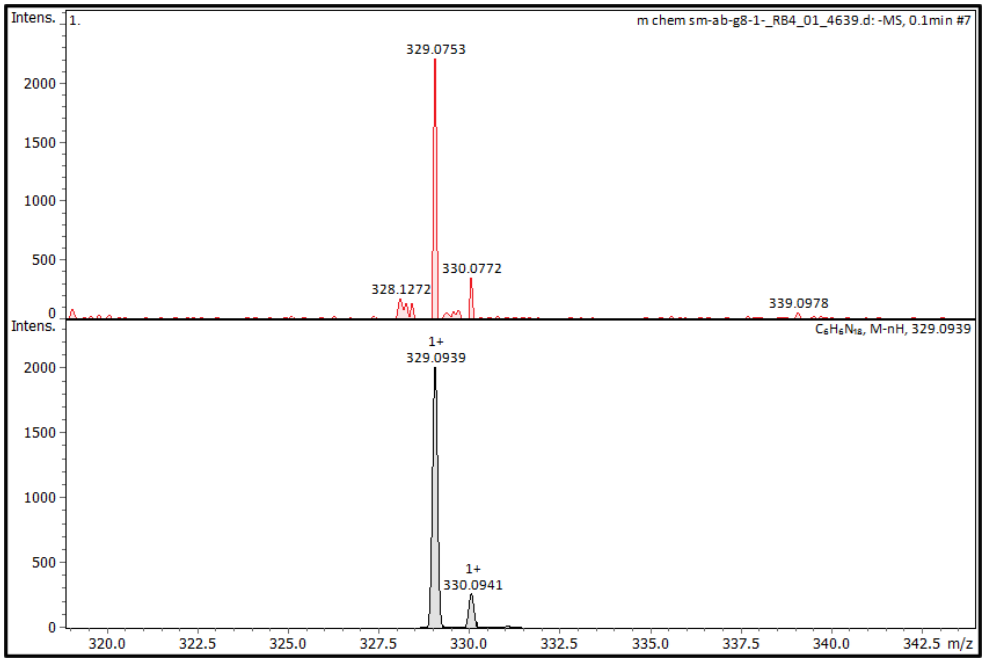

Figure 4.13: Mass spectrum of **G8**; ESI-MS (m/z) $C_6H_6N_{18}$: Calculated for $[C_6H_6N_{18}\text{-}H]^-$: 329.0939; Found: 329.0753

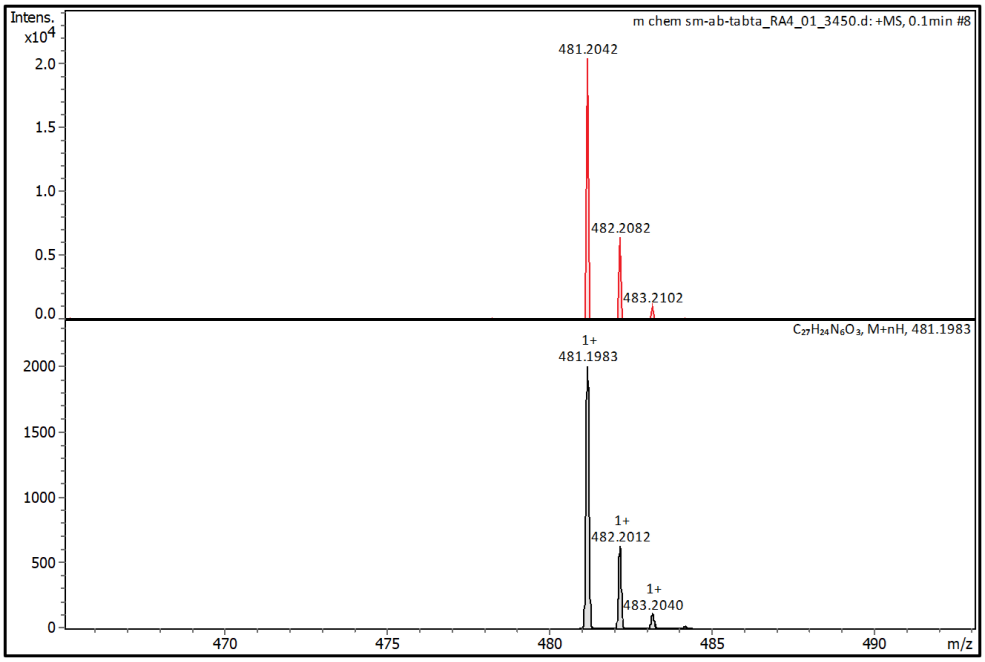

Figure 4.14: Mass spectrum of gelator component **TABTA**; ESI-MS (m/z) $C_{27}H_{24}N_6O_3$: Calculated for $[C_{27}H_{24}N_6O_3\text{+}H]^+$: 481.1983; Found: 481.2042

4.7.2 NMR Spectra

NMR data for **TNBTA** and **TABTA** molecules matched well with their proposed structures. The NMR was recorded with samples dissolved in DMSO-d_6. ^{1}H NMR peaks in the δ 8.82-6.45 region correspond to the aromatic protons and a highly deshielded broad peak after 10 ppm corresponds to the amide N-H proton of **TNBTA** and **TABTA**.[49] A peak at 4.86 ppm corresponds to the amine proton of **TABTA**. ^{13}C NMR peaks in the δ 110-150 region correspond to the aromatic carbons and a peak above 160 ppm corresponds to the carbonyl carbon of **TNBTA** and **TABTA**.[50]

4.7.1.1 NMR Spectra of G8

^{13}C NMR (125MHz, 298K, DMSO-d_6) δ, ppm: 162.43, 153.99. (**Figure 4.15**)

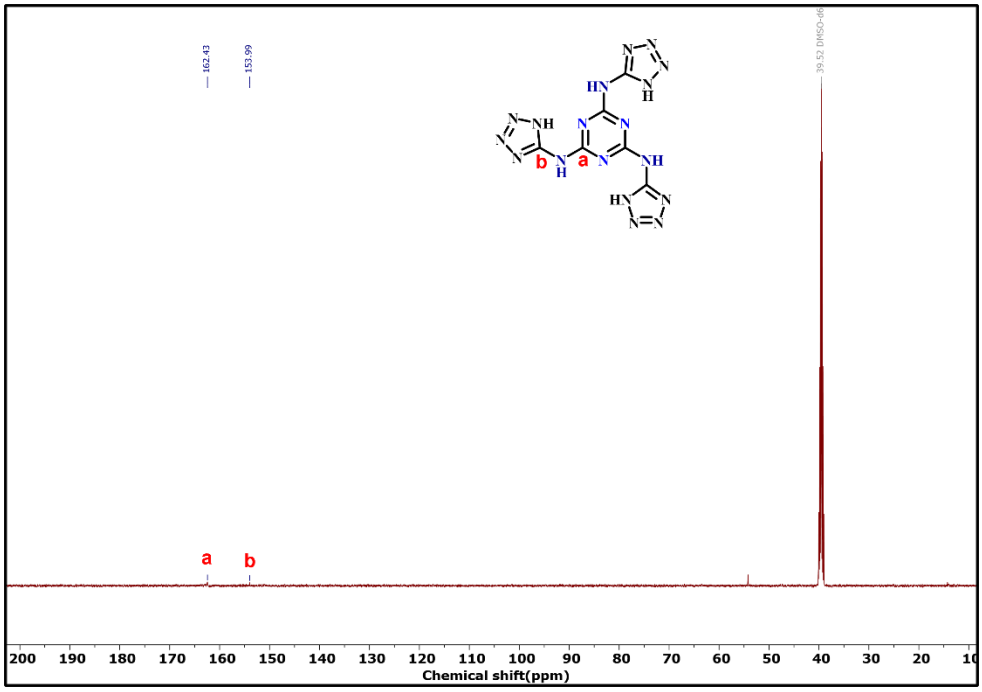

Figure 4.15: ^{13}C NMR of **G8**

4.7.1.2 NMR Spectra of TNBTA

^{1}H NMR (500MHz, 298K, DMSO-d_6) δ, ppm: 11.22 (s, 1H, H_d), 8.82 (s, 1H, CH_a), 8.30 (d, 2H, CH_c), 8.14 (d, 2H, CH_b). (**Figure 4.16**) ^{13}C NMR (125MHz, 298K, DMSO-d_6) δ, ppm: 164.76, 144.99, 142.61, 134.63, 130.63, 124.70, 119.8. (**Figure 4.17**)

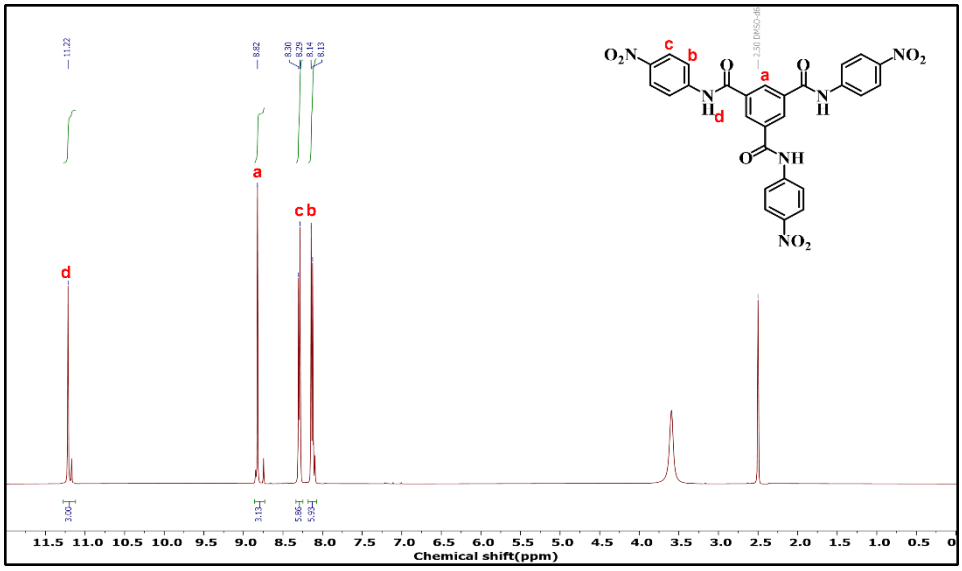

Figure 4.16: ^{1}H NMR of **TNBTA**

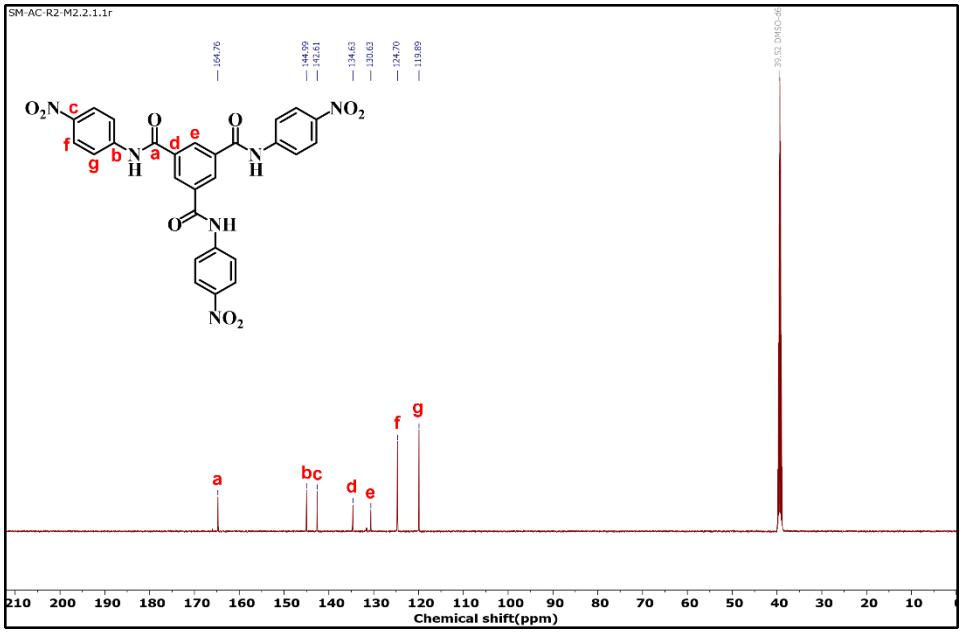

Figure 4.17: ^{13}C NMR of **TNBTA**

4.7.1.3 NMR Spectra of gelator component TABTA

^{1}H NMR (500MHz, 298K, DMSO-d_6) δ, ppm: 10.03 (s, 1H, H_a), 8.45 (s, 1H, CH_b), 7.30 (d, 2H, CH_c), 6.45 (d, 2H, CH_d), 4.86 (s, 2H, NH_e). (**Figure 4.18**) ^{13}C NMR (125MHz, 298K, DMSO-d_6) δ, ppm: 163.83, 145.41, 135.74, 128.97, 127.94, 122.13, 113.74. (**Figure 4.19**)

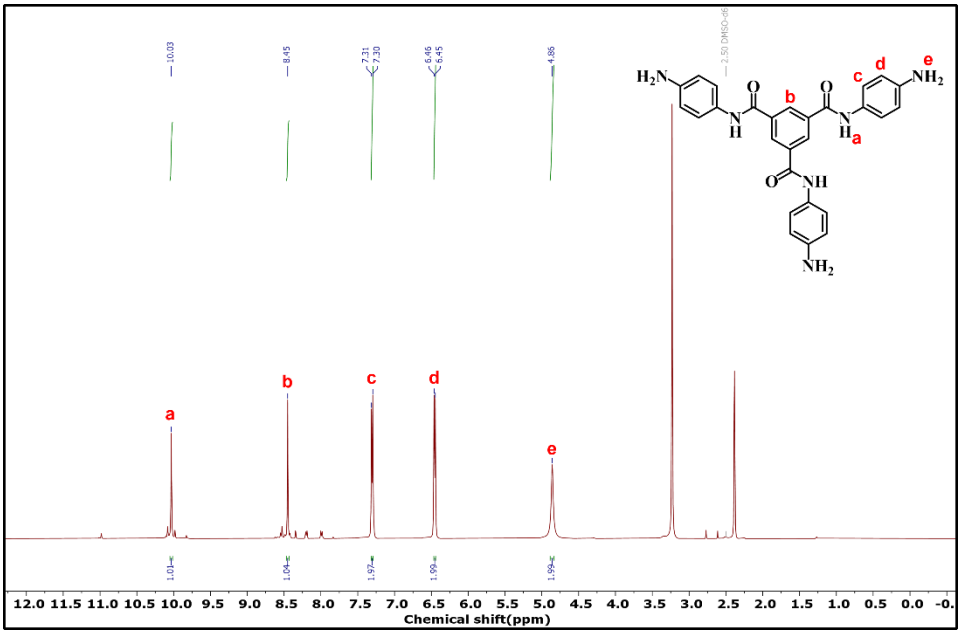

Figure 4.18: ^{1}H NMR of gelator component **TABTA**

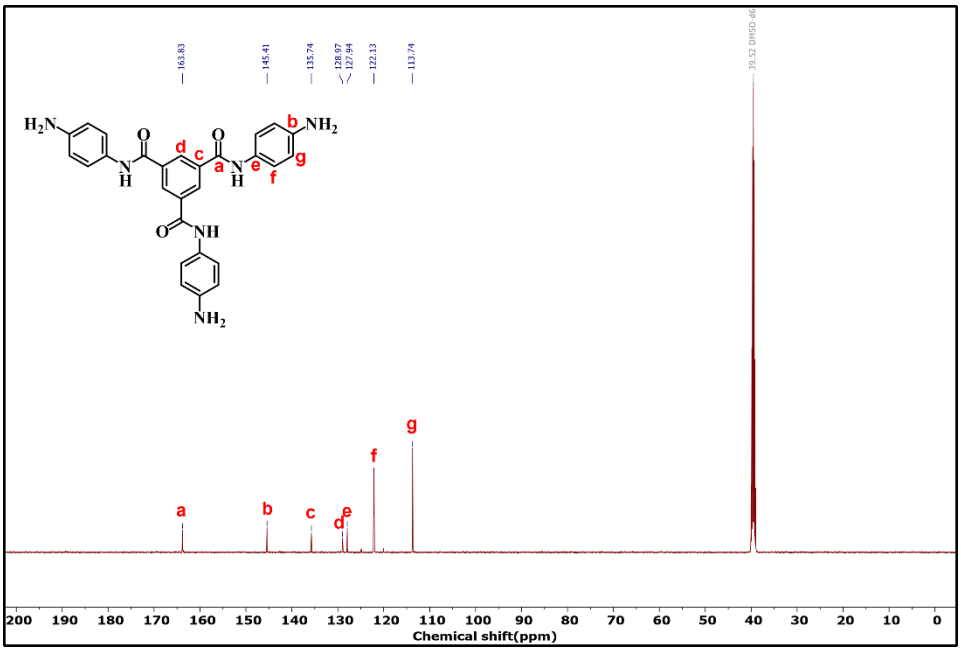

Figure 4.19: ^{13}C NMR of gelator component **TABTA**

4.7.3 FT-IR Spectra

The bands in the IR spectra matched well with the expected characteristic bands of various functional groups of **G8**, **TNBTA**, and **TABTA**. For the gelator component, **G8** (**Figure 4.20 (a)**) notable peaks included a broad one at 2900 cm^{-1} indicating N-H stretching, sharp peaks at 1637 cm^{-1} for C=N stretching, 1518 cm^{-1} for N-H bending, 1415 cm^{-1} for cyclic -C-N=C-

group, and 1235 cm^{-1} for C-N stretching.[48] **TNBTA** (**Figure 4.20 (b)**) and **TABTA** (**Figure 4.20 (c)**) exhibited similar patterns, with broad bands at 3396 cm^{-1} and 3320 cm^{-1} for N-H stretching,[51] along with sharp peaks at 1690 cm^{-1} and 1639 cm^{-1} respectively for C=O amide stretching.[52] Additionally, **TNBTA** displayed a distinct peak at 1545 cm^{-1} corresponding to -NO_2 stretching.

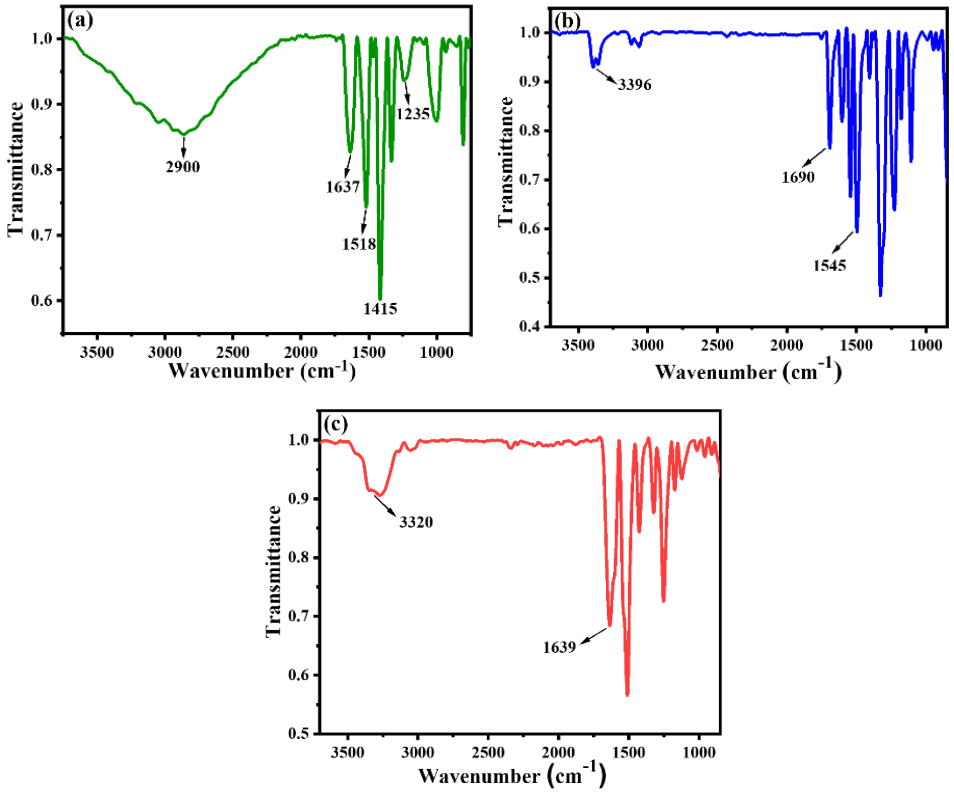

Figure 4.20: IR spectrum of (a) **G8**, (b) **TNBTA**, and (c) **TABTA**

As already reported, **G8** shows an IR band at 1637 cm^{-1} for C=N stretching, 1520 cm^{-1} for N-H bending, and 1234 cm^{-1} for C-N stretching.[48] The other gelator component **TABTA** shows IR bands at 1639 cm^{-1} for C=O stretching, 1512 cm^{-1} for amide N-H bending, and 1255 cm^{-1} for C-N stretching. Upon analyzing the **G8-TABTA** xerogel, the amide N-H bending was observed at 1508 cm^{-1}, and C=O and C-N stretching frequencies were observed at 1645 cm^{-1} and 1247 cm^{-1} respectively. These shifts in the wavenumber indicate the presence of some non-covalent interactions between the gelator components **G8** and **TABTA** (**Figure 4.21 (a)**).

Subsequently, the **sodium salt of ibuprofen** shows two distinct IR peaks at 1547 cm^{-1} and 1410 cm^{-1} for asymmetric and symmetric CO_2^- stretch respectively.[53] Thus, upon examining the **TABTA-Ibp** xerogel those peaks were observed to shift towards 1508 cm^{-1} and 1400 cm^{-1} for asymmetric and symmetric CO_2^- stretch respectively. This downward shift in wavenumber indicates the presence of hydrogen bonding between the components **TABTA** and **sodium salt of ibuprofen** (**Figure 4.21 (b)**).

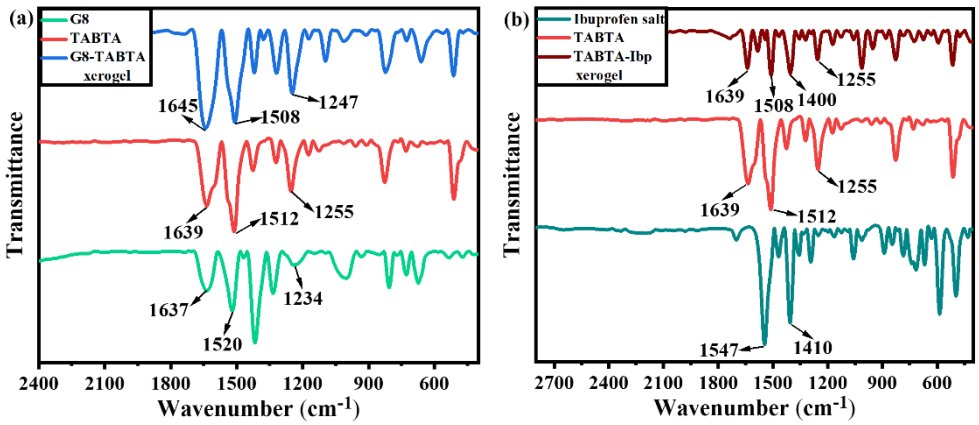

Figure 4.21: FT-IR spectra of (a) **G8**, **TABTA,** and **G8-TABTA** xerogel (b) **Ibuprofen salt**, **TABTA,** and **TABTA-Ibp** xerogel

The FT-IR analyses for **G8-TABTA-Ag** xerogel, **G8-TABTA-Zn** xerogel, and **TABTA-Ibp-Ag** xerogel were conducted where for **G8-TABTA-Ag** xerogel the major peaks were observed at 3370 cm^{-1} and 2938 cm^{-1} for N-H stretching, 1645 cm^{-1} for C=O/C=N stretching, 1508 cm^{-1} for the N-H bending, and 1247 cm^{-1} for C-N stretch (**Figure 4.22 (a)**). Similarly, for **G8-TABTA-Zn** xerogel, the major peaks were observed at 3308 cm^{-1} and 2936 cm^{-1} for N-H stretching, 1647 cm^{-1} for C=O/C=N stretching, 1508 cm^{-1} for the N-H bending, and 1247 cm^{-1} for C-N stretch (**Figure 4.22 (b)**). Next, for **TABTA-Ibp-Ag** xerogel the major peaks were observed at 3326 cm^{-1} for hydrogen-bonded O-H stretching, 2958 cm^{-1} for N-H stretching, 1666 cm^{-1} for C=O amide stretching, 1520 cm^{-1} and 1415 cm^{-1} for asymmetric and symmetric CO_2^- stretching respectively, and 1249 cm^{-1} for C-N stretch (**Figure 4.22 (c)**). All these shifts in the wavenumber for the xerogels of corresponding metallogels might be predominantly due to different non-covalent interactions within the distinct metallogels.

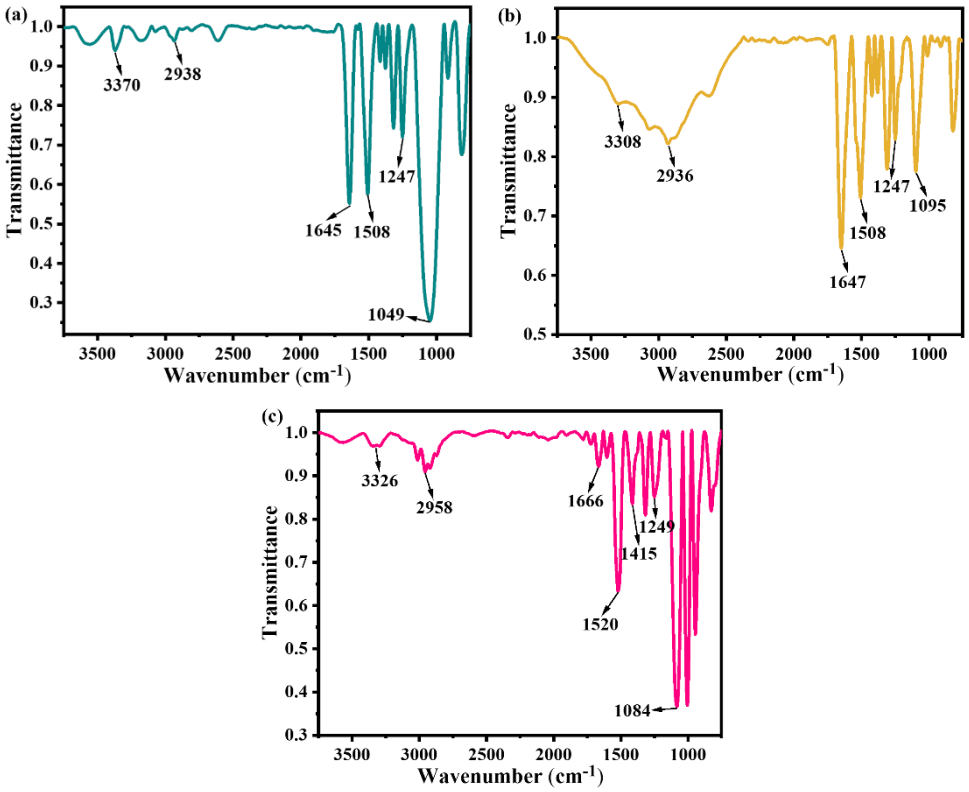

Figure 4.22: IR spectrum of (a) **G8-TABTA-Ag** xerogel, (b) **G8-TABTA-Zn** xerogel, and (c) **TABTA-Ibp-Ag** xerogel

4.7.4 Rheological Analysis

The rheological analysis assessed the gels' strength and sol-gel transition characteristics.

4.7.4.1 G8-TABTA organogel and its silver and zinc metallogel

For the **G8-TABTA** organogel, the average storage modulus (G') was 137 Pa. During the experiment, initially, the storage modulus (G') was found to be greater than the loss modulus (G") in most of the ranges. Still, upon G' and G" deviated from linearity and the crossover point was observed at 70% of the strain value (**Figure 4.23**) and angular frequency-dependent storage modulus (G') and loss modulus (G") parameters were examined for the organogel to confirm their viscoelastic properties (**Figure 4.24**).

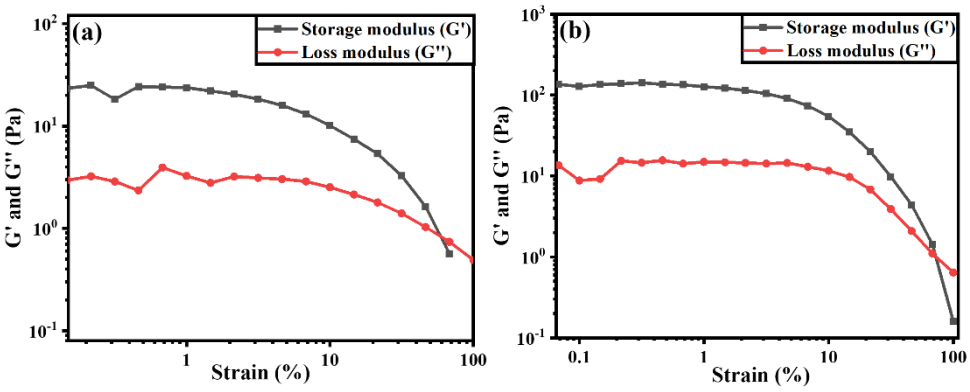

Figure 4.23: Linear viscoelastic (LVE) range of **G8-TABTA** organogel (a) critical gel concentration and (b) most stable organogel

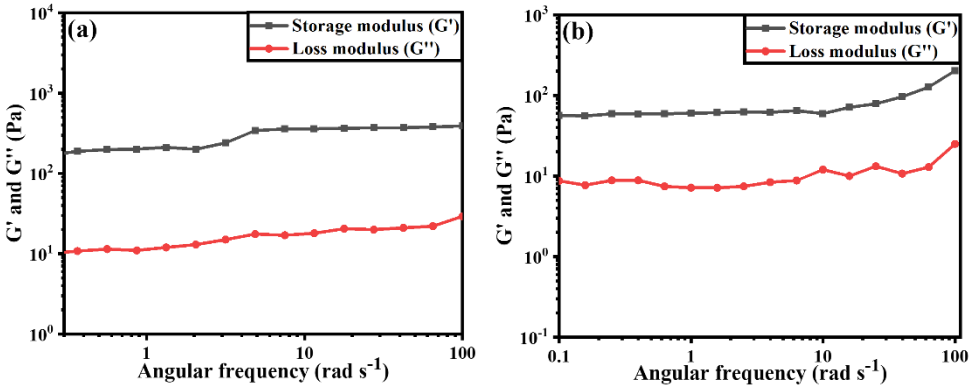

Figure 4.24: Angular frequency sweep of **G8-TABTA** organogel (a) critical gel concentration and (b) most stable organogel

Subsequently, **G8-TABTA** metallogels were prepared using the silver and zinc perchlorate salts. The storage modulus (G') was measured to be within the range of 350-1500 Pa for **G8-TABTA-Ag** (**Figure 4.25**) and 550-2450 Pa for **G8-TABTA-Zn** (**Figure 4.27**) metallogels, with a crossover point observed at 110% and 97%, respectively. Additionally, angular frequency-dependent storage modulus (G') and loss modulus (G'') parameters were examined for the metallogels to confirm their viscoelastic properties as depicted in (**Figure 4.26**) and (**Figure 4.28**) respectively.

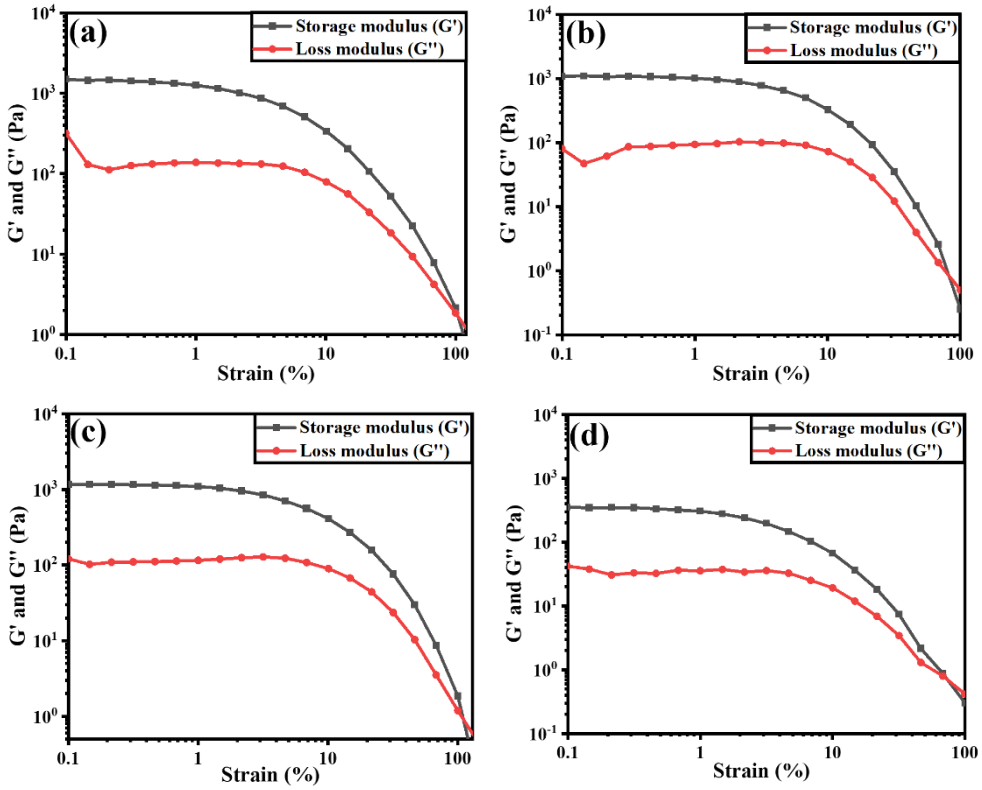

Figure 4.25:Linear viscoelastic (LVE) range of **G8-TABTA-Ag** metallogel for varying concentrations of Ag-perchlorate salt from 0.10 to 0.40 mmol

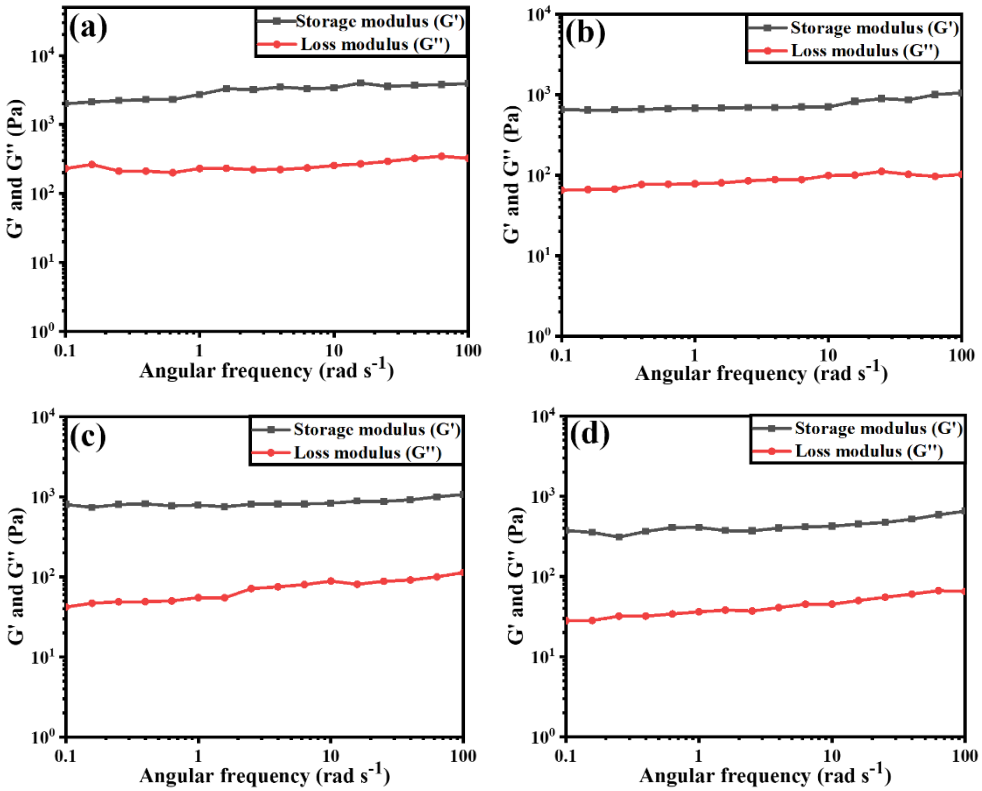

Figure 4.26: Angular frequency sweep of **G8-TABTA-Ag** metallogel for varying concentrations of Ag-perchlorate salt from 0.10 to 0.40 mmol

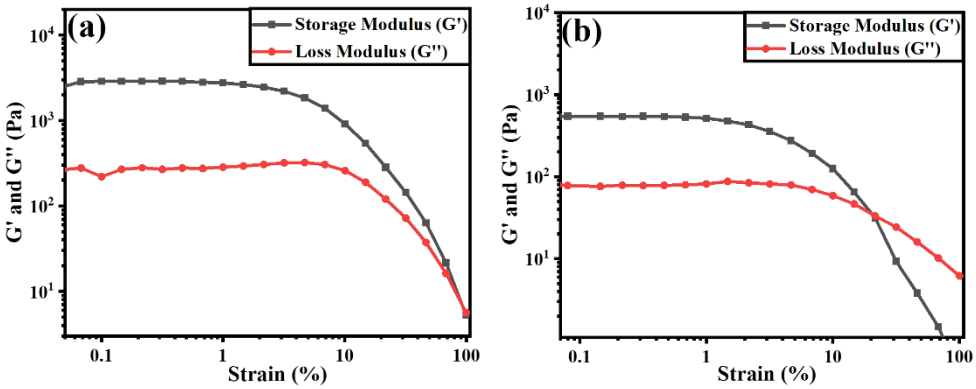

Figure 4.27: Linear viscoelastic (LVE) range of **G8-TABTA-Zn** metallogel for varying concentrations of Zn-perchlorate salt from 0.025 to 0.05 mmol

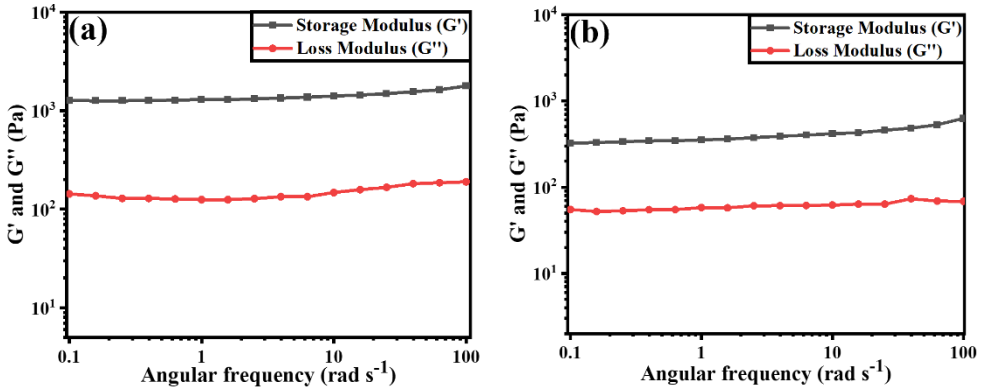

Figure 4.28: Angular frequency sweep of **G8-TABTA-Zn** metallogel for varying concentrations of Zn-perchlorate salt from 0.025 to 0.05 mmol

Additionally, the rheological time-oscillation strain-sweep experiment (thixotropic measurement) was performed for the **G8-TABTA** organogel (**Figure 4.29** (a)) and its silver and zinc metallogels, **G8-TABTA-Ag** (**Figure 4.29** (b)) and **G8-TABTA-Zn** (**Figure 4.29** (c)) respectively. The organogel and metallogels underwent cyclic strain, starting with a low strain of 0.5% shear strain where the storage modulus (G') exceeded the loss modulus (G''). Over time, the strain was incrementally increased to 100%, leading to a transformation of the metallogel into a quasi-liquid state (sol), as observed in time sweep plots where G' became less than G''. Upon the removal of high strain, the metallogels reverted to their original viscoelastic behavior, with G' surpassing G'' again. This reversible process was repeated multiple times for all synthesized metallogels, demonstrating their thixotropic characteristics.

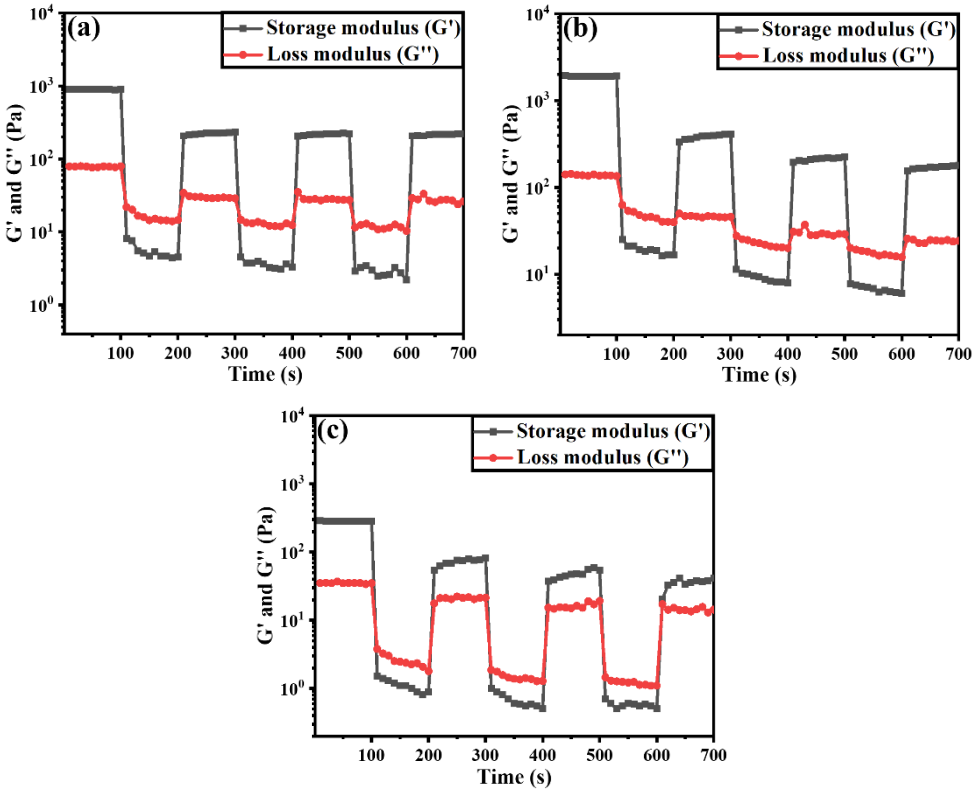

Figure 4.29: Time-oscillation strain-sweep experiment (thixotropic behavior) of (a) **G8-TABTA** organogel, (b) **G8-TABTA-Ag** metallogel, and (c) **G8-TABTA-Zn** metallogel

4.7.4.2 TABTA- Ibp organogel and its silver metallogel

For **TABTA-Ibp** organogel, the average storage modulus (G') was 2084 Pa. During the experiment, initially, the storage modulus (G') was found to be greater than the loss modulus (G'') in most of the ranges. Still, upon increasing the strain, the values of G' and G'' deviated from linearity. The crossover point was observed at 2% of the strain value (**Figure 4.30**) and angular frequency-dependent storage modulus (G') and loss modulus (G'') parameters were examined for the organogel to confirm their viscoelastic properties (**Figure 4.31**).

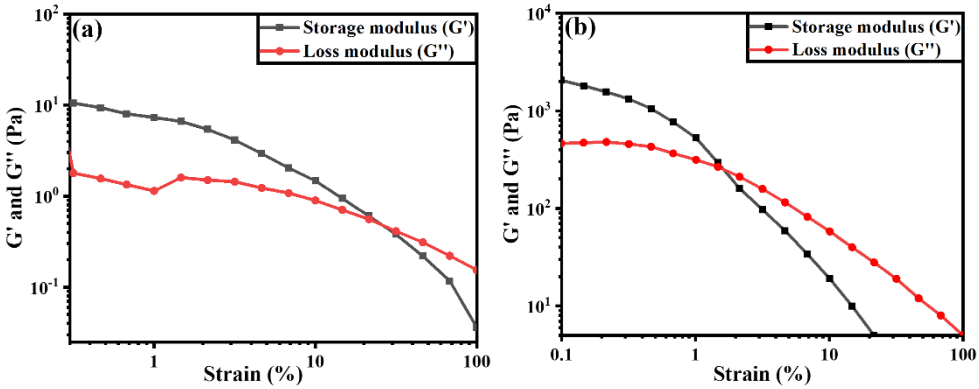

Figure 4.30: Linear viscoelastic (LVE) range of **TABTA-Ibp** organogel (a) critical gel concentration and (b) most stable organogel.

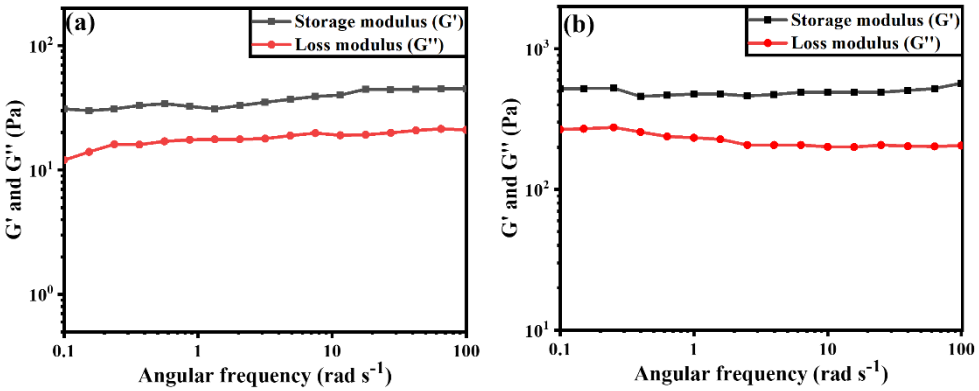

Figure 4.31: Angular frequency sweep of **TABTA-Ibp** organogel (a) critical gel concentration and (b) most stable organogel

Subsequently, **TABTA-Ibp** metallogel was prepared using the silver perchlorate salt. The storage modulus (G') was measured to be within the range of 230-450 Pa for **G8-TABTA-Ag** (**Figure 4.32**) metallogel, with a crossover point observed at 11%. Additionally, angular frequency-dependent storage modulus (G') and loss modulus (G'') parameters were examined for the metallogels to confirm their viscoelastic properties, as depicted in (**Figure 4.33**).

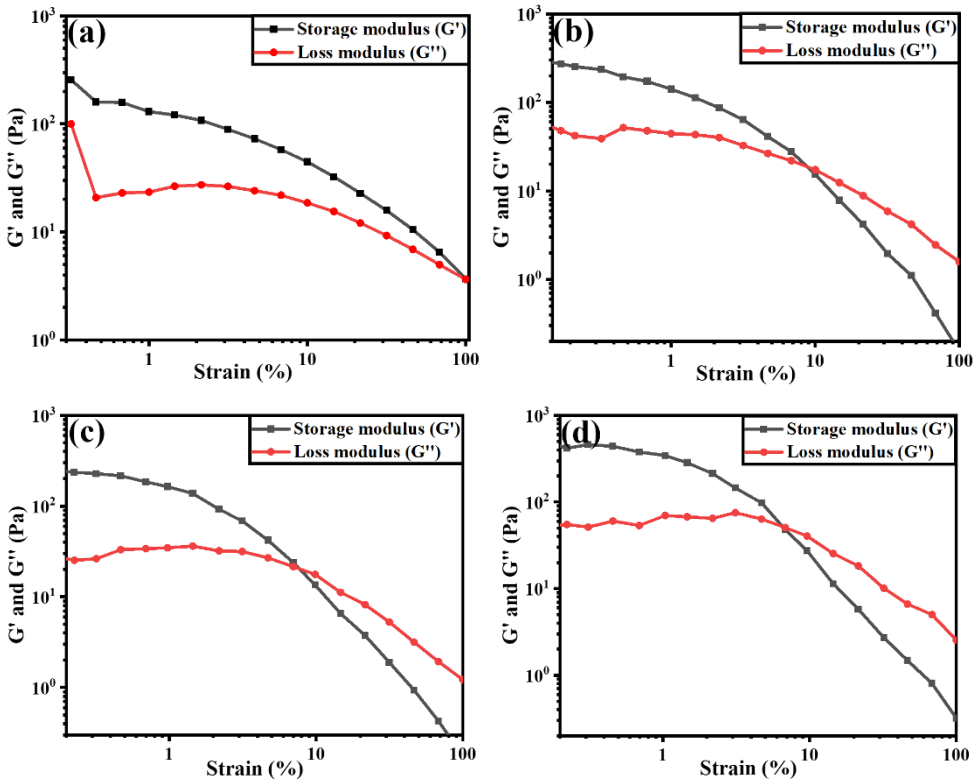

Figure 4.32: Linear viscoelastic (LVE) range of **TABTA-Ibp-Ag** metallogel for varying concentrations of Ag-perchlorate salt from 0.15 to 0.30 mmol

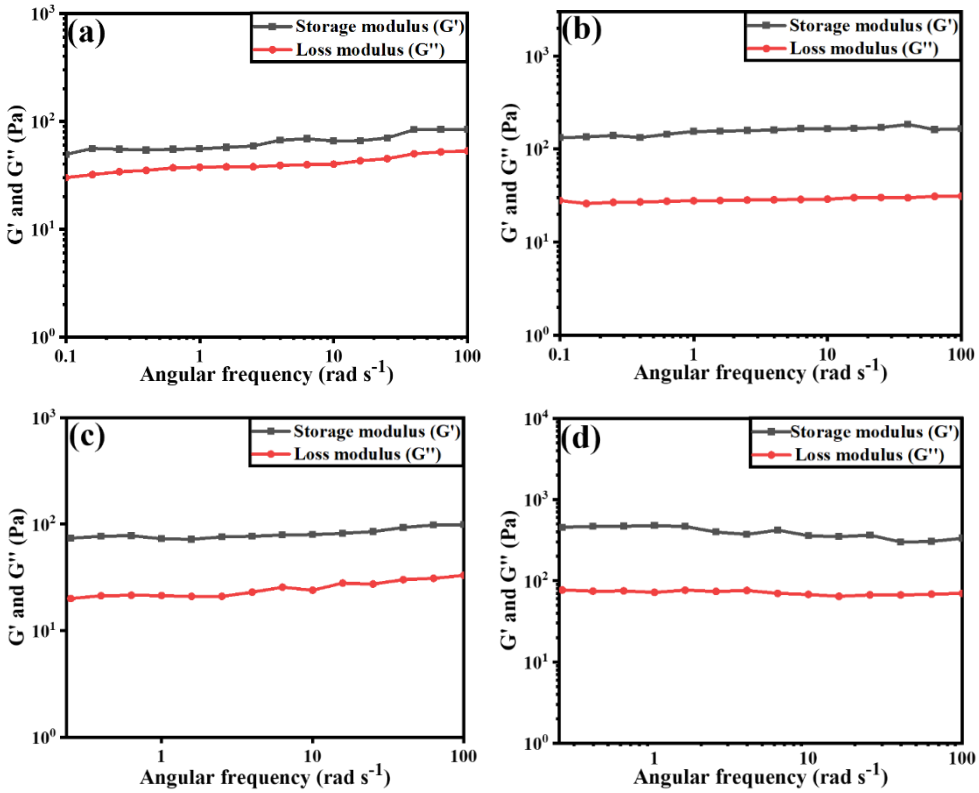

Figure 4.33: Angular frequency sweep of **TABTA-Ibp-Ag** metallogel for varying concentrations of Ag-perchlorate salt from 0.15 to 0.30 mmol

Additionally, the rheological time-oscillation strain-sweep experiment (thixotropic measurement) was performed for the **TABTA-Ibp** organogel (**Figure 4.34** (a)) and its silver metallogel, **G8-TABTA-Ag** (**Figure 4.34** (b)). The organogel and metallogel underwent cyclic strain, starting with a low strain of 0.5% shear strain where the storage modulus (G') exceeded the loss modulus (G"). Over time, the strain was incrementally increased to 100%, leading to a transformation of the metallogel into a quasi-liquid state (sol), as observed in time sweep plots where G' became less than G". Upon the removal of high strain, the metallogels reverted to their original viscoelastic behavior, with G' surpassing G" again. This reversible process was repeated multiple times for all synthesized metallogels, demonstrating their thixotropic characteristics.

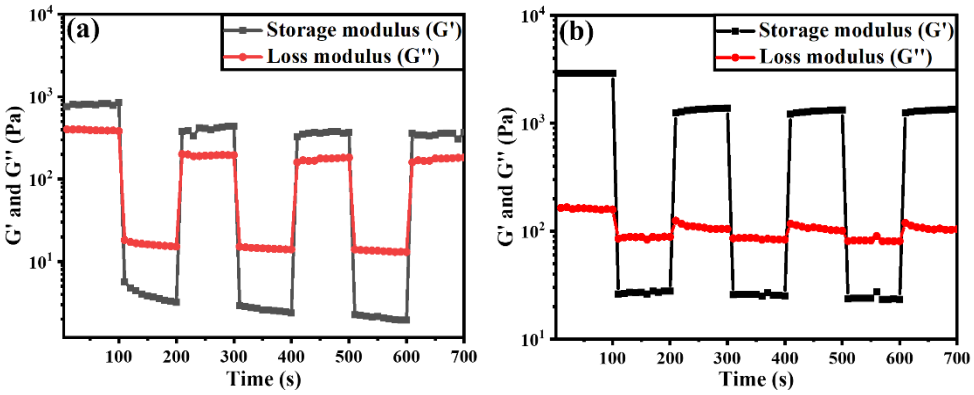

Figure 4.34: Time-oscillation strain-sweep experiment (thixotropic behavior) of (a) **TABTA-Ibp** organogel, and (b) **TABTA-Ibp-Ag** metallogel

4.7.5 PXRD Analysis

The PXRD technique investigated the interactions between the gelator components **G8** and **TABTA**. As already reported, **G8** shows peaks at 2θ= 20.08° (d = 4.42 Å) for intercolumnar stacking and 2θ = 27.30° (d = 3.26 Å) for π-π stacking. [48] Conversely, **TABTA** exhibits peaks at 2θ= 20.58° (d = 4.31 Å) for intercolumnar stacking, and π-π stacking peaks at 2θ = 22.52° (d = 3.94 Å) and 2θ = 27.36° (d =3.26 Å). However, upon analysis of the xerogel of **G8-TABTA**, an intense peak at 2θ = 27.30° (d = 3.26 Å) and a peak at 2θ = 22.58° (d = 3.93 Å) corresponding to π-π stacking were

observed (**Figure 4.35** (a)). Thus, based on the PXRD data, it can be inferred that π-π stacking likely plays a significant role in the interaction between **G8** and **TABTA**, leading to gel formation, which aligns well with the FT-IR data.

Subsequently, the **sodium salt of ibuprofen** shows peaks at 2θ = 17.25° (d = 5.13 Å), 2θ = 18.82° (d =4.71 Å), 2θ = 22.35° (d = 3.97 Å), 2θ = 29.85° (d =2.99 Å), 2θ = 32.45° (d = 2.76 Å), and 2θ = 39.42° (d =2.28 Å). However, when analyzing the xerogel of **TABTA-Ibp**, there's a noticeable change in peak intensity within the range of 2θ = 17.25° to 22.35°, corresponding to intercolumnar stacking and π-π stacking. Meanwhile, peaks at 2θ = 29.85°, 32.45°, and 39.42° become slightly more intense, corresponding to hydrogen bonding interactions (**Figure 4.35** (b)). Thus, based on the PXRD data, it can be inferred that hydrogen bonding interactions between **TABTA** and **sodium salt of ibuprofen** likely lead to gel formation, consistent with the FT-IR data.

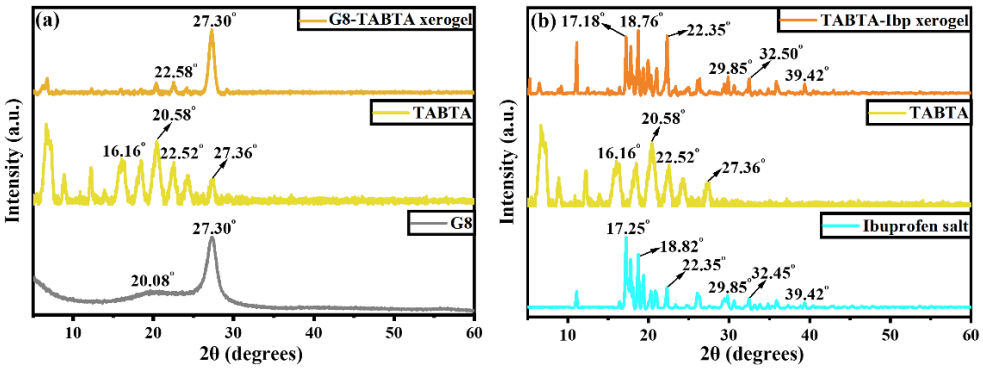

Figure 4.35: PXRD spectra of (a) **G8**, **TABTA,** and **G8-TABTA** xerogel. (b) **Ibuprofen salt**, **TABTA,** and **TABTA-Ibp** xerogel

The PXRD analyses for **G8-TABTA-Ag** xerogel, **G8-TABTA-Zn** xerogel, and **TABTA-Ibp-Ag** xerogel were conducted where for **G8-TABTA-Ag** xerogel very intense peaks were observed at 2θ = 38.31°, 44.48°, 64.54°, and 77.51° corresponding to 111, 200, 220, and 311 crystallographic planes of the face-centered cubic (fcc) silver crystals.[54] Similar peaks like xerogel of **G8-TABTA** organogel were also observed at 2θ = 27.59°, and 22.58° (**Figure 4.36** (a)). Similarly, for **G8-TABTA-Zn** xerogel, the major peaks

were observed at 2θ = 18.75°, 23.35°, and 26.62° (**Figure 4.36** (b)). Next, for **TABTA-Ibp-Ag** xerogel again very intense peaks were observed at 2θ = 38.15°, 44.23°, 64.61°, and 77.56° corresponding to 111, 200, 220, and 311 crystallographic planes of the face-centered cubic (fcc) silver crystals.[54] Similar peaks like xerogel of **TABTA-Ibp** organogel were also observed at 2θ = 21.80°, 26.48°, and 29.10° (**Figure 4.36** (c)). Thus, it can be concluded that silver nanoparticles are formed within the gel matrix for both the silver metallogels.

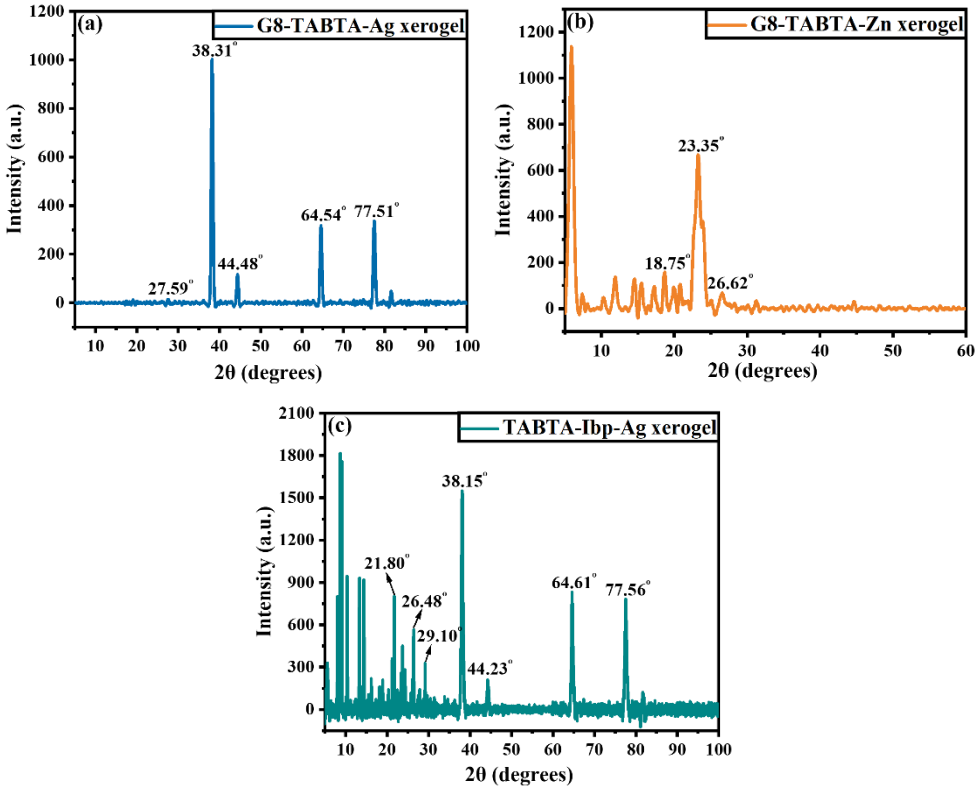

Figure 4.36: PXRD spectrum of (a) **G8-TABTA-Ag** xerogel, (b) **G8-TABTA-Zn** xerogel, and (c) **TABTA-Ibp-Ag** xerogel

4.7.6 Thermogravimetric Analysis

Thermogravimetric analysis was conducted to examine the thermal stability of the gelator components **G8** and **TABTA**, as well as the xerogels of organogel and metallogels of **G8-TABTA** and **TABTA-Ibp**, within the temperature range from 30 to 800ºC.

4.7.6.1 The gelator components G8 and TABTA

The TGA analysis showed the thermal stability of the gelator components **G8** and **TABTA** with minimal weight loss of 7% and 4% up to 240ºC and 316ºC, respectively. This weight loss might be due to the removal of the entrapped solvent molecules on the surface of the compound. Moreover, for **G8** between 240-340ºC, the observed weight loss was about 21%, possibly due to the breakage of C-N bonds of the secondary amine between cyanuric and tetrazole rings (**Figure 4.37** (a)). In contrast, in the case of **TABTA**, 44% of weight loss was observed between 316-540ºC, indicating the stability of the amide bond in **TABTA** up to 540ºC (**Figure 4.37** (b)).

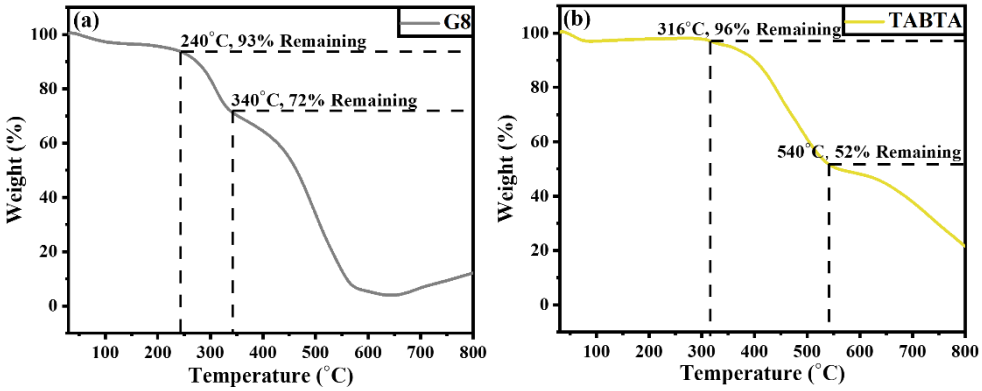

Figure 4.37: TGA analysis of the gelator components (a) **G8**, and (b) **TABTA**

4.7.6.2 G8-TABTA organogel and its silver and zinc metallogel

For **G8-TABTA** organogel and its silver and zinc metallogel, the observed minimal weight loss was about 11-12% up to the 170-260ºC temperature range, which might be due to the disruption of the non-covalent interactions that facilitate gel formation between the gelator components and the metal ion for metallogels. However, the weight loss was more pronounced at the low volatility range for **G8-TABTA** organogel than it was for its metallogels, indicating a stronger gel network formation in the metallogel. Additionally, for **G8-TABTA-Ag** and **G8-TABTA-Zn** xerogel, it was observed that above 800ºC, approximately 36% and 15% of residue remains undecomposed, corresponding to the silver and zinc content in the xerogel, respectively (**Figure 4.38**).

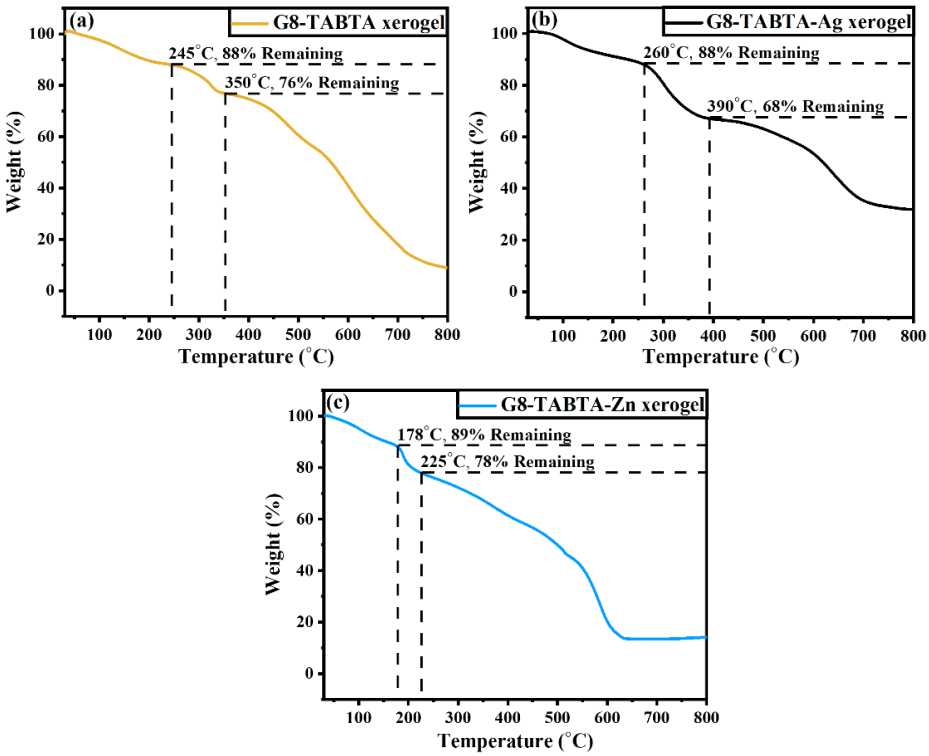

Figure 4.38: TGA analysis of (a) **G8-TABTA** xerogel, (b) **G8-TABTA-Ag** xerogel, and (c) **G8-TABTA-Zn** xerogel

4.7.6.3 TABTA- Ibp organogel and its silver metallogel

Next, for **TABTA- Ibp** organogel and its silver metallogel, the observed minimal weight loss was about 25-30% up to the 70-300ºC temperature range, which might be due to the disruption of the non-covalent interactions that facilitate gel formation between the gelator components and the metal ion for metallogels. However, the weight loss was more pronounced for the **G8-TABTA-Ag** metallogel, indicating a weaker metallogel network formation (**Figure 4.39**).

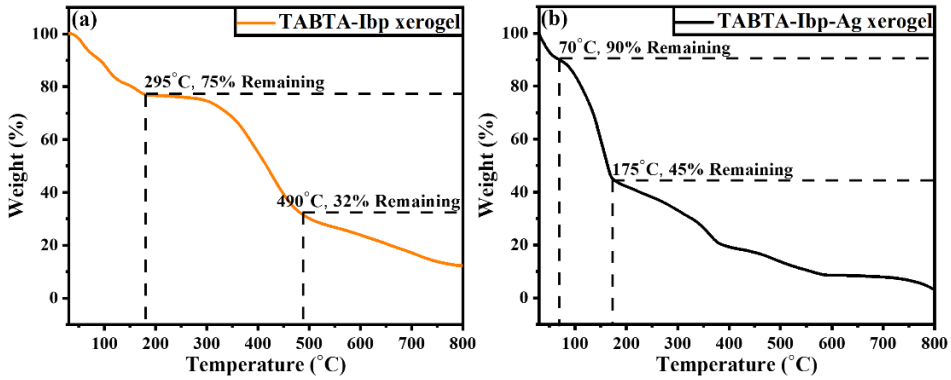

Figure 4.39: TGA analysis of (a) **TABTA-Ibp** xerogel, and (b) **TABTA-Ibp-Ag** xerogel

4.7.7 BET Analysis

Brunauer−Emmett−Teller (BET) analysis was conducted to examine the surface area and porosity, and the Barrett-Joyner-Halenda (BJH) method was used to plot the pore size distribution of the gelator components **G8** and **TABTA**, as well as the xerogels of organogel and metallogels of **G8-TABTA** and **TABTA-Ibp**, from N_2 adsorption-desorption isotherm at 77K and 1 bar pressure.

4.7.7.1 The gelator components G8 and TABTA

The surface area for the gelator components **G8** and **TABTA** was found to be 21.936 m^2/g and 18.113 m^2/g, respectively (**Figure 4.40**).

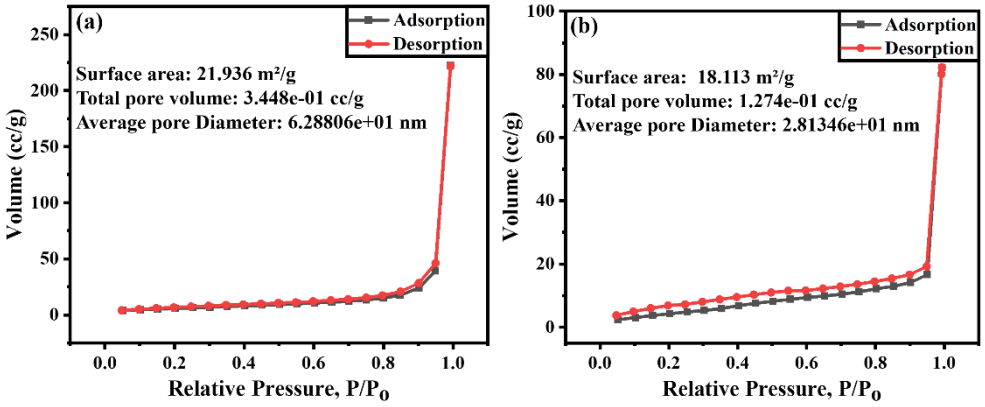

Figure 4.40: N_2 adsorption and desorption isotherm for the gelator components (a) **G8**, and (b) **TABTA**

Further, the pore size of the xerogel was found to be between 2-50 nm confirming the mesoporous nature of the gelator components **G8** and **TABTA** (**Figure 4.41**).

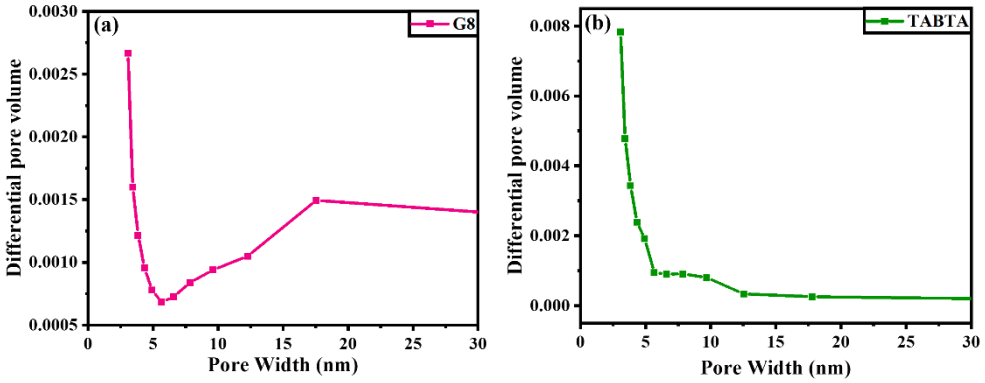

Figure 4.41: BJH pore size distribution for the gelator components (a) **G8**, and (b) **TABTA**

4.7.7.2 G8-TABTA organogel and its silver and zinc metallogel

For **G8-TABTA** organogel and its silver and zinc metallogel, the surface area was observed to be 3.033 m^2/g, 1.923 m^2/g, and 5.518 m^2/g respectively (**Figure 4.42**) indicating the stronger gel network formation between the gelator components. Further, the other parameters obtained from the N_2 adsorption-desorption isotherm are listed below (**Table 4.15**).

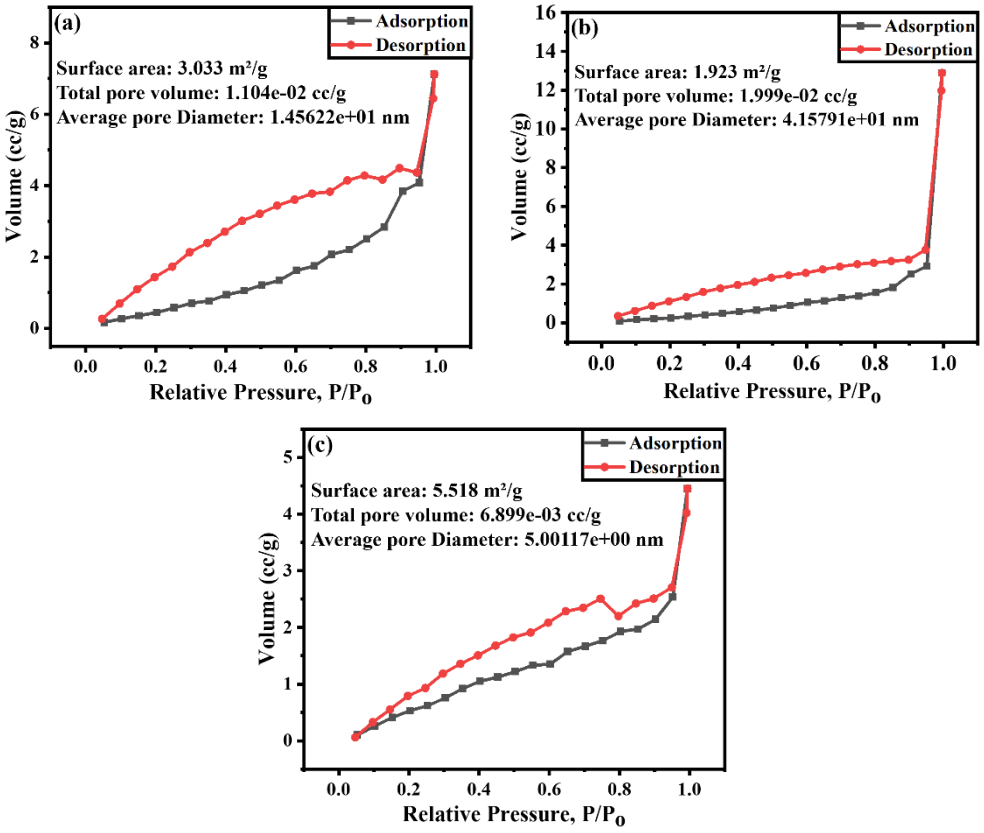

Figure 4.42: N_2 adsorption and desorption isotherm for (a) **G8-TABTA** xerogel, (b) **G8-TABTA-Ag** xerogel, and (c) **G8-TABTA-Zn** xerogel

Table 4.15: Characteristic parameters of xerogel of **G8-TABTA** organogel and its silver and zinc metallogel obtained from N_2 adsorption-desorption isotherm

	BET Surface area	**Total pore volume**	**Average pore diameter**
G8-TABTA xerogel	3.033 m^2/g	1.104e-02 cc/g	1.45622e+01 nm
G8-TABTA-Ag xerogel	1.923 m^2/g	1.999e-02 cc/g	4.15791e+01 nm
G8-TABTA-Zn xerogel	5.518 m^2/g	6.899e-02 cc/g	5.00117e+00 nm

Moreover, the pore size was found to be between 2-10 nm for the xerogels of **G8-TABTA** organogel and its metallogels calculated using the Barrett-Joyner-Halenda (BJH) method (**Figure 4.43**).

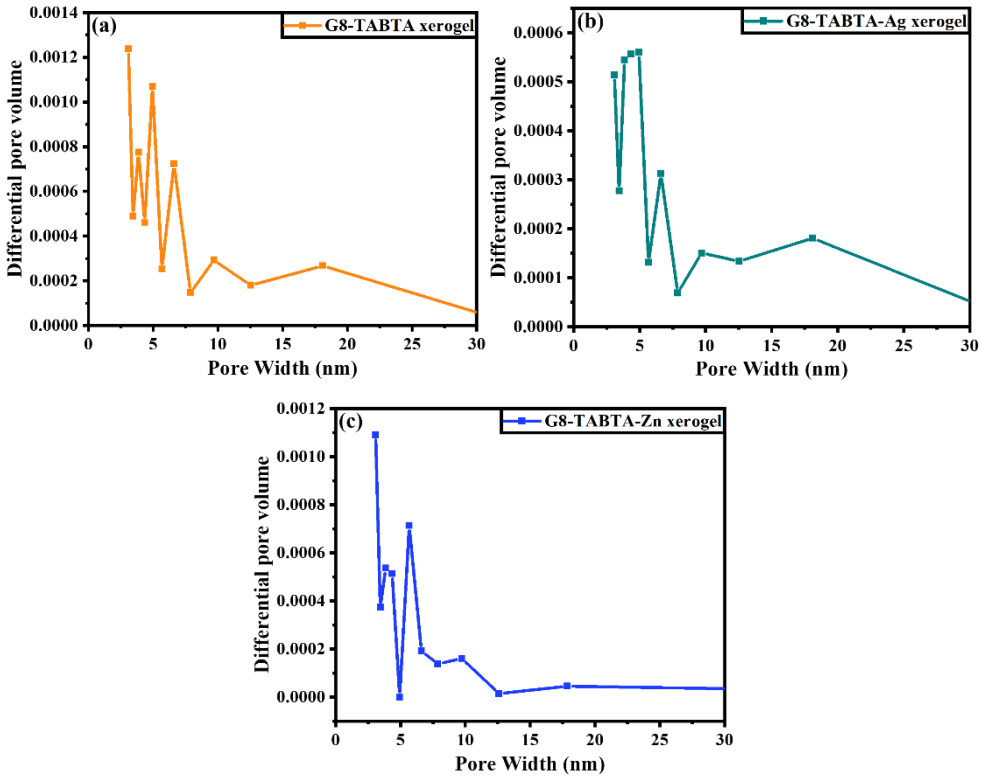

Figure 4.43: BJH pore size distribution for (a) **G8-TABTA** xerogel, (b) **G8-TABTA-Ag** xerogel, and (c) **G8-TABTA-Zn** xerogel

4.7.7.3 TABTA- Ibp organogel and its silver metallogel

Next, for **TABTA- Ibp** organogel and its silver metallogel, the surface area was observed to be 12.014 m^2/g, and 8.666 m^2/g respectively (**Figure 4.44**) indicating the mesoporous gel network formed between the gelator components. Further, the other parameters obtained from N_2 adsorption-desorption isotherm are listed below (**Table 4.16**).

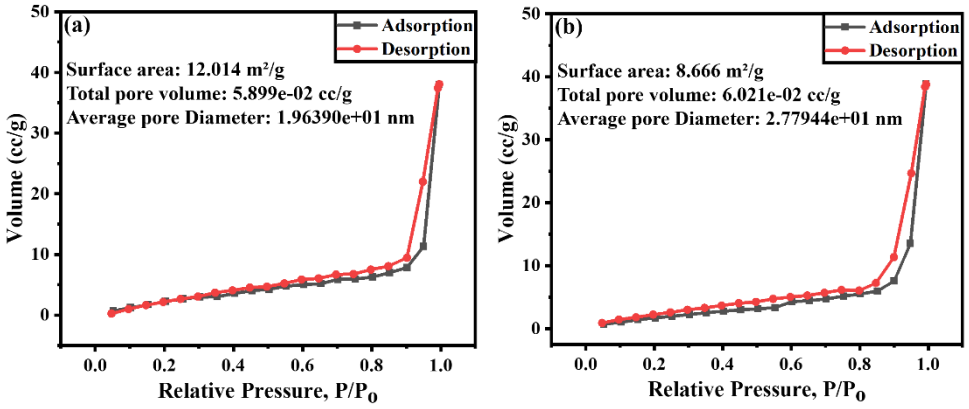

Figure 4.44: N_2 adsorption and desorption isotherm for (a) **TABTA-Ibp** xerogel, and (b) **TABTA-Ibp-Ag** xerogel

Table 4.16: Characteristic parameters of xerogel of **TABTA-Ibp** organogel and its silver metallogel obtained from N_2 adsorption-desorption isotherm

	BET Surface area	**Total pore volume**	**Average pore diameter**
TABTA-Ibp xerogel	12.014 m^2/g	5.899e-02 cc/g	1.96390e+01 nm
TABTA-Ibp-Ag xerogel	8.666 m^2/g	6.021e-02 cc/g	2.77944e+01 nm

Moreover, the pore size was found to be between 2-10 nm for the xerogels of **TABTA-Ibp** organogel and its silver metallogel calculated using the Barrett-Joyner-Halenda (BJH) method (**Figure 4.45**).

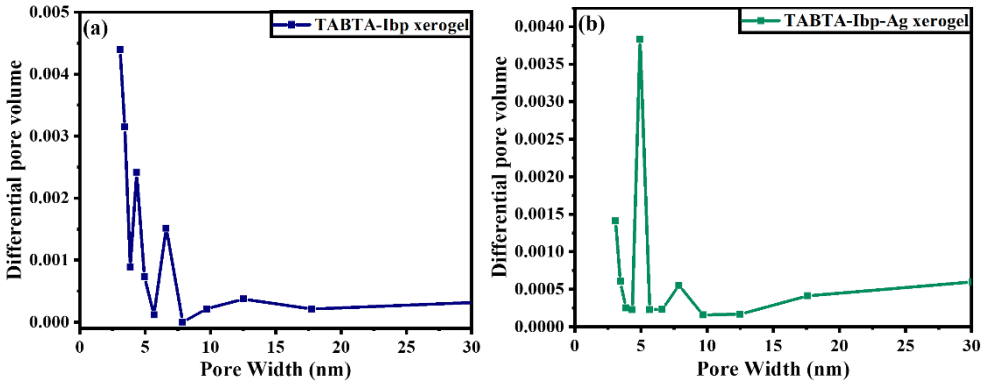

Figure 4.45: BJH pore size distribution for (a) **TABTA-Ibp** xerogel, and (b) **TABTA-Ibp-Ag** xerogel

4.7.8 FESEM Analysis

FESEM analysis was conducted to evaluate the morphology of the xerogels of the synthesized gels. The gelator component **TABTA** shows microrod-type morphology (**Figure 4.46** (a)). Upon transformation to hybrid organogel **G8-TABTA**, its xerogel shows flower-type morphology (**Figure 4.46** (b)). Subsequent analysis of metallogels derived from the **G8-TABTA** hybrid matrix revealed notable morphological alterations: **G8-TABTA-Ag** exhibited needle-like structures, while **G8-TABTA-Zn** displayed long fiber-like formations (**Figure 4.46** (c and d)).

Furthermore, the xerogel of **TABTA-Ibp** showed a granular morphology, which transformed into flakes upon formation of its silver metallogel, **TABTA-Ibp-Ag** (**Figure 4.47** (a and b)), respectively.

Therefore, these FESEM images provide visual evidence of interactions between the gelator components and metal ions in the metallogels, resulting in morphological transformations.

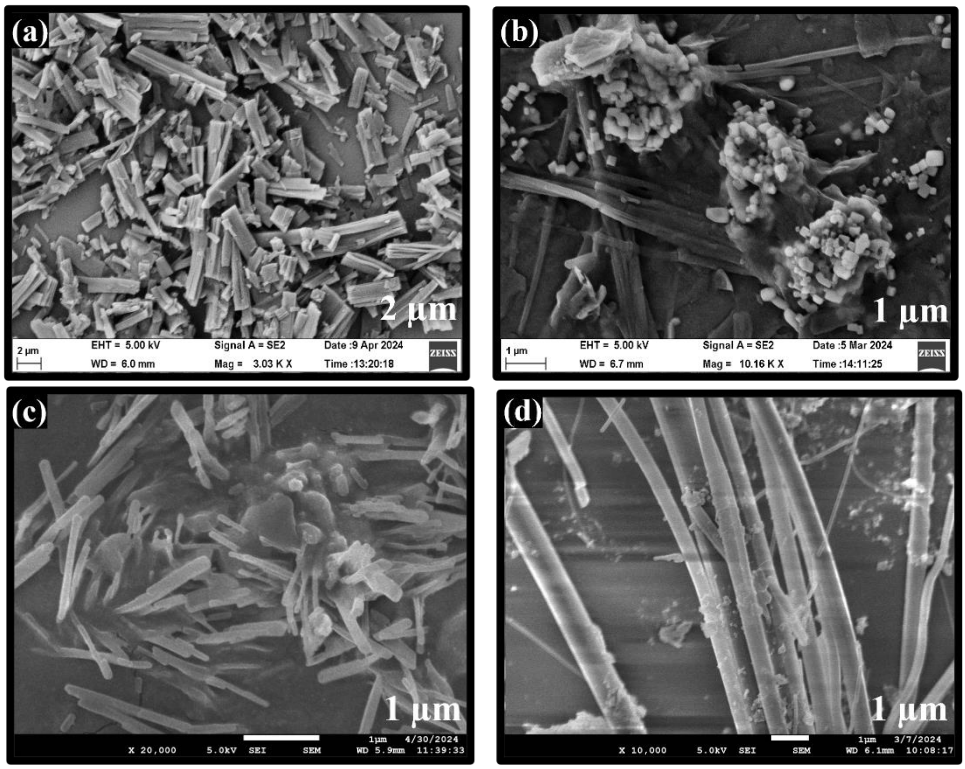

Figure 4.46: FESEM images of (a) gelator component **TABTA** (powder), (b) **G8-TABTA** xerogel, (c) **G8-TABTA-Ag** xerogel, and (d) **G8-TABTA-Zn** xerogel

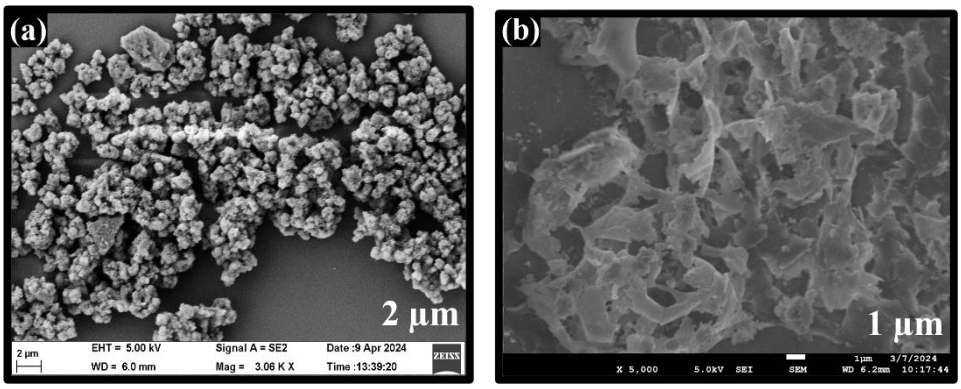

Figure 4.47: FESEM images of (a) **TABTA-Ibp** xerogel, and (b) **TABTA-Ibp-Ag** xerogel

4.8 Analysis of silver nanoparticle formation for G8-TABTA-Ag and TABTA-Ibp-Ag metallogel

Furthermore, for both the silver metallogels of **G8-TABTA** and **TABTA-Ibp** after 24 hours, a notable color change was observed (**Figure 4.48**), suggesting the formation of silver nanoparticles within the gel matrix.

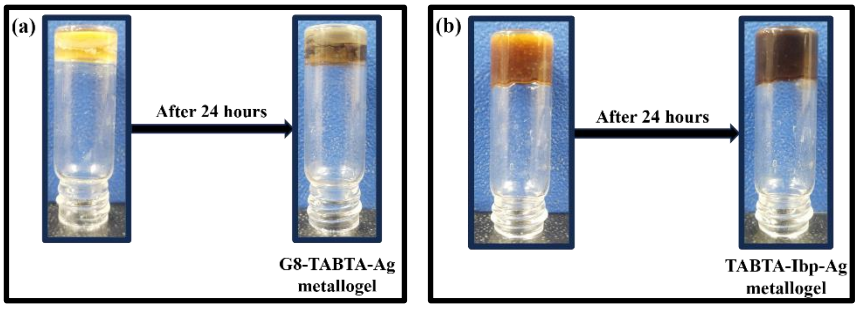

Figure 4.48: Formation of silver nanoparticles within the gel matrix after 24 hours for (a) **G8-TABTA-Ag** metallogel, and (b) **TABTA-Ibp-Ag** metallogel

The formation of silver nanoparticles was analyzed using UV-visible spectroscopy. A broad peak at 475 and 450 nm was observed for **G8-TABTA-Ag** metallogel and its xerogel, respectively (**Figure 4.49** (a)). Similarly, for **TABTA-Ibp-Ag** metallogel and its xerogel, a broad peak at 460 and 450 nm respectively was observed (**Figure 4.49** (b)). According to literature reports, AgNPs generally show an absorption peak in the range of 410−480 nm due to their strong surface plasmon resonance (SPR) which

arises from the collective oscillations of free electrons on the nanoparticle surface. Depending upon the particle size, the oscillation varies, which in turn governs the particular wavelength range in the visible spectrum.[55] Moreover, the PXRD analysis also confirms the formation of silver nanoparticles (already discussed in Section **4.7.5**).

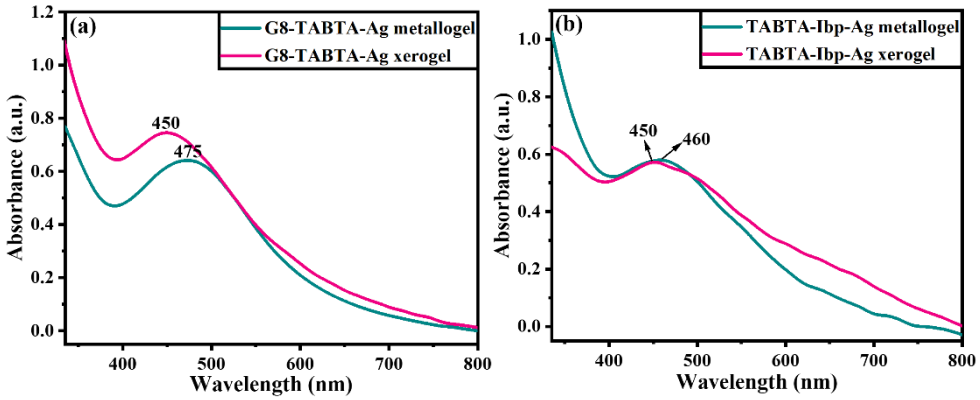

Figure 4.49: UV-vis spectra depicting the synthesis of silver nanoparticles for (a) **G8-TABTA-Ag** metallogel, and (b) **TABTA-Ibp-Ag** metallogel

The FESEM analysis was conducted for the formation of silver nanoparticles after 24 hours of the formation of the **G8-TABTA** and **TABTA-Ibp** metallogels. Both the metallogels displayed nanoscale spherical morphologies (**Figure 4.50** (a and b)), respectively.[56]

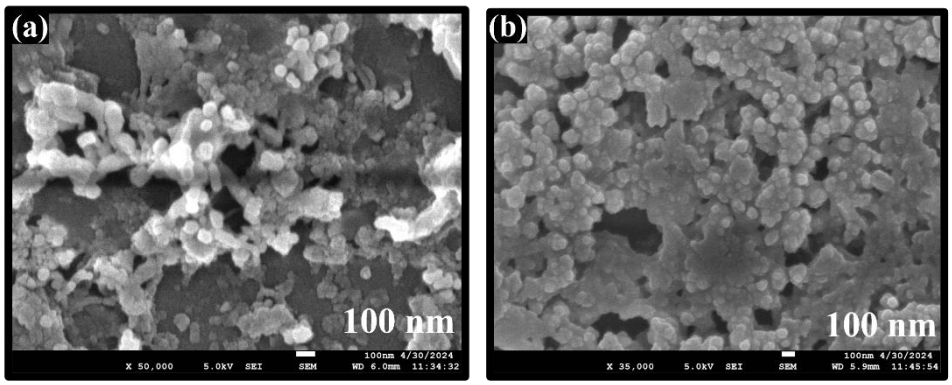

Figure 4.50: FESEM images of (a) **G8-TABTA-Ag** metallogel, and (b) **TABTA-Ibp-Ag** metallogel, taken after 24 hours of the metallogel formation

Further, EDS and elemental mapping analysis were done for both the metallogels, confirming the presence of silver in both the nanocomposites (**Figure 4.51)**.

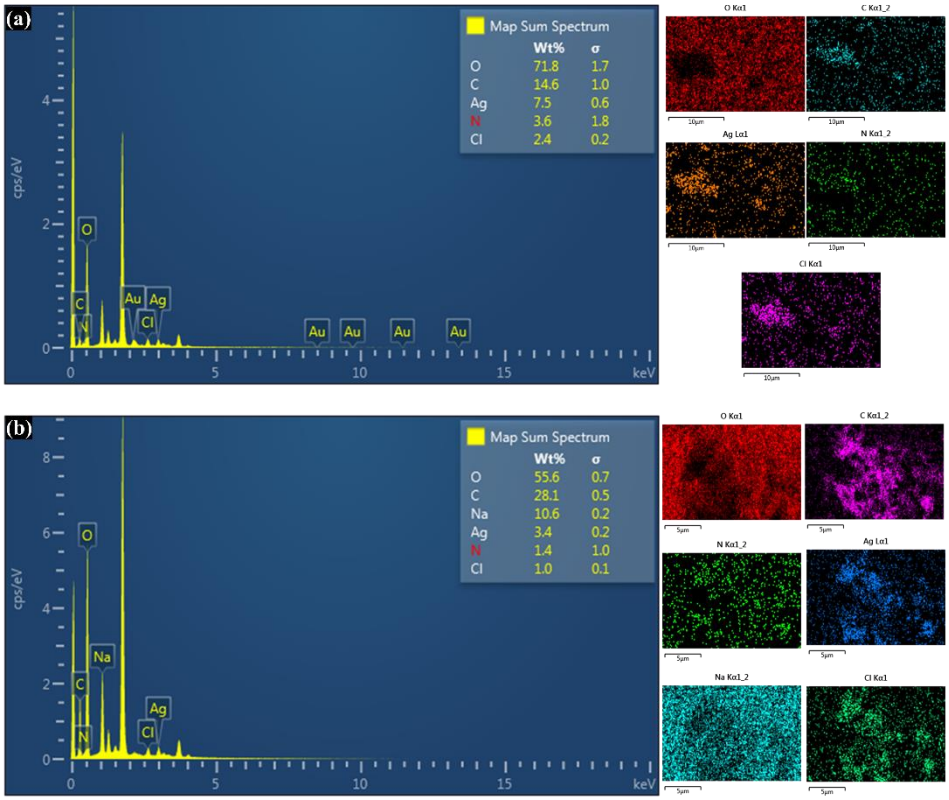

Figure 4.51: EDS spectrum and elemental mapping analysis of (a) **G8-TABTA-Ag** metallogel, and (b) **TABTA-Ibp-Ag** metallogel

Further, the XPS analysis was carried out for both the silver metallogels to confirm the presence of all the elements and silver nanoparticles in the metallogel matrices. The deconvoluted XPS spectra for Ag 3d show two peaks at 374.6 and 368.2 eV for the **G8-TABTA-Ag** matrix, whereas in the case of the **TABTA-Ibp-Ag** matrix peaks at 374.8 and 368.7 eV were observed corresponding to the $3d_{3/2}$ and $3d_{5/2}$ orbits of Ag(0), respectively, thus, confirming the formation of silver nanoparticles (**Figure 4.52 and 4.53**), respectively.[36,57]

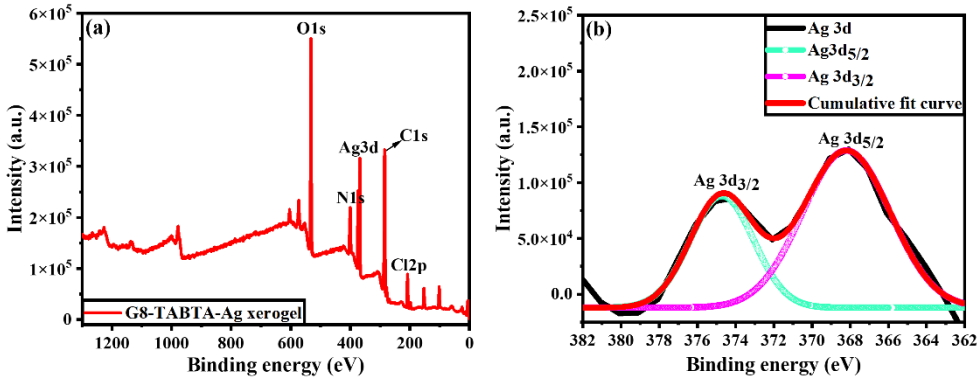

Figure 4.52: (a) XPS spectra, and (b) Deconvoluted XPS spectra of Ag 3d, of **G8-TABTA-Ag** xerogel

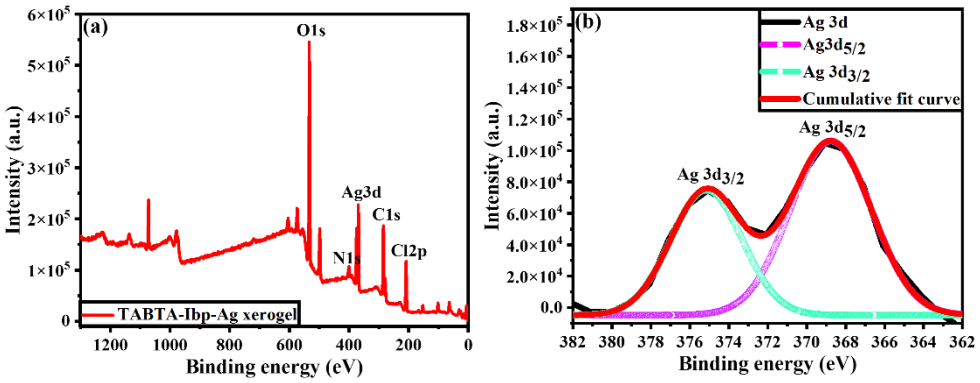

Figure 4.53: (a) XPS spectra, and (b) Deconvoluted XPS spectra of Ag 3d, of **TABTA-Ibp-Ag** xerogel

4.9 Self-healing and injectibility properties of G8-TABTA and TABTA-Ibp gels

The self-healing capability was also examined for the prepared organogels and metallogels of **G8-TABTA** and **TABTA-Ibp**. It was assessed by finely fragmenting the gels, which demonstrated the ability to restore itself to its initial state when the fragmented pieces were brought into proximity (**Figure 4.54**) and (**Figure 4.55**).

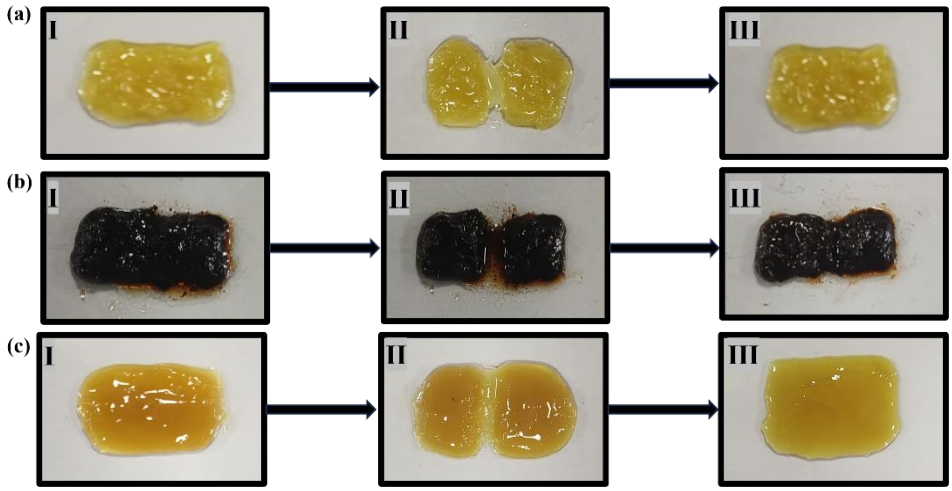

Figure 4.54: Images showing the self-healing property of (a) **G8-TABTA** organogel, (b) **G8-TABTA-Ag** metallogel, and (c) **G8-TABTA-Zn** metallogel

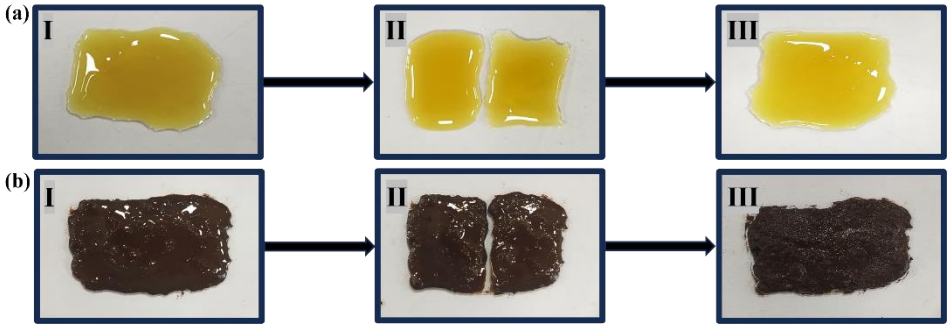

Figure 4.55: Images showing the self-healing property of (a) **TABTA-Ibp** organogel, and (b) **TABTA-Ibp-Ag** metallogel

Moreover, for self-drug delivery application purposes, the injectable behavior of **TABTA-Ibp** organogel and **TABTA-Ibp-Ag** metallogel was examined (**Figure 4.56** (a)) and (**Figure 4.56** (b)) respectively. It was noticed that both gels could be injected through a narrow syringe after gelation. When subjected to external mechanical force, these interactions were disrupted, causing the gel to transition into a viscous liquid, which regains its original structure upon removal of the external force through supramolecular interactions.

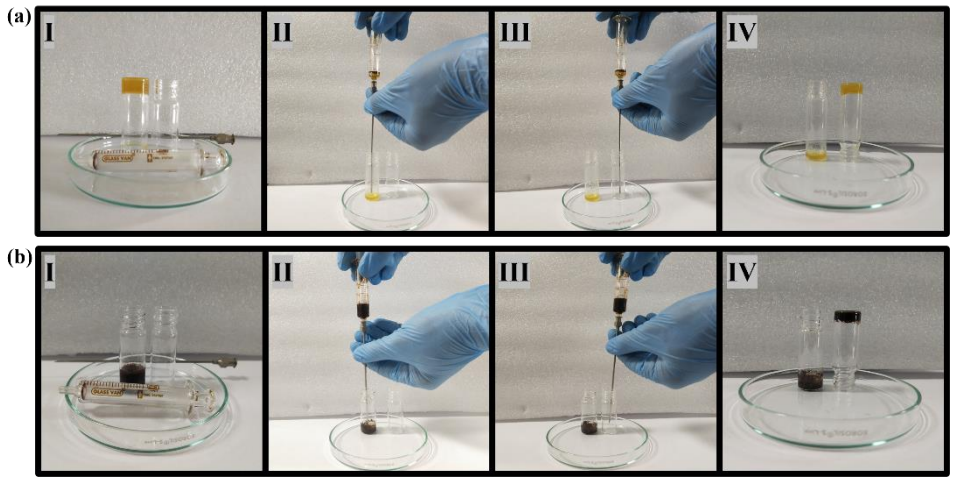

Figure 4.56: Images showing the injectibility of (a) **TABTA-Ibp** organogel, and (b) **TABTA-Ibp-Ag** metallogel

4.10 UV-Vis Spectra for G8-TABTA gel matrix

The UV-Vis spectra of **G8**, **TABTA,** and **G8-TABTA** organogel (**Figure 4.57**) were taken in the solution state. As already reported, **G8** shows one absorbance peak at 335 nm in the solid-state UV-Vis spectrum, whereas, in the solution state, only a broad shoulder was observed in this range at around 320 nm and a sharp peak at 268 nm.[48] Similarly, when the UV-Vis analysis was carried out for **TABTA** and **G8-TABTA** organogel in the solution state, a broad UV-Vis peak was observed at around 315 nm and a sharp peak at 268 nm. These peaks might be due to the intramolecular π-π* and n-π* transitions between the aromatic moieties, respectively.[58]

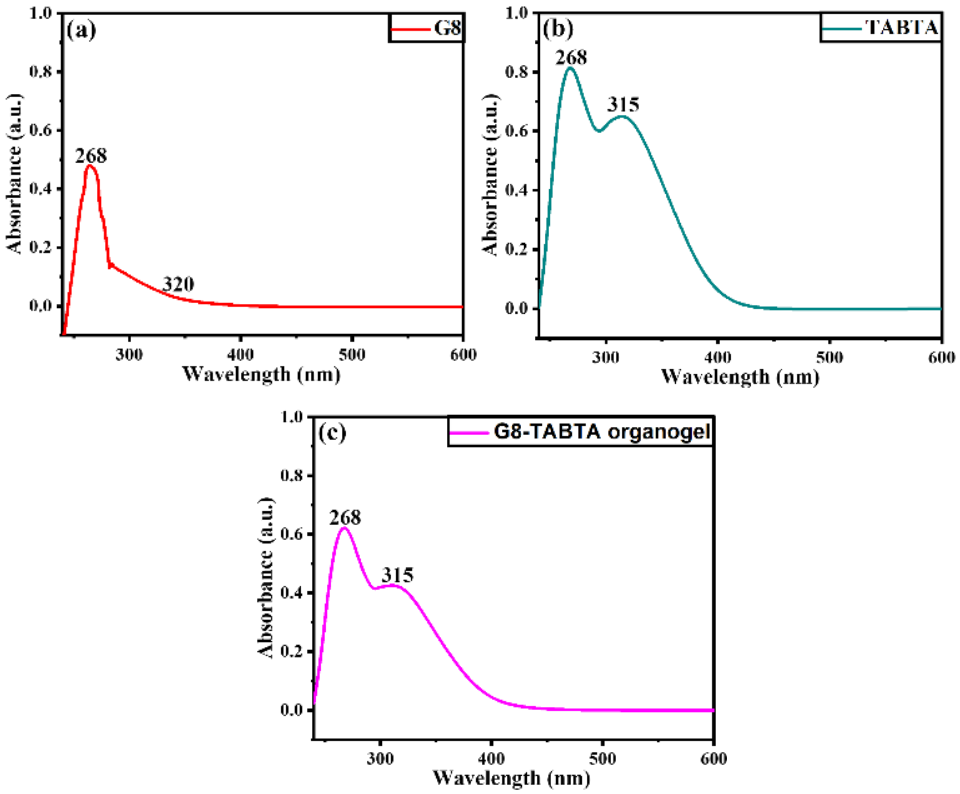

Figure 4.57: UV-visible spectrum of (a) **G8**, (b) **TABTA**, and (c) **G8-TABTA** organogel

4.11 Fluorescence Spectra for G8-TABTA gel matrix

The emission spectra for the gelation components **G8**, **TABTA,** and **G8-TABTA** (**Figure 4.58** (**a**)) were recorded in DMSO by exciting at a wavelength of 350 nm. From the emission spectra, a very high-intensity peak for **G8** (emission wavelength 430 nm) was observed compared to **TABTA** and the organogel **G8-TABTA** (emission wavelength 422 nm and 425 nm respectively). These results suggest that the formed organogel **G8-TABTA** undergoes aggregation-caused quenching (ACQ) and the introduction of **TABTA** to the organogel **G8-TABTA** strongly dominates the decrease in fluorescence intensity. The ACQ phenomenon observed may result from the specific interactions between the gelator components **G8** and **TABTA**.

Further, to study the effect of concentration on the fluorescence behavior of **G8**, **TABTA**, and **G8-TABTA** organogel (**Figure 4.58**), a 1 mM stock solution of **G8**, **TABTA**, and **G8-TABTA** organogel was prepared in

DMSO. As already reported for **G8**, it shows aggregation-induced enhanced emission (AIEE),[48] i.e., the fluorescence intensity increases on increasing the concentration of **G8**, while in contrast, **TABTA** shows ACQ as with increasing concentration, fluorescence intensity decreases. Like **TABTA**, the fluorescence intensity of organogel **G8-TABTA** also decreases by increasing its concentration, demonstrating the ACQ phenomenon.

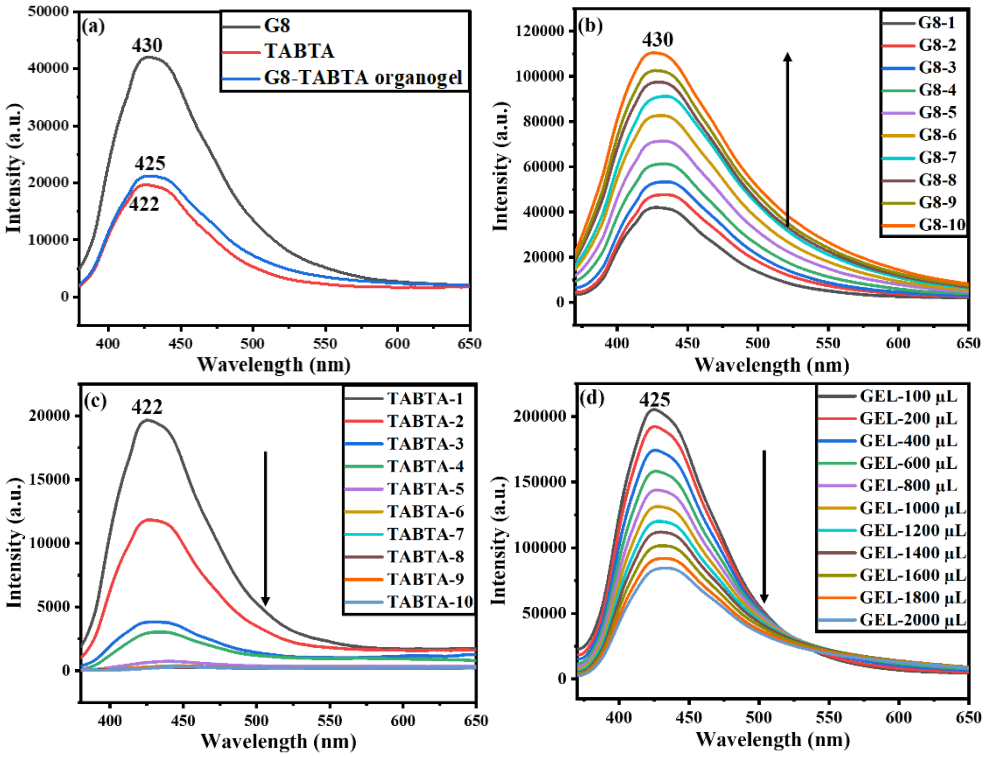

Figure 4.58:(a) Fluorescence spectra of **G8**, **TABTA,** and **G8-TABTA** in DMSO (b) AIE phenomenon of **G8** (1 mM in 20 mL DMSO) from 50-2000 µL of **G8** (c) ACQ phenomenon of **TABTA** (1 mM in 20 mL DMSO) from 50-2000 µL of **TABTA** (d) ACQ phenomenon of **G8-TABTA** organogel (1 mM in 20 mL DMSO) from 50-2000 µL of **G8-TABTA** organogel

4.12 Drug Release of Ibuprofen drug from TABTA-Ibp organogel and TABTA-Ibp-Ag metallogel

It is well-established that a gel creates a three-dimensional structure through cross-linking. It expands when immersed in a solution and can serve as an effective vehicle for delivering drugs.[59] The low-molecular-weight gel has the potential to provide either gradual or rapid release of drugs due to a pH-

induced transition from gel to sol state.[60] Accordingly, UV-visible spectroscopy was employed to examine the release of ibuprofen from **TABTA-Ibp** organogel. **TABTA** shows two peaks at 315 nm and 268 nm for intramolecular π-π* and n-π* transitions respectively, while **Ibuprofen salt** shows a peak at 235 nm due to π-π* transition.[61] Moreover, when examining **TABTA-Ibp** organogel, a slight shift was observed in the peak positions to 230, 280, and 320 nm (**Figure 4.59**).

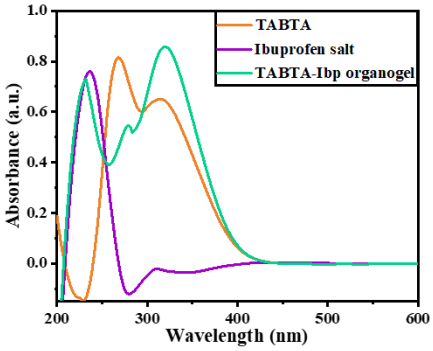

Figure 4.59: UV-visible spectra for **TABTA**, **Ibuprofen salt**, and **TABTA-Ibp** organogel

However, the addition of PBS buffer leads to the collapsing of the gel[62] and slow release of Ibuprofen drug from the gel matrix, as evidenced by the segregation of the solution layer and the formation of a yellow solid precipitate (**Figure 4.60**).

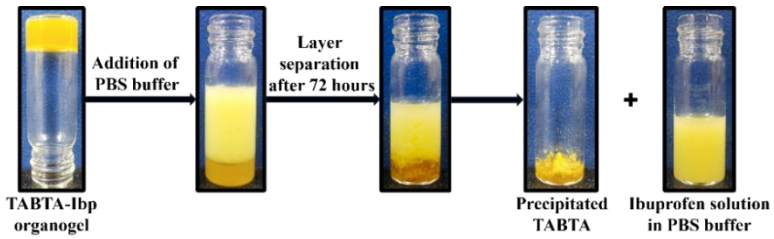

Figure 4.60: Images showing self-drug delivery of the Ibuprofen drug after the addition of PBS buffer solution to the **TABTA-Ibp** gel matrix

The precipitate was filtered and characterized by mass spectrometry and NMR spectroscopy indicating the presence of **TABTA** and the release of the Ibuprofen drug from the gel matrix. Mass data of the residue gives the most significant peak at 481.2019 m/z corresponding to gelator **TABTA** itself (**Figure 4.61**). ESI-MS (m/z) $C_{27}H_{24}N_6O_3$: Calculated for $[C_{27}H_{24}N_6O_3+H]^+$: 481.1983; Found: 481.2019. NMR data of the residue also matched well with the gelator **TABTA** confirming the release of the

Ibuprofen drug from the gel matrix. ^{1}H NMR (500MHz, 298K, DMSO-d_6) δ, ppm: 10.03 (s, 1H, H_a), 8.45 (s, 1H, CH_b), 7.30 (d, 2H, CH_c), 6.45 (d, 2H, CH_d), 4.86 (s, 2H, NH_e) (**Figure 4.62**). ^{13}C NMR (125MHz, 298K, DMSO-d_6) δ, ppm: 163.83, 145.41, 135.74, 128.97, 127.94, 122.13, 113.74 (**Figure 4.63**).

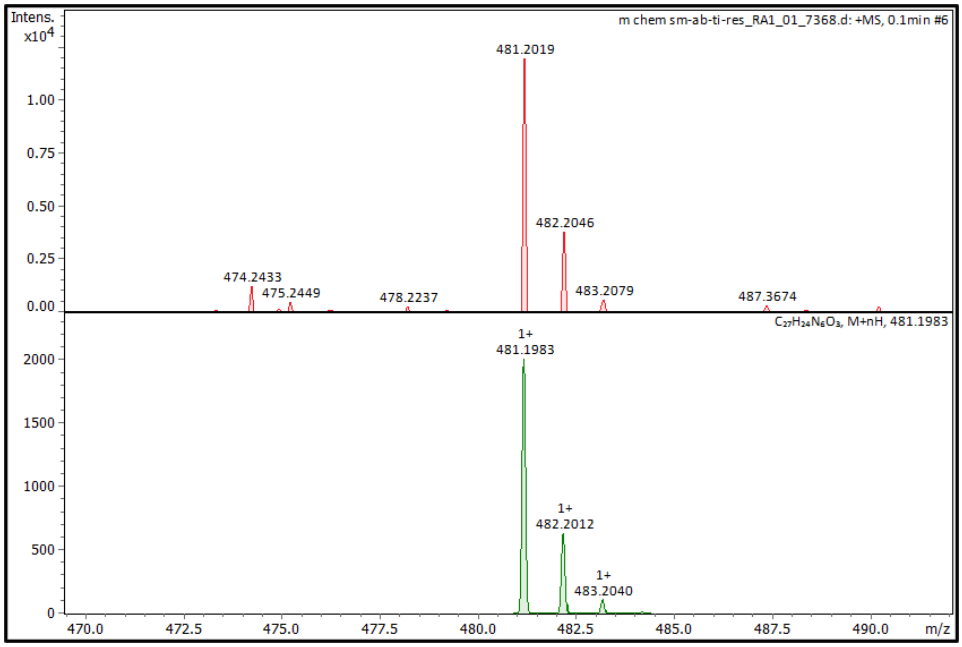

Figure 4.61: Mass spectrum of solid precipitate after drug release

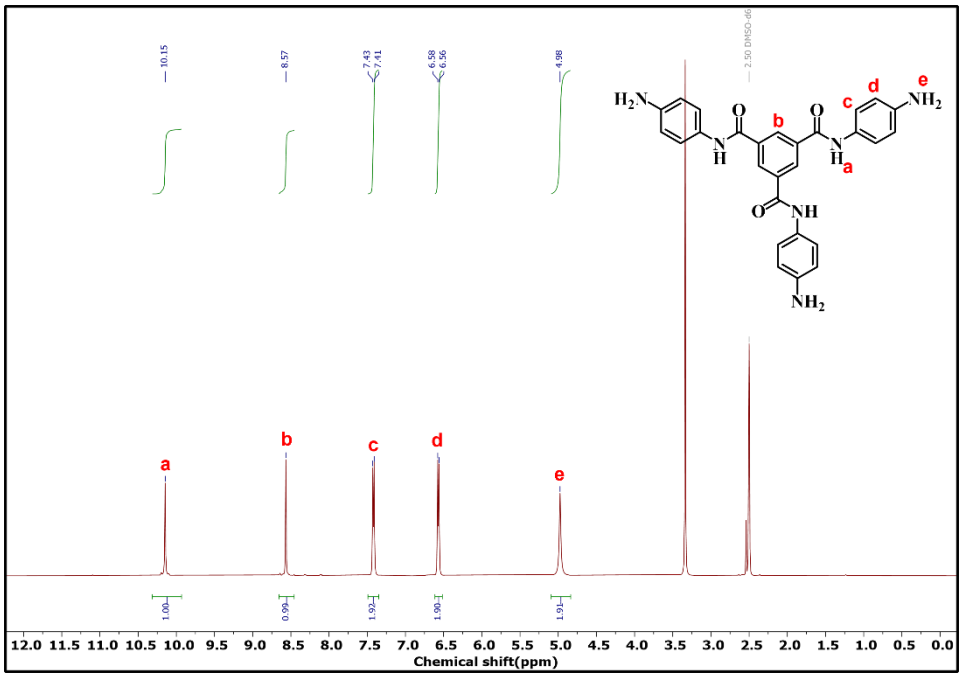

Figure 4.62: ^{1}H NMR of solid precipitate after drug release

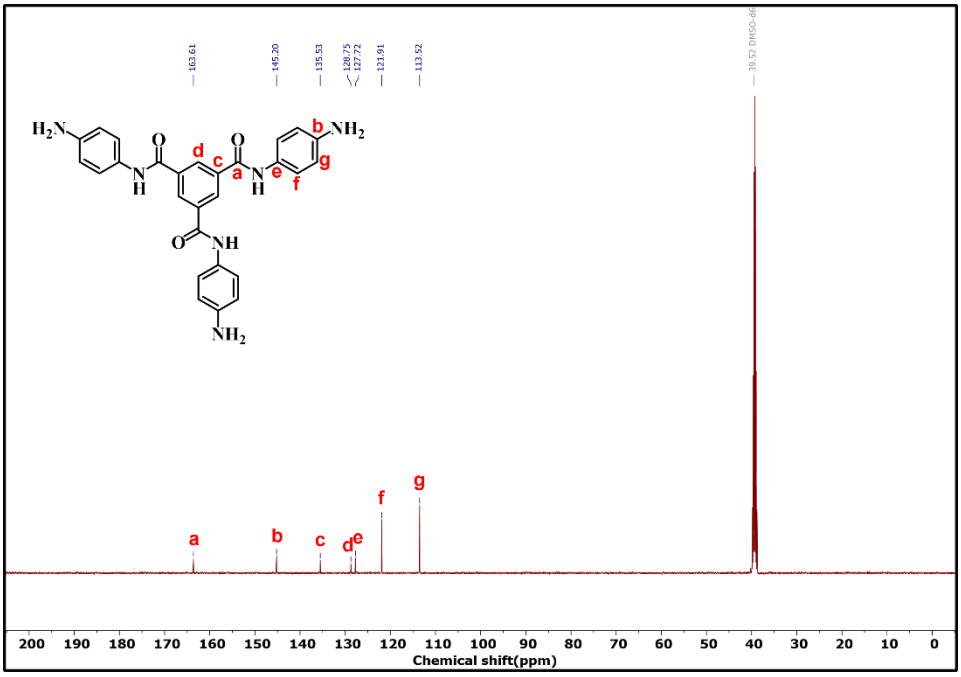

Figure 4.63: ^{13}C NMR of solid precipitate after drug release

The time-dependent release of Ibuprofen drug from **TABTA-Ibp** organogel at neutral (pH=7.4) and acidic (pH=5.29)[63] was studied (**Figure 4.64**) and (**Figure 4.65**) respectively. A significant decrease in the peak intensity at around 280 and 320 nm was observed, along with the rise of a new peak at 230 nm indicating the gradual release of the drug with time.

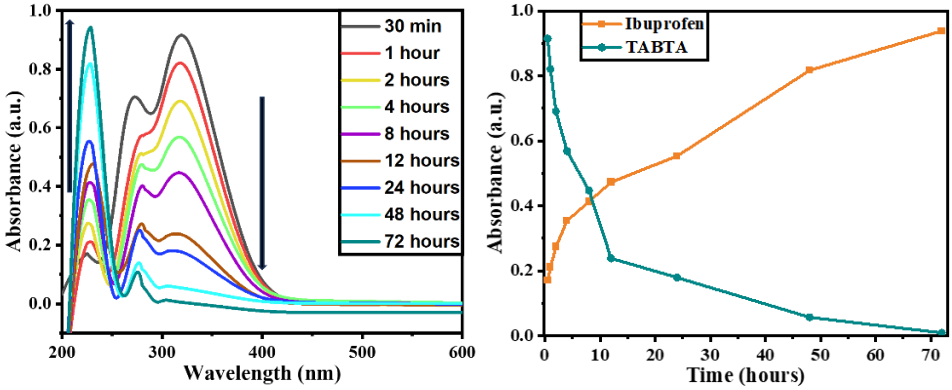

Figure 4.64: Release of Ibuprofen drug from **TABTA-Ibp** organogel collapsed using PBS buffer (pH=7.4) monitored by UV-visible spectroscopy

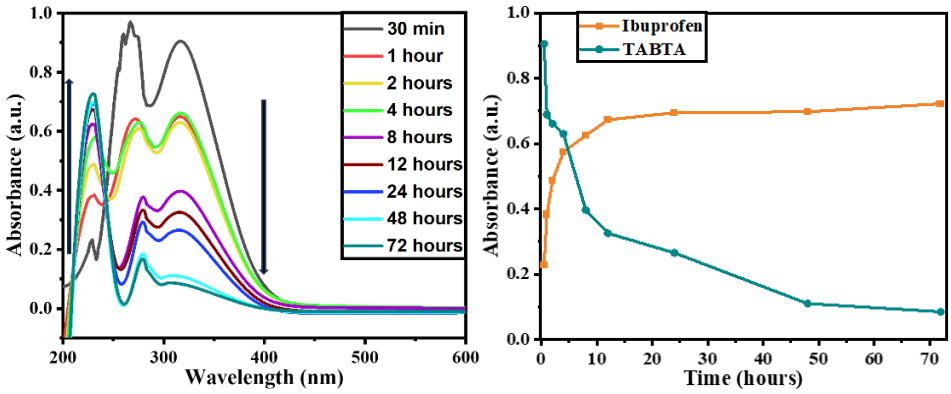

Figure 4.65: Release of Ibuprofen drug from **TABTA-Ibp** organogel collapsed using PBS buffer (pH=5.29) monitored by UV-visible spectroscopy

Similarly, the time-dependent release of Ibuprofen drug from **TABTA-Ibp-Ag** metallogel at neutral (pH=7.4) and acidic (pH=5.29) was studied (**Figure 4.66**) and (**Figure 4.67**) respectively. The drug release pattern exhibited a comparable trend to that observed in the **TABTA-Ibp** organogel.

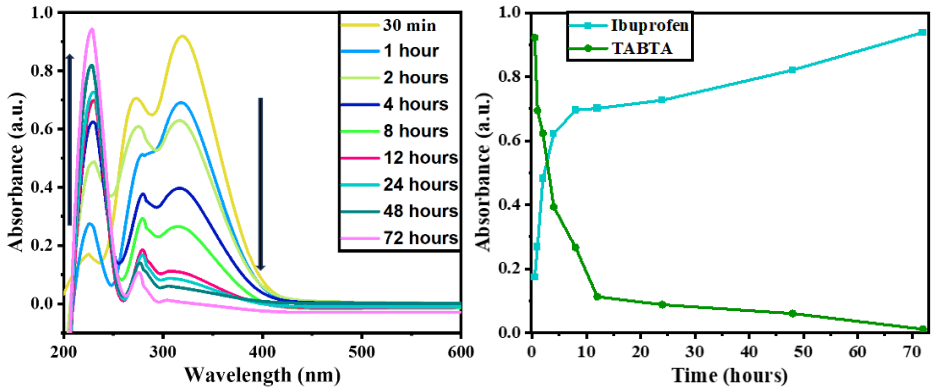

Figure 4.66: Release of Ibuprofen drug from **TABTA-Ibp-Ag** metallogel collapsed using PBS buffer (pH=7.4) monitored by UV-visible spectroscopy

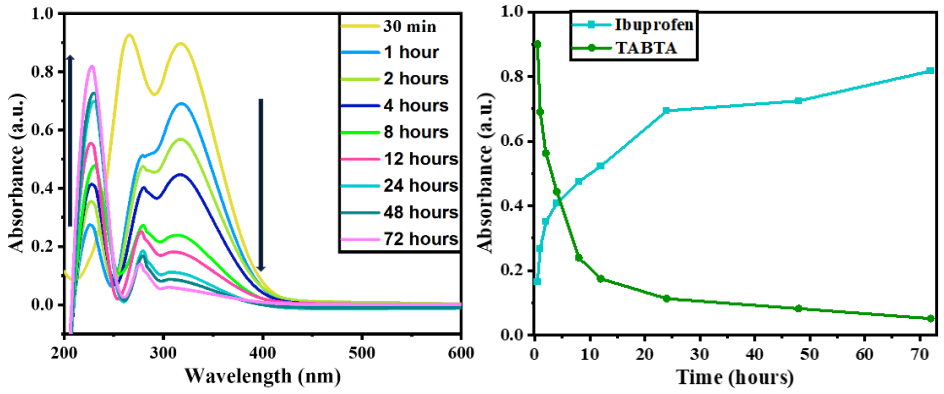

Figure 4.67: Release of Ibuprofen drug from **TABTA-Ibp-Ag** metallogel collapsed using PBS buffer (pH=5.29) monitored by UV-visible spectroscopy

The release of the drug was calculated, and it was observed that for **TABTA-Ibp** organogel, approximately 82% and 48% of the Ibuprofen were released from the gel matrix after 72 hours at pH=7.4 and 5.29, respectively. In comparison, in the **TABTA-Ibp-Ag** metallogel, about 85% and 57% of the Ibuprofen was released under the same conditions after 72 hours. (**Figure 4.68**). This might be due to the lower solubility of Ibuprofen in water in acidic pH values, thus decreasing the release rate at pH=5.29 compared to neutral pH=7.4.

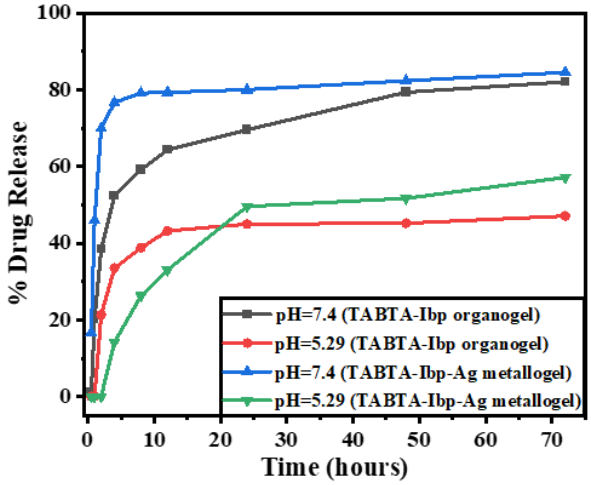

Figure 4.68: Drug release profile for **TABTA-Ibp** organogel and **TABTA-Ibp-Ag** metallogel at different pH= 7.4 and 5.29

CHAPTER 5

CONCLUSION AND FUTURE SCOPE

5.1 Conclusion

The organogels **G8-TABTA** and **TABTA-Ibp** and their respective metallogels have been successfully designed and their components, **G8** and **TABTA** have been characterized using mass, NMR, and FT-IR spectroscopy. The fabrication of the organogels and metallogels was confirmed by the test tube inversion method, and their gelation was optimized successfully. All the gels were found to be thixotropic, having moderate strength. Furthermore, the formation of silver nanoparticles within the gel matrix has been confirmed by UV-visible spectroscopy, PXRD analysis, and FESEM analysis. The effect of gelation on fluorescence intensity for the **G8-TABTA** gel matrix has also been studied where the organogel exhibits the ACQ phenomenon, and the **TABTA-Ibp** gel matrix has been loaded with silver nanoparticles and utilized for dual delivery of Ibuprofen drug and AgNPs. The release kinetics of Ibuprofen from the **TABTA-Ibp-Ag** matrix have been investigated, revealing that 85% of the drug is released from the matrix within 72 hours.

5.2 Future Scope

The silver nanoparticles are known to show good antimicrobial activity. Thus, investigation on the antibacterial properties of the organogel matrices and their metallogels is under process. This is purposefully done to design a matrix that simultaneously delivers Ibuprofen drug and AgNPs. Therefore, it is expected that these act as anti-inflammatory and antimicrobial agents.

REFERENCES

(1) Marr, P. C.; Marr, A. C. Ionic Liquid Gel Materials: Applications in Green and Sustainable Chemistry. *Green Chem.* **2016**, *18* (1), 105–128. https://doi.org/10.1039/C5GC02277K.

(2) John, G.; Jadhav, S. R.; Menon, V. M.; John, V. T. Flexible Optics: Recent Developments in Molecular Gels. *Angew. Chem. Int. Ed.* **2012**, *51* (8), 1760–1762. https://doi.org/10.1002/anie.201107167.

(3) Korde, J. M.; Kandasubramanian, B. Fundamentals and Effects of Biomimicking Stimuli-Responsive Polymers for Engineering Functions. *Ind. Eng. Chem. Res.* **2019**, *58* (23), 9709–9757. https://doi.org/10.1021/acs.iecr.9b00683.

(4) Ma, Y.; Tang, Y.; Billingham, N. C.; Armes, S. P.; Lewis, A. L. Synthesis of Biocompatible, Stimuli-Responsive, Physical Gels Based on ABA Triblock Copolymers. *Biomacromolecules* **2003**, *4* (4), 864–868. https://doi.org/10.1021/bm034118u.

(5) Trung, N. D.; Huy, D. T. N.; Jade Catalan Opulencia, M.; Lafta, H. A.; Abed, A. M.; Bokov, D. O.; Shomurodov, K.; Van Thuc Master, H.; Thaeer Hammid, A.; Kianfar, E. RETRACTED ARTICLE: Conductive Gels: Properties and Applications of Nanoelectronics. *Nanoscale Res. Lett.* **2022**, *17* (1), 50. https://doi.org/10.1186/s11671-022-03687-3.

(6) *Molecular Gels*; Weiss, R. G., Terech, P., Eds.; Springer Netherlands: Dordrecht, 2006. https://doi.org/10.1007/1-4020-3689-2.

(7) Biswas, P.; Ganguly, S.; Dastidar, P. Stimuli-Responsive Metallogels for Synthesizing Ag Nanoparticles and Sensing Hazardous Gases. *Chem. – Asian J.* **2018**, *13* (15), 1941–1949. https://doi.org/10.1002/asia.201800743.

(8) Houard, F.; Cucinotta, G.; Guizouarn, T.; Suffren, Y.; Calvez, G.; Daiguebonne, C.; Guillou, O.; Artzner, F.; Mannini, M.; Bernot, K. Metallogels: A Novel Approach for the Nanostructuration of Single-Chain Magnets. *Mater. Horiz.* **2023**, *10* (2), 547–555. https://doi.org/10.1039/D2MH01158A.

(9) Johannesson, J.; Khan, J.; Hubert, M.; Teleki, A.; Bergström, C. A. S. 3D-Printing of Solid Lipid Tablets from Emulsion Gels. *Int. J. Pharm.* **2021**, *597*, 120304. https://doi.org/10.1016/j.ijpharm.2021.120304.

(10) Tam, A. Y.-Y.; Yam, V. W.-W. Recent Advances in Metallogels. *Chem. Soc. Rev.* **2013**, *42* (4), 1540. https://doi.org/10.1039/c2cs35354g.

(11) Ding, J.; Zhou, G.; Liu, D.; Jiang, W.; Wei, Z.; Dong, X. Synthesis and Performance of a Novel High-Efficiency Coal Dust Suppressant Based on Self-Healing Gel. *Environ. Sci. Technol.* **2020**, *54* (13), 7992–8000. https://doi.org/10.1021/acs.est.0c00613.

(12) Ghosh, D.; Deepa; Damodaran, K. K. Metal Complexation Induced Supramolecular Gels for the Detection of Cyanide in Water. *Supramol. Chem.* **2020**, *32* (4), 276–286. https://doi.org/10.1080/10610278.2020.1751845.

(13) Jung, J. H.; Lee, J. H.; Silverman, J. R.; John, G. Coordination Polymer Gels with Important Environmental and Biological Applications. *Chem Soc Rev* **2013**, *42* (3), 924–936. https://doi.org/10.1039/C2CS35407A.

(14) Danks, A. E.; Hall, S. R.; Schnepp, Z. The Evolution of 'Sol-Gel' Chemistry as a Technique for Materials Synthesis. *Mater. Horiz.* **2016**, *3* (2), 91–112. https://doi.org/10.1039/C5MH00260E.

(15) Piepenbrock, M.-O. M.; Clarke, N.; Steed, J. W. Metal Ion and Anion-Based "Tuning" of a Supramolecular Metallogel. *Langmuir* **2009**, *25* (15), 8451–8456. https://doi.org/10.1021/la900145n.

(16) Michon, C.; Cuvelier, G.; Launay, B. Concentration Dependence of the Critical Viscoelastic Properties of Gelatin at the Gel Point. *Rheol. Acta* **1993**, *32* (1), 94–103. https://doi.org/10.1007/BF00396681.

(17) Martins, A. J.; Silva, P.; Maciel, F.; Pastrana, L. M.; Cunha, R. L.; Cerqueira, M. A.; Vicente, A. A. Hybrid Gels: Influence of Oleogel/Hydrogel Ratio on Rheological and Textural Properties. *Food Res. Int.* **2019**, *116*, 1298–1305. https://doi.org/10.1016/j.foodres.2018.10.019.

(18) Tanaka, J. Evaluation of Gel Point. In *Gels Handbook*; Elsevier, 2001; Vol. 1, pp 51–64. https://doi.org/10.1016/B978-012394690-4/50078-5.

(19) Lin, O. C. C. Thixotropic Behavior of Gel-like Systems. *J. Appl. Polym. Sci.* **1975**, *19* (1), 199–214. https://doi.org/10.1002/app.1975.070190115.

(20) Żeglin´ski, J.; Piotrowski, G. P.; Piękos´, R. A Study of Interaction between Hydrogen Peroxide and Silica Gel by FTIR Spectroscopy and Quantum Chemistry. *J. Mol. Struct.* **2006**, *794* (1–3), 83–91. https://doi.org/10.1016/j.molstruc.2006.01.043.

(21) Chen, X.; Peng, Y.; Tao, X.; Du, G.; Li, Q. Building a Quadruple Stimuli-Responsive Supramolecular Gel Based on a Supra-Amphiphilic Metallogelator. *New J. Chem.* **2021**, *45* (48), 22902–22907. https://doi.org/10.1039/D1NJ04764G.

(22) Shapiro, Y. E. Structure and Dynamics of Hydrogels and Organogels: An NMR Spectroscopy Approach. *Prog. Polym. Sci.* **2011**, *36* (9), 1184–1253. https://doi.org/10.1016/j.progpolymsci.2011.04.002.

(23) Lakshmi, R. V.; Bharathidasan, T.; Bera, P.; Basu, B. J. Fabrication of Superhydrophobic and Oleophobic Sol-Gel Nanocomposite Coating. *Surf. Coat. Technol.* **2012**, *206* (19–20), 3888–3894. https://doi.org/10.1016/j.surfcoat.2012.03.044.

(24) Verma, Y. L.; Singh, M. P.; Singh, R. K. Effect of Ultrasonic Irradiation on Preparation and Properties of Ionogels. *J. Nanomater.* **2012**, *2012*, 1–6. https://doi.org/10.1155/2012/570719.

(25) Cametti, M.; Džolić, Z. AIE-Active Supramolecular Gel Systems. In *Aggregation-Induced Emission (AIE)*; Elsevier, 2022; pp 117–164. https://doi.org/10.1016/B978-0-12-824335-0.00002-7.

(26) Wang, Q.; Wu, H.; Qian, W.; Gao, A.; Cao, X. Design of Multifunctional Fluorescent Self-Assembly System for Sensing Hg2+, Volatile Acids and Being Applied as Anti-Counterfeit Materials through the Transformation of ACQ-to-AIE. *Dyes Pigments* **2023**, *216*, 111372. https://doi.org/10.1016/j.dyepig.2023.111372.

(27) Su, M.; Liu, C.; Zhang, Y.; Rong, X.; Wang, X.; Li, X.; Wang, K.; Zhu, H.; Zhu, B. Rational Design of a Water-Soluble TICT-AIEE-Active Fluorescent Probe for Mercury Ion Detection. *Anal. Chim. Acta* **2022**, *1230*, 340337. https://doi.org/10.1016/j.aca.2022.340337.

(28) Zong, L.; Xie, Y.; Wang, C.; Li, J.-R.; Li, Q.; Li, Z. From ACQ to AIE: The Suppression of the Strong π–π Interaction of Naphthalene Diimide Derivatives through the Adjustment of Their Flexible Chains. *Chem. Commun.* **2016**, *52* (77), 11496–11499. https://doi.org/10.1039/C6CC06176A.

(29) Shah, J. Cubic Phase Gels as Drug Delivery Systems. *Adv. Drug Deliv. Rev.* **2001**, *47* (2–3), 229–250. https://doi.org/10.1016/S0169-409X(01)00108-9.

(30) Branco, M. C.; Pochan, D. J.; Wagner, N. J.; Schneider, J. P. Macromolecular Diffusion and Release from Self-Assembled β-Hairpin Peptide Hydrogels. *Biomaterials* **2009**, *30* (7), 1339–1347. https://doi.org/10.1016/j.biomaterials.2008.11.019.

(31) Das, S.; Solra, M.; Rana, S. Emulsion Gel: A Dual Drug Delivery Platform for Osteoarthritis Treatment. *Regen. Eng. Transl. Med.* **2023**, *9* (2), 279–294. https://doi.org/10.1007/s40883-022-00282-x.

(32) Mathew, A. P.; Uthaman, S.; Cho, K.-H.; Cho, C.-S.; Park, I.-K. Injectable Hydrogels for Delivering Biotherapeutic Molecules. *Int. J. Biol. Macromol.* **2018**, *110*, 17–29. https://doi.org/10.1016/j.ijbiomac.2017.11.113.

(33) Datta, S.; Bhattacharya, S. Multifarious Facets of Sugar-Derived Molecular Gels: Molecular Features, Mechanisms of Self-Assembly and Emerging Applications. *Chem. Soc. Rev.* **2015**, *44* (15), 5596–5637. https://doi.org/10.1039/C5CS00093A.

(34) Malviya, N.; Sonkar, C.; Ganguly, R.; Bhattacharjee, D.; Bhabak, K. P.; Mukhopadhyay, S. Novel Approach to Generate a Self-Deliverable Ru(II)-Based Anticancer Agent in the Self-Reacting Confined Gel Space. *ACS Appl. Mater. Interfaces* **2019**, *11* (50), 47606–47618. https://doi.org/10.1021/acsami.9b17075.

(35) Fang, W.; Zhang, Y.; Wu, J.; Liu, C.; Zhu, H.; Tu, T. Recent Advances in Supramolecular Gels and Catalysis. *Chem. – Asian J.* **2018**, *13* (7), 712–729. https://doi.org/10.1002/asia.201800017.

(36) Kyarikwal, R.; Malviya, N.; Chakraborty, A.; Mukhopadhyay, S. Preparation of Tris-Tetrazole-Based Metallogels and Stabilization of Silver Nanoparticles: Studies on Reduction Catalysis and Self-Healing Property. *ACS Appl. Mater. Interfaces* **2021**, *13* (49), 59567–59579. https://doi.org/10.1021/acsami.1c19217.

(37) Kyarikwal, R.; Munjal, R.; Nag, P.; Vennapusa, S. R.; Mukhopadhyay, S. Design and Synthesis of Hydrophobic Mixed Organogels with Complementary Hydrogen-Bond Donor–Acceptor Sites: Removal of Heavy Metal Ions Hg^{2+}, Cd^{2+} and Pb^{2+} from Aqueous Solution. *Mater. Adv.* **2023**, *4* (16), 3603–3618. https://doi.org/10.1039/D3MA00300K.

(38) Malviya, N.; Sonkar, C.; Kundu, B. K.; Mukhopadhyay, S. Discotic Organic Gelators in Ion Sensing, Metallogel Formation, and Bioinspired Catalysis. *Langmuir* **2018**, *34* (38), 11575–11585. https://doi.org/10.1021/acs.langmuir.8b02352.

(39) Sheikhi, A.; Van De Ven, T. G. M. Trapping It Softly: Ultrasoft Zirconium Metallogels for Macromolecule Entrapment and Reconfiguration. *ACS Macro Lett.* **2016**, *5* (8), 904–908. https://doi.org/10.1021/acsmacrolett.6b00447.

(40) Uzan, S.; Barış, D.; Çolak, M.; Aydın, H.; Hoşgören, H. Organogels as Novel Carriers for Dermal and Topical Drug Delivery Vehicles. *Tetrahedron* **2016**, *72* (47), 7517–7525. https://doi.org/10.1016/j.tet.2016.10.009.

(41) Parveen, R.; Dastidar, P. Supramolecular Gels by Design: Towards the Development of Topical Gels for Self-Delivery Application. *Chem. – Eur. J.* **2016**, *22* (27), 9257–9266. https://doi.org/10.1002/chem.201600105.

(42) Yadav, E.; Khatana, A. K.; Sebastian, S.; Gupta, M. K. DAP Derived Fatty Acid Amide Organogelators as Novel Carrier for Drug Incorporation and pH-Responsive Release. *New J. Chem.* **2021**, *45* (1), 415–422. https://doi.org/10.1039/D0NJ04611F.

(43) Constantin, M.; Lupei, M.; Bucatariu, S.-M.; Pelin, I. M.; Doroftei, F.; Ichim, D. L.; Daraba, O. M.; Fundueanu, G. PVA/Chitosan Thin Films Containing Silver Nanoparticles and Ibuprofen for the Treatment of Periodontal Disease. *Polymers* **2022**, *15* (1), 4. https://doi.org/10.3390/polym15010004.

(44) Popescu, I.; Constantin, M.; Solcan, G.; Ichim, D. L.; Rata, D. M.; Horodincu, L.; Solcan, C. Composite Hydrogels with Embedded Silver Nanoparticles and Ibuprofen as Wound Dressing. *Gels* **2023**, *9* (8), 654. https://doi.org/10.3390/gels9080654.

(45) Klapötke, T. M.; Sabaté, C. M. The Preparation and Characterization of Guanylurea Nitrate and Perchlorate Salts. *Heteroat. Chem.* **2008**, *19* (3), 301–306. https://doi.org/10.1002/hc.20419.

(46) Dos Santos, C. M. G.; Boyle, E. M.; De Solis, S.; Kruger, P. E.; Gunnlaugsson, T. Selective and Tuneable Recognition of Anions Using C3v-Symmetrical Tripodal Urea-Amide Receptor Platforms. *Chem. Commun.* **2011**, *47* (44), 12176. https://doi.org/10.1039/c1cc15233e.

(47) Li, Y.; Chen, W.; Gao, R.; Zhao, Z.; Zhang, T.; Xing, G.; Chen, L. 2D Covalent Organic Frameworks with Built-in Amide Active Sites for Efficient Heterogeneous Catalysis. *Chem. Commun.* **2019**, *55* (96), 14538–14541. https://doi.org/10.1039/C9CC07500C.

(48) Kyarikwal, R.; Kundu, B. K.; Chakraborty, A.; Mukhopadhyay, S. A Tris-Tetrazole Based Nanostructured Soft Material: Studies on Self-Healing, AIEE, and Rheological and Fluorometric Detection of 3-Aminopyridine. *Mater. Chem. Front.* **2022**, *6* (19), 2835–2847. https://doi.org/10.1039/D2QM00520D.

(49) Lundquist, K. Proton (1H) NMR Spectroscopy. In *Methods in Lignin Chemistry*; Lin, S. Y., Dence, C. W., Eds.; Timell, T. E., Series Ed.; Springer Series in Wood Science; Springer Berlin Heidelberg: Berlin, Heidelberg, 1992; pp 242–249. https://doi.org/10.1007/978-3-642-74065-7_17.

(50) Bax, A.; Ferretti, J. A.; Nashed, N.; Jerina, D. M. Complete Proton and Carbon-13 NMR Assignment of Complex Polycyclic Aromatic

Hydrocarbons. *J. Org. Chem.* **1985**, *50* (17), 3029–3034. https://doi.org/10.1021/jo00217a001.

(51) Matsumoto, Y.; Honma, K. NH Stretching Vibrations of Pyrrole Clusters Studied by Infrared Cavity Ringdown Spectroscopy. *J. Chem. Phys.* **2007**, *127* (18), 184310. https://doi.org/10.1063/1.2790894.

(52) Suchkova, G. G.; Maklakov, L. I. Amide Bands in the IR Spectra of Urethanes. *Vib. Spectrosc.* **2009**, *51* (2), 333–339. https://doi.org/10.1016/j.vibspec.2009.09.002.

(53) Ramukutty, S.; Ramachandran, E. Growth, Spectral and Thermal Studies of Ibuprofen Crystals. *Cryst. Res. Technol.* **2012**, *47* (1), 31–38. https://doi.org/10.1002/crat.201100394.

(54) Shameli, K.; Majid Darroudi; Mansor Bin Ahmad; Wan Md. Zin Wan Yunis; Nor Azowa Ibrahim. Synthesis and Characterization of Silver/Talc Nanocomposites Using the Wet Chemical Reduction Method. *Int. J. Nanomedicine* **2010**, 743. https://doi.org/10.2147/IJN.S13227.

(55) Hussein-Al-Ali, S. H.; Abudoleh, S. M.; Abualassal, Q. I. A.; Abudayeh, Z.; Aldalahmah, Y.; Hussein, M. Z. Preparation and Characterisation of Ciprofloxacin-loaded Silver Nanoparticles for Drug Delivery. *IET Nanobiotechnol.* **2022**, *16* (3), 92–101. https://doi.org/10.1049/nbt2.12081.

(56) Khan, M. A. M.; Kumar, S.; Ahamed, M.; Alrokayan, S. A.; Alsalhi, M. S.; Alhoshan, M.; Aldwayyan, A. S. Structural and Spectroscopic Studies of Thin Film of Silver Nanoparticles. *Appl. Surf. Sci.* **2011**, *257* (24), 10607–10612. https://doi.org/10.1016/j.apsusc.2011.07.058.

(57) Ferraria, A. M.; Carapeto, A. P.; Botelho Do Rego, A. M. X-Ray Photoelectron Spectroscopy: Silver Salts Revisited. *Vacuum* **2012**, *86* (12), 1988–1991. https://doi.org/10.1016/j.vacuum.2012.05.031.

(58) Malviya, N.; Das, M.; Mandal, P.; Mukhopadhyay, S. A Smart Organic Gel Template as Metal Cation and Inorganic Anion Sensor. *Soft Matter* **2017**, *13* (36), 6243–6249. https://doi.org/10.1039/C7SM01199G.

(59) Li, J.; Mooney, D. J. Designing Hydrogels for Controlled Drug Delivery. *Nat. Rev. Mater.* **2016**, *1* (12), 16071. https://doi.org/10.1038/natrevmats.2016.71.

(60) Radin, S.; Chen, T.; Ducheyne, P. The Controlled Release of Drugs from Emulsified, Sol-Gel Processed Silica Microspheres. *Biomaterials* **2009**, *30* (5), 850–858. https://doi.org/10.1016/j.biomaterials.2008.09.066.

(61) Hoang, V. D.; Ly, D. T. H.; Tho, N. H.; Minh Thi Nguyen, H. UV Spectrophotometric Simultaneous Determination of Paracetamol and Ibuprofen in Combined Tablets by Derivative and Wavelet Transforms. *Sci. World J.* **2014**, *2014*, 1–13. https://doi.org/10.1155/2014/313609.

(62) Xu, Y.; Zhan, C.; Fan, L.; Wang, L.; Zheng, H. Preparation of Dual Crosslinked Alginate–Chitosan Blend Gel Beads and in Vitro Controlled Release in Oral Site-Specific Drug Delivery System. *Int. J. Pharm.* **2007**, *336* (2), 329–337. https://doi.org/10.1016/j.ijpharm.2006.12.019.

(63) Gao, W.; Chan, J. M.; Farokhzad, O. C. pH-Responsive Nanoparticles for Drug Delivery. *Mol. Pharm.* **2010**, *7* (6), 1913–1920. https://doi.org/10.1021/mp100253e.